

Erik Wangensten Berg

Anti-icing coatings based on graphene oxide additions; preparation and characterization

June 2019



NTNU
Norwegian University of
Science and Technology

Anti-icing coatings based on graphene oxide additions; preparation and characterization

Erik Wangensten Berg

Submission:	June 2019	
Program:	Materials Science and Engineering	
Supervisor:	Hilde Lea Lein	IMA
Co-Supervisors:	Sidsel Meli Hanetho	SINTEF
	Anh Hoang Dam	CealTech

Norwegian University of Science and Technology
Department of Materials Science and Engineering

Abstract

Ice formation is a serious challenge for many industries operating in subzero conditions. Current methods for ice mitigation and removal are energy intensive, laborious and environmentally hazardous. A promising candidate to revolutionize anti-icing surfaces are superhydrophobic coatings. These coatings utilize their water-repellent attributes to shed water droplets before icing can occur. The major drawback with these coatings are their low mechanical robustness and durability. Developing a durable superhydrophobic coating with anti-icing properties is an ideal solution to cope with ice formation.

In this work, reinforced hydrophobic nanocomposites were constructed and evaluated. A hierarchical composite structure was achieved by combining the inherent steel microstructure with synthesized silicon dioxide, silica, nanoparticles. Surface chemistry was altered by depositing a thin hydrophobic polymer based on the 1H,1H,2H,2H-perfluorooctyltriethoxysilane precursor. Different quantities of graphene oxide was added to act as a reinforcing agent. Graphene oxides effect on tribological, hydrophobic and anti-icing properties were evaluated. Nanoparticle and coating deposition were done by a spray coating technique. Low graphene oxide content of 0.01 wt% yielded the best overall results with a high contact angle at $150^{\circ} \pm 4^{\circ}$ coupled with a contact angle hysteresis of $23^{\circ} \pm 9^{\circ}$. The coating also demonstrated improved nucleation temperature, icing durability and abrasion resistance. Graphene oxide additions proved detrimental to the ice formation delay regardless of graphene oxide amount. These finding show a promising potential for graphene oxide additions to anti-icing coatings and continued research is warranted. Despite low graphene oxide content achieving very high contact angles, none of the coatings qualified as superhydrophobic due to the rose petal effect.

Sammendrag

Isdannelse utgjør et stort problem i flere industrier. Dagens metoder for å hindre isdannelse er både energikrevende og omfattende. I tillegg blir miljøfarlige kjemikalier hyppig brukt. Et lovende alternativ er superhydrofobiske coatinger med anti-ising egenskaper. Disse coatingene avstøter inntreffende vann før isdannelse kan oppstå. Ulempen ved disse coatingene er deres lave mekaniske styrke og holdbarhet.

Denne oppgaven fokuserer på eksperimentell armering av hydrofobiske nanokompositter. En hierarkisk overflatestruktur oppnås ved å kombinere kald-valset stål sin mikrostruktur med silisium dioksid, silika, nanopartikler. Overflate energien har blitt manipulert ved å deponere en tynn hydrofobisk polymer basert på 1H,1H,2H,2H-perfluorooktyltrietoxsysilan. Forskjellige mengder grafen oksid ble tilsatt for å armere polymer matriksen. Grafen oksids påvirkning på tribologiske, hydrofobiske og anti-ising egenskaper ble evaluert. Nanopartikkel og coating deponering ble utført via spray deponering. En coating med 0.01 vt% grafen oksid og nanopartikler resulterte i det beste sammenlagte resultatet. Denne coatingen viste en superhydrofobisk kontaktvinkel på $150^{\circ} \pm 4^{\circ}$ med en kontaktvinkel hysteresese på $23^{\circ} \pm 9^{\circ}$. Denne coatingen viste også en forbedret slitastebestandighet, holdbarhet og nukleeringstemperatur. Grafen oksid hadde en negativ effekt på forsinkelse av isdannelse uavhengig av grafen oksid mengde. På bakgrunn av disse resultatene har grafen oksid vist et lovende potensiale for armering av hydrofobiske nanokompositter. Til tross for høye målte kontaktvinkler kunne ingen av nanokomposittene kunne bli kvalifisert som superhydrofobisk på grunn av rose petal effekten.

Preface

This master's thesis is the result of work conducted during the spring of 2019, the last semester of a 5-year Master's degree programme in Materials Science and Engineering at the Norwegian University of Science and Technology (NTNU).

Work has been performed in collaboration the Functional Materials and Materials Chemistry Research Group (FACET) at the department of Materials Science and Engineering. Associate professor Hilde Lea Lein has been the main supervisor. The work has been supported by SINTEF Industry with Sidsel Meli Hanetho as co-supervisor. The work has also been performed in collaboration with CealTech with Anh Hoang Dam as co-supervisor. The research done has been built on the insight provided by earlier work performed by Raymond Luneng [1], Hanna S. Vassmyr [2] and the specialization project by the author [3]. Substrates were supplied by Finmekanisk verksted at NTNU and tribological characterization was performed by SINTEF. All experimental work in this thesis was performed by the author.

Trondheim, June 2019

Erik Wangensten Berg

Acknowledgements

This last semester has been a roller coaster of experiences. From scrapping failed experiments and starting over, to crying tears of joy after imaging my first nanoparticles. The work has been ambitious and challenging, but at the same time very rewarding and inspiring.

The work performed during this last semester would have been impossible without help and constant support from the people around me. First of all, I would like to thank my supervisor, Associate Professor Hilde Lea Lein, for your guidance, encouragement and positive feedback. I would also like to thank you for allowing me to work independently and testing my own hypotheses. I also want to extend my gratitude to my co-supervisor Sidsel Meli Hanetho for your valuable insights and your uplifting spirit. Finally I would like to thank my co-supervisor Anh Hoang Dam for your knowledge and valuable feedback.

I would also like to thank all of the people who assisted me with instrument training, lab equipment or otherwise contributed to my work. I also would like to thank everyone in the FACET group for your constructive criticism and support during the thesis.

Contents

Abstract	ii
Sammendrag	iii
Preface	iv
Acknowledgement	v
1 Background	1
1.1 Motivation	1
1.2 Aim of the work	3
2 Introduction	4
2.1 Surface tension and thermodynamics	4
2.2 Hydrophobicity	6
2.3 Wetting states	8
2.4 Roughness	10
2.5 Hierarchical structure	12
2.6 Anti-icing surfaces	13
2.7 Graphene oxide	17
2.8 Sol-Gel synthesis	18
2.9 Spray coating	21
3 Experimental	23
3.1 Substrates	25

3.2	Cleaning	25
3.3	Nanoparticle synthesis	25
3.4	Coating synthesis	27
3.5	Spray coating	29
3.6	Heat treatment	30
3.7	Characterization	30
3.8	Contact angle measurements	33
3.9	Environmental experiments	34
3.10	Sample summary	36
4	Results	38
4.1	Microroughness	38
4.2	Rheology	41
4.3	Nanoparticles	41
4.4	Nanoparticle deposition	45
4.5	Coating characterization	49
4.6	Wetting	53
4.7	Anti-icing properties	57
4.8	Tribological properties	62
5	Discussion	63
5.1	Hierarchical structure	63
5.2	Synthesis evaluation	67
5.3	Wetting states	68
5.4	Spray coating and rheology	69
5.5	Coating thickness and coverage	70
5.6	Contact angle evaluation	72
5.7	Anti-icing characterization	73
5.8	Tribological assessment	75
5.9	Graphene oxides effect on anti-icing coatings	75
6	Conclusion	77
7	Further work	79

Appendices	89
A - Spray coat optimization	90
B - Nanoparticles	93
C - Coating	97
D - Python codes	104

List of Figures

1.1	Clean and iced turbine blade.	2
2.1	A representation of the three phase junction according to Young's equation.	6
2.2	Visual representation of advancing and receding angle during tilting.	8
2.3	Wenzel and Cassie-Baxter wetting states	10
2.4	Cassie impregnating wetting state	11
2.5	Illustration of a hierarchical structure	13
2.6	An overview and comparison of the different anti-icing surfaces.	14
2.7	pH dependence for silicon alkoxides.	19
2.8	The relationship between pH and particle morphology.	20
2.9	Schematic of the spray coating process.	22
3.1	Flowchart of the experimental work	24
3.2	Chemical formula of 1H,1H,2H,2H-Perfluorooctyltriethoxysilane	27
3.3	A comparison of the droplet fitting modes.	34
3.4	Sample summary	37
4.1	3D presentation of the surface texture.	39
4.2	SEM image of the steel microstructure.	40
4.3	Nanoparticle cluster (NP1)	42
4.4	Nanoparticle cluster (NP2)	43
4.5	Particle comparison	44
4.6	Nanoparticle buildup	46
4.7	Nanoparticle coverage (NP1)	47

4.8	Nanoparticle coverage (NP2)	48
4.9	Coating thickness	49
4.10	Graphene oxide sheets	50
4.11	Pure graphene oxide	51
4.12	Graphene oxide coverage on γ 3- β 1-NP0 sample	52
4.13	High magnification graphene oxide image	53
4.14	Contact angles vs graphene oxide content plot	55
4.15	Contact angle comparison measured in the DSA	55
4.16	Volume and contact angle vs time	56
4.17	Change in contact angle as a function of temperature	58
4.18	Ice formation process	59
4.19	Abrasion resistance	62
5.1	Nanoparticles effect on wetting	65
5.2	Nanoparticle density	66
5.3	Nanoparticle pinning of water droplet	69
5.4	Baseline example	73
1	Nanoparticle coverage after one layer.	90
2	Nanoparticle coverage after three layers.	91
3	Nanoparticle coverage after four layers.	92
4	Image of a nanoparticle cluster on a γ 0- β 0-NP1 sample. A thin an even spreading of nanoparticles can also be observed.	93
5	Magnified image of a NP1 particles on a γ 0- β 0-NP1 sample.	94
6	Image of nanoparticle coverage on a γ 0- β 0-NP2 sample.	95
7	Image of a γ 0- β 0-NP2 sample displaying the size variance of NP2 particles.	96
8	Overview image of a γ 1- β 2-NP2. A decent particle coverage can be observed. A graphene oxide sheet can be observed on the bottom right side of the image.	97
9	Magnified image of a γ 1- β 2-NP2. A graphene oxide sheet can be seen covering the nanoparticles.	98

10	Overview image of a $\gamma 2$ - $\beta 2$ -NP2. A large particle buildup can be observed with high amounts of graphene oxide covering the buildups.	99
11	Image of a $\gamma 2$ - $\beta 2$ -NP2. A graphene oxide sheet can be seen covering the nanoparticles.	100
12	Image of a $\gamma 3$ - $\beta 2$ -NP2 sample. A large concentration of graphene oxide sheets can be seen covering the nanoparticles.	101
13	Image of a $\gamma 1$ - $\beta 2$ -NP0 sample. A graphene oxide sheet covering the cold-rolled microstructure can be observed.	102
14	Image of a $\gamma 2$ - $\beta 2$ -NP0 sample. A graphene oxide sheet covering the cold-rolled microstructure can be observed.	103

List of Tables

3.1	Composition of 316-steel.	25
3.2	Chemicals used for cleaning substrates.	25
3.3	Chemicals applied during silica nanoparticle synthesis.	26
3.4	Precise amounts of chemicals used.	26
3.5	Chemicals applied during coating synthesis.	27
3.6	Categorized synthesis method and graphene oxide quantities.	28
3.7	Exact quantities used during all fluorosilane syntheses.	29
3.8	Spray coating parameters.	29
3.9	Heat treatment parameters.	30
3.10	HAAKE MARS III measurement parameters.	31
3.11	Tribology.	32
4.1	Average profile roughness, skewness and kurtosis.	38
4.2	Viscosity measurements	41
4.3	A summary of the respective nanoparticle sizes	42
4.4	Contact angle results	54
4.5	Nucleation temperatures	58
4.6	Energy barrier for ice nucleation results.	60
4.7	Icing/deicing cycling	61

List of Abbreviations

CA	Contact angle
CAH	Contact angle hysteresis
ROA	Roll-off angle
GO	Graphene oxide
TEOS	Tetraethyl orthosilicate
NP	Nanoparticle
β-silane	1H,1H,2H,2H-Perfluorooctyltriethoxysilane
DI water	Deionized water
FESEM	Field emission scanning electron microscope
EDS	Energy-dispersive X-ray spectroscopy

Chapter 1

Background

In the following chapter, motivation and the aim of the work will be presented.

1.1 Motivation

Ice formation pose a serious challenge for modern industry operating in sub zero conditions. In temperate and arctic regions, ice accumulation on infrastructure such as high-voltage power lines can be detrimental to the structural integrity. Consequently reducing the reliability of electrical transport [4, 5]. In the energy sector, wind turbines may suffer greatly from icing on the turbine blades. Turbine power losses are estimated to be up to 20% during icing, decreasing the total annual energy production of up to 2% [6, 7]. Another industry often operating in freezing conditions is the aviation industry. Both when grounded and in-flight, airplanes may be crippled by ice formation. When grounded in subzero conditions, ice formed on the wings and fuselage will reduce the lift-off coefficient preventing take-off [8]. While in-flight the adversely low temperature in the stratosphere may affect the flight characteristics which may have fatal consequences [9]. Figure 1.1 provide a visual example of ice accumulation on a wind turbine blade.

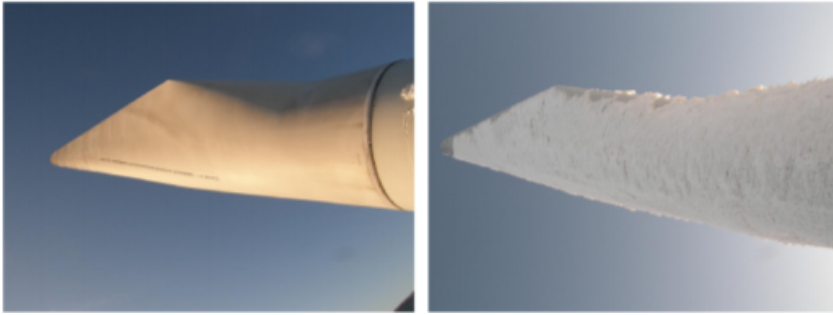


Figure 1.1: Clean and iced turbine blade. Adopted from [7].

There are two main options for mitigating ice accretion, active de-icing and passive anti-icing [10]. Active de-icing is the removal of ice after formation and includes thermal heating, mechanical removal and de-icing chemicals [4, 11]. This removal step is often followed up by the use of passive anti-icing chemicals. Passive anti-icing solutions is the prevention of ice formation by using chemicals or a coating with anti-icing characteristics. Passive anti-icing chemicals are commonly used, but they are unfavourable because of their toxicity and negative environmental impact [12]. State of the art anti-icing coatings are currently inferior compared to chemicals and lacks the durability needed for long term applications [13]. A disadvantage of using de-icing techniques and passive chemicals are their short term effect. Thus frequent reapplication is required increasing both power consumption and maintenance cost. Considering the disadvantages, it is evident that active de-icing techniques and the use of chemicals are sub-optimal. A passive anti-icing alternative is therefore highly desirable. A durable anti-icing coating designed for long-term use is an ideal solution, reducing both maintenance cost and power consumption.

Graphene oxide is a relatively new material with an abundance of interesting properties. A monolayer of graphene oxide is reported to exhibit a Young's modulus of 207.6 ± 23.4 GPa [14]. Introducing graphene oxide into an anti-icing coating, can amplify the mechanical strength and durability of the coating [15, 16, 17]. A strong and durable nanocomposite with anti-icing properties can serve as a energy-efficient alternative to de-icing techniques and chemicals. Graphene oxides influence on anti-icing properties is relatively uncharted which substantiates the importance of this thesis.

1.2 Aim of the work

The main objective and aim of the work is to synthesize a reinforced nanocomposite exhibiting anti-icing properties. The anti-icing properties will be evaluated based on the hydrophobic character of the nanocomposite. Limited research has been established on graphene oxides influence on anti-icing coatings. Consequently this thesis will have an experimental approach on how to incorporate graphene oxide into a hydrophobic coating and lay some groundwork characterizing anti-icing properties of the nanocomposite.

Selection of coating was made based on the earlier work performed by H.Vassmyr and R.Luneng [1, 2]. The coating conjoins a polymer matrix and silica nanoparticles to form a superhydrophobic nanocomposite. 1H,1H,2H,2H-perfluorooctyltriethoxysilane is the precursor of the hydrophobic polymer. Ice formation is mitigated by the superhydrophobic nature of the coating. Whereas the introduction of graphene oxide will potentially enhance the mechanical strength of the nanocomposite, acting as a reinforcing agent. Due to the application of this nanocomposite, nanocomposite will henceforth be referred to as a coating.

The experimental work will focus on how to introduce graphene oxide into the polymer matrix and how different quantities of graphene oxides influence the coating. The coating will be characterized in terms of contact angles, roll of angle and contact angle hysteresis to evaluate hydrophobicity and wetting state. Anti-icing characteristics such as nucleation temperature, ice delay and durability will be measured. To evaluate tribological properties, coefficient of friction will be measured.

Chapter 2

Introduction

When designing an anti-icing coating, two main approaches can be taken; either a superhydrophobic or an icephobic approach. A superhydrophobic approach entails minimizing wetting of water droplets, repelling water droplets prior to ice formation. While an icephobic approach consist of hindering ice accumulation by reducing ice adhesion on the surface. This thesis focus on the superhydrophobic approach and how graphene oxide additions will influence the coating. The following chapter will expand upon surface energy, hydrophobicity, roughness, hierarchical structure, sol-gel synthesis, anti-icing surfaces, graphene oxide, spray coating and how superhydrophobicity can impede ice formation.

2.1 Surface tension and thermodynamics

All surfaces have a contractile force acting upon the surface working to minimize the surface area of the material [18]. This force is most evident when inspecting a glass while filling it with water - the contractile force will force the water to bulge above the rim before overflowing. This force is called surface tension. Surface tension develops because of cohesion within the liquid which is the attraction between identical molecules [19]. For example in water, molecules prefer to stay in the interior where hydrogen can form

Van der Waals bonds with the surrounding oxygen atoms [18]. Surface water molecules are unable to fully form these bonds due to fewer neighboring molecules [18, 19]. Thus water will strive to minimize the amount of unformed bonds, by reducing the surface area [18, 20]. Surface tension is denoted as γ and attempts to keep the surface in equilibrium. If a force is infinitesimally larger than this equilibrium, a new surface is produced. This force is termed work, W , and can be related to the surface tension through Equation 2.1 [20, 21].

$$W = \gamma dA \quad (2.1)$$

The area upon the work is performed is defined as dA . When considering the work required to overcome cohesive forces within the liquid, we often employ the term work of adhesion, W_a . By relating work performed to thermodynamic variables, we can derive Equation 2.2 through rigorous differentiation. As confirmed by several authors this surface energy is related to thermodynamics by Equation 2.2, when temperature and pressure is constant [18, 20, 21, 22]. Gibbs free energy is expressed as dG .

$$dG = \gamma dA \quad (2.2)$$

Based on Equation 2.2 we can conclude that changes in surface tension is thermodynamically motivated. Surface tension per area is often referred to as surface energy and is denoted as γ with a subscript indicating the surface area. Previously we defined the amount of work required to create a new surface, but what is of particular interest in this thesis is the work of adhesion, which quantifies the attraction between two surfaces. A mathematical expression for work of adhesion is displayed in Equation 2.3 where γ_{sl} , γ_{lv} and γ_{sv} are the surface energies between the solid-liquid, liquid-vapor and the solid-vapour respectively [18, 23].

$$W_{sl} = \gamma_{sv} + \gamma_{lv} - \gamma_{sl} \quad (2.3)$$

W_{sl} is the work of adhesion between a liquid and solid surface. The specific interaction

between liquid, in our case water, and solid surfaces can be manipulated by controlling the surface tension, γ_s [18, 23].

2.2 Hydrophobicity

Hydrophobicity is the absence of attraction between a solid surface and a water molecule, i.e. how well the surface repels water. Studies have shown that both surface energy and surface texture are important factors when investigating hydrophobicity [24, 25, 26]. When a water droplet is deposited onto a perfectly flat surface, a junction between the water, surface and air will occur called the three phase junction. An illustration of the three phase junction is provided in Figure 2.1, where γ_{sl} , γ_{lv} and γ_{sv} are the surface energies between the solid-liquid, liquid-vapor and the solid-vapour respectively.

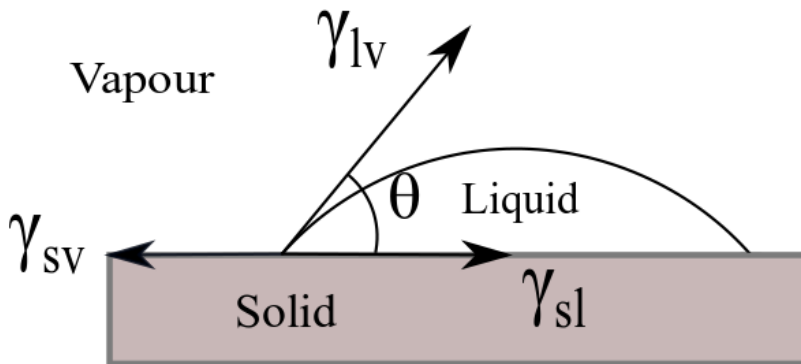


Figure 2.1: Representation of a three phase junction according to Young's equation.
Inspired by [18]

The angle formed at this junction is called the contact angle, abbreviated CA. The contact angle, denoted as θ can be used to quantify the hydrophobicity. Young's Equation 2.4 describes the force equilibrium in the horizontal direction which occurs in the three phase junction depicted in Figure 2.1 [18, 24].

$$\cos\theta = \frac{\gamma_{sv} - \gamma_{sl}}{\gamma_{lv}} \quad (2.4)$$

If θ exceeds 90° the surface is considered hydrophobic, while a θ below 90° is considered hydrophilic [27]. A special case of hydrophobicity is superhydrophobicity. Superhydrophobic surfaces exhibits a very high contact angle of $\theta > 150^\circ$. Another term closely related to the contact angle is wetting. Wetting is a liquids ability to retain contact with the substrate [28]. The degree of wetting, termed wettability, is based upon adhesive forces explained in Section 2.1. Hydrophilic surfaces displays high wettability while hydrophobic surfaces displays low wettability [27, 28, 29].

Young's equation assumes a perfectly flat surface which is rarely the case in real situations. All surfaces have some degree of roughness and heterogeneity, and these factors have to be considered when evaluating hydrophobicity [18]. Across a real surface a multitude of metastable states exist with different surface energies dependent on the local topography and surface chemistry [30]. This phenomena will give rise to different contact angles across the surface and the static θ will not be sufficient in determining hydrophobicity. Measuring the contact angle hysteresis is a method of including these metastable states and quantifying the dynamic contact angle [31, 32]. The contact angle hysteresis can be found by depositing a water droplet onto a substrate and slowly tilting the substrate, as shown in Figure 2.2. Consequently a gravitational pull will force the droplet to form an asymmetric shape and eventually move down the inclined surface. When the droplet begins advancing down the tilted surface, a critical asymmetric form is reached. Forming two distinct contact angles, one at each side of the droplet. These contact angles are measured at the last possible moment prior to movement and are called the advancing and receding contact angles. The advancing contact angle, denoted as θ_{adv} , is the largest contact angle formed on the advancing side of the droplet. While the receding contact angle is the minimum angle, denoted as θ_{rec} [31]. Contact angle hysteresis, abbreviated CAH, is defined as the difference between the advancing and receding contact angle as presented in Equation 2.5 [27, 30, 31, 33].

$$CAH = \theta_{adv} - \theta_{rec} \quad (2.5)$$

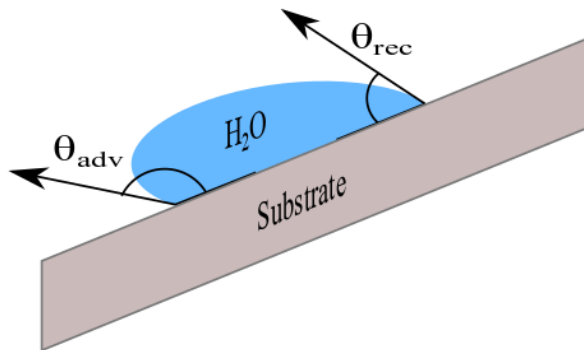


Figure 2.2: Visual representation of advancing and receding angle during tilting.
Inspired by [31]

Another term linked to CAH is the roll-off angle, abbreviated as ROA. Roll-off angle is defined as the angle of tilt when the water droplet begins to slide down the surface [34]. A low contact angle hysteresis reflects a high water droplet repellency which is vital for superhydrophobic surfaces [26, 31]. A surface with a contact angle above 150° and contact angle hysteresis below 10° exhibit extreme water-repellent behaviour and can be defined as superhydrophobic [10, 25, 27].

2.3 Wetting states

The assumption of a perfectly smooth surface is plausible when studying liquid-liquid interaction, but when investigating liquid-solid interaction, heterogeneity have to be included. R. Wenzel introduced a roughness correction factor to Young's equation in 1936 [35]. This correction factor, r_w , accounted for the ratio between the actual and geometric surface, presented in Equation 2.6 [35, 36].

$$r_w = \frac{\text{actual surface}}{\text{geometric surface}} \quad (2.6)$$

$$r_w \cos\theta = \cos\theta_W = \frac{\gamma_{sv} - \gamma_{sl}}{\gamma_{lv}} \quad (2.7)$$

Wenzel could calculate the contact angle more accurately based on roughness by integrating, r_w into Young's Equation 2.7, where θ_W is the roughness corrected angle. A system obeying Equation 2.7 is called a Wenzel wetting state [33]. Wenzel wetting state is defined as having perfect wetting of the exposed asperities on the solid surface [35, 36]. Figure 2.3A presents a visual interpretation of a Wenzel wetting state.

Perfect wetting of the surface asperities is rarely the real wetting state and the Wenzel wetting state may prove insufficient. Pockets of air may fill the cavities between the asperities, forcing the liquid to rest on the apex of the asperities. Providing a perfect non-wetting state between the asperities, this wetting state was defined by Cassie and Baxter in 1944 termed the Cassie-Baxter state [36]. The Cassie-Baxter wetting state assumes the cavities between peaks being filled with vapour instead of liquid, splitting the liquid-surface interface into a liquid-solid interface and a liquid-vapour interface [37]. The sum of these interfaces make up the Cassie-Baxter Equation 2.8, and provides us with the apparent contact angle in a Cassie-Baxter state, θ_{CB} [38]. The surface fraction of liquid-solid and liquid-vapour interfaces are denoted as f_{ls} and f_{lv} respectively, with their respective contact angles θ_{ls} and θ_{lv} [37, 38].

$$\cos\theta_{CB} = f_{ls} \cos\theta_{ls} + f_{lv} \cos\theta_{lv} \quad (2.8)$$

With further manipulation, we can use the fact that f_{ls} is the fraction of the solid surface which is wetted by the liquid expressed as f . Ergo the fraction of liquid in contact with vapour is $(1 - f)$. If the vapour is air, the contact angle will be $\theta_{lv} = 180^\circ$. Providing us with the improved Equation 2.9 [38, 39].

$$\cos\theta_{CB} = f \cos\theta - (1 - f) \quad (2.9)$$

f will range between 0 and 1. Hence decreasing f will decrease the fraction of contact, directly increasing the apparent contact angle θ_{CB} i.e increasing hydrophobicity [38]. A visual representation of the Wenzel and Cassie-Baxter states are provided in Figure 2.3.

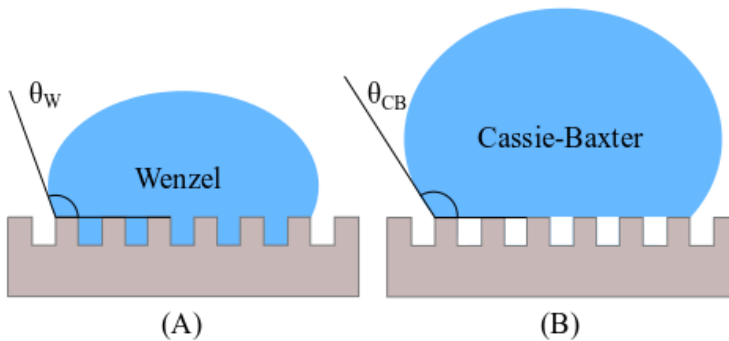


Figure 2.3: Wenzel (A) and Cassie-Baxter (B) wetting states. Inspired by [36].

Another important wetting phenomena to consider is partial wetting. Water can partially penetrate surface asperities and cause a different wetting regime called a Cassie impregnating state [40]. During Cassie impregnating state, the water droplet is pinned by the surface roughness causing a very high adhesion. This results in a high CA combined with a high CAH. This phenomena is also called the rose petal effect [40]. Figure 2.4 illustrates a Cassie impregnating state.

2.4 Roughness

A quantitative measure of the two dimensional profile roughness is the average roughness, denoted as R_a . Average roughness is defined as the arithmetic average of the absolute height deviation from the mean [41]. The average roughness, R_a is measured in two dimensions and is the most common way to asses roughness profiles [42]. A mathematical definition is supplied in Equation 2.10, where n is the number of data

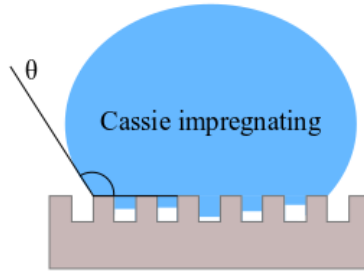


Figure 2.4: Partial wetting leading to a Cassie impregnating state will behave. Inspired by [40].

points and y_i is the height deviation from the mean [41, 43].

$$R_a = \frac{1}{n} \sum_{i=1}^n |y_i| \quad (2.10)$$

A flaw in the average roughness parameter, is the lack of consideration to local variability [42, 43]. Large anomalies will increase the average roughness, reducing it's accuracy. In order to take local variability into account, two additional statistical parameters must be introduced; Skewness and Kurtosis, expressed mathematically as R_{sk} and R_{ku} respectively. Skewness is the measure of profile symmetry [41], i.e whether the profile consist of mainly peaks or valleys. A positive skewness indicates a majority of peaks, while negative skewness suggest a prevalence of valleys. Skewness for a normal distribution of peaks and valleys is zero. Different surface structures may exhibit similar average roughness values, hence skewness is used to differentiate them. Equation 2.11 provides the mathematical definition of skewness, where n is the number of data points, y_i is the height deviation from the mean and R_q is the root mean square roughness expressed in the subsequent Equation 2.12 [41, 43].

$$R_{sk} = \frac{1}{nR_q^3} \left(\sum_{i=1}^n y_i^3 \right) \quad (2.11)$$

$$R_q = \sqrt{\frac{1}{n} \sum_{i=1}^n y_i^2} \quad (2.12)$$

To complement the average roughness and skewness, kurtosis is used. Kurtosis reflects the shape of the height distribution compared to a normal distribution [42]. A normal height distribution will display a $R_{ku} = 3$, while a broad height distribution has a $R_{ku} < 3$ [41]. An $R_{ku} > 3$ indicate a narrow height distribution. The mathematical kurtosis formula is presented in Equation 2.13 [41, 43].

$$R_{ku} = \frac{1}{nR_q^4} \left(\sum_{i=1}^n y_i^4 \right) \quad (2.13)$$

2.5 Hierarchical structure

A natural material displaying a superhydrophobic character is the lotus leaf. Papillae¹ grows on the surface providing the leaf with a microroughness. In addition each papillae contains nanosized asperities giving the leaf both a micro and nanoscale roughness [44]. These two roughness categories layered on top of each other is described as a hierarchical structure [25]. Surface chemistry combined with hierarchical roughness is the reason for the superhydrophobic nature of the lotus leaf [25, 44, 45]. An illustration of a hierarchical structure is displayed in Figure 2.5.

Microroughness combined with a nanoroughness create a hierarchical structure which is known to enhance the hydrophobic properties of a surface [25, 40, 45]. Hierarchical structures is therefore vital in achieving superhydrophobicity. The hierarchical structure presented in Figure 2.5 facilitates a higher degree of liquid-vapour interface reducing the area of liquid-surface contact, ensuring a high contact angle. Obtaining such a structure will favour a Cassie-Baxter wetting state where the liquid droplet will rest on top of the micro- and nano-scaled asperities [13, 20, 25].

¹Papillose epidermal cells



Figure 2.5: Illustration of a hierarchical structure containing nanosized asperities on top of microsized asperities, providing a nanoroughness and microroughness respectively.

2.6 Anti-icing surfaces

Designing an anti-icing surface is a complex procedure. There are multiple strategies for obtaining anti-icing characteristics ranging from smooth infused polymers to textured superhydrophobic coatings. Kreder et.al [13] performed a comprehensive study of anti-icing surfaces and constructed an overview of the different anti-icing surfaces. Figure 2.6 provides a redrawn and adapted version of the anti-icing surface overview [13]. The anti-icing properties of dry surfaces are owed to their ability of rapidly shedding incoming water droplets. Dry surfaces focus on preventing ice formation by limiting the amount of water on the surface. Their major drawback is their durability and robustness. The asperities in the hierarchical structure deteriorates during icing/de-icing cycles [13, 46]. Wet surfaces usually consist of a porous structure infused with a water-immiscible liquid [47]. Wet surfaces demonstrate a low ice adhesion due to the slippery liquid interface between the liquid surface and ice [13, 47]. The following subsections will elaborate on how dry textured surfaces can behave as an anti-icing surface.




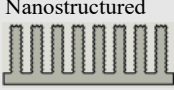

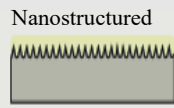
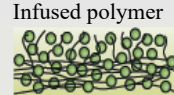

	Type of surface	Advantage	Disadvantage
Dry surface	Self-assembled monolayer 	<ul style="list-style-type: none"> • Environmentally tolerant 	<ul style="list-style-type: none"> • Limited compatibility • Lower performance than state of the art
	Bulk coatings 	<ul style="list-style-type: none"> • Environmentally tolerant • Versatile and durable 	<ul style="list-style-type: none"> • Lower performance than state of the art
	Microstructured 	<ul style="list-style-type: none"> • Rapid shedding of droplets prevents ice nucleation 	<ul style="list-style-type: none"> • Poor pressure tolerance • Low humidity tolerance • Poor durability
	Nanostructured 	<ul style="list-style-type: none"> • Improved pressure tolerance • Improved humidity tolerance 	<ul style="list-style-type: none"> • Poor durability
Wet surface	Microstructured 	<ul style="list-style-type: none"> • Low ice adhesion • Low droplet CAH • High humidity and pressure tolerance 	<ul style="list-style-type: none"> • Poor resistance to lubricant resistance
	Nanostructured 	<ul style="list-style-type: none"> • Improved lubricant retention 	<ul style="list-style-type: none"> • Low mechanical robustness
	Infused polymer 	<ul style="list-style-type: none"> • Increased lubricant content 	<ul style="list-style-type: none"> • Kinetics of lubricant depletion and replenishment is unknown
	Hydrated 	<ul style="list-style-type: none"> • Low ice adhesion without need for lubricant replenishment 	<ul style="list-style-type: none"> • Poor wetting properties

Figure 2.6: An overview and comparison of the different anti-icing surfaces. Redrawn and inspired by Kreder et.al [13].

2.6.1 Anti-icing properties

A term called icephobicity is frequently used to distinguish the ice repellent properties of a surface. Icephobic surfaces should demonstrate three different, although related, attributes [48]:

1. Suppressing ice formation of water condensing on the surface
2. Prevent freezing of incoming water
3. Low ice adhesion, to easily shed/remove ice after ice formation

Suppressing ice formation

Suppression of ice formation can be investigated by measuring the delay of ice nucleation. This delay is regulated by the energy barrier for ice nucleation, i.e energy needed for ice nucleation to begin. Several factors can influence this energy barrier, and for superhydrophobic coatings the delay is generally attributed to the insulating effect of the air pockets which arise in a Cassie-Baxter wetting state [13, 49]. A Wenzel wetting state will have the adverse effect, by increasing the solid-liquid interface, consequently lowering the energy barrier necessary for ice nucleation. Delay in ice formation has an excellent synergy with superhydrophobicity. Both require a Cassie-Baxter state and by increasing the nucleation time, water droplets will have more time to shed before nucleation can occur.

Prevent freezing of incoming water

Preventing freezing of incoming water relies on the ability to repel the incoming water droplets at low temperatures [48]. Superhydrophobic coatings is considered ideal candidates because of their excellent water repellent abilities. Due to their low wettability, water droplets will bounce of the surface, reducing the contact time. A crucial challenge is to maintain the superhydrophobic behaviour at low temperatures.

Ice adhesion

Even the best anti-icing surfaces will suffer from ice formation under extreme conditions. Effective and easy removal of ice formed is a critical, but challenging requirement. Ice adhesion can be quantified by measuring the energy needed to displace ice formed on the surface. Ice adhesion is most commonly tested by performing a shear strength test, where a ice adhesion below $\sim 500\text{kPa}$ is seen as the benchmark for icephobicity [48]. If we take passive removal factors into account such as wind and vibration, ice adhesion of less than $\sim 20\text{kPa}$ must be achieved [13].

Ice adhesion can be approximated by using thermodynamic work of adhesion. From Equation 2.3, we can utilize the almost identical surface energies of water and ice to approximate ice adhesion [13, 50]. Equation 2.14 assumes similar interfacial energies at the solid interface. Through equation 2.14 we can approximate the ice adhesion based upon surface energy and the hydrophobic behaviour of the surface. Where γ_w is the water interface and θ_{rec} is the receding contact angle.

$$W_a \approx \gamma_w (1 + \cos\theta_{rec}) \quad (2.14)$$

2.6.2 Superhydrophobicity and icephobicity

In recent years, new discoveries have been made on the anti-icing properties of nanostructured superhydrophobic coatings. These coatings have demonstrated both delayed ice formation and reduced ice adhesion [51, 52, 53]. A challenge faced when exploring the anti-icing properties of superhydrophobic coatings are the multiple length scales involved [13]. The hierarchical structure on superhydrophobic coatings ranges from 50 nm to 10 μm . These sizes are usually sufficient to promote a Cassie-Baxter state because of the macroscopic dimension of typical water droplets. However the critical nucleus size necessary for ice nucleation is less than 10 nm [13].

2.7 Graphene oxide

Graphene was successfully isolated and characterized in 2004 by Andre Geim and Konstantin Novoselov [54]. This achievement sparked widespread research for the use and application of graphene due to its remarkable physicochemical properties. Graphene oxide, abbreviated GO, is a monomolecular layer of graphite oxide and is a derived branch of graphene functionalized with various oxide groups [55]. The oxygen groups have mostly been identified as hydroxyl and epoxy groups. However the precise atomic structure remains elusive [55].

Graphene oxide demonstrates a high mechanical strength, a high specific surface area and excellent thermal and electrical conductivities [14, 55, 56]. A challenge facing graphene oxide and hydrophobicity, is the hydrophilic nature of the oxide groups [57]. Graphene oxide is soluble in water which is unfavourable when aiming for a hydrophobic surface. An advantage with this solubility is the ability to form stable and homogeneous dispersions of GO through sonification [57].

An area where graphene oxide show great coating potential is the mechanical strength. Graphene oxide consist of a hexagonal carbon network with hybridized sp^2 and sp^3 orbitals creating strong γ -bonds [55]. This honeycomb structure yield sheets of graphene oxide exhibiting a high Young's modulus of 207.6 ± 23.4 GPa [14]. Taking advantage of this high modulus the graphene oxide sheets can be used as two dimensional nanofillers in the polymer matrix to enhance the mechanical strength [15, 16, 17, 58]. By embedding graphene oxide into the polymer matrix, it is possible to increase the mechanical strength and durability while retaining the hydrophobic nature of the polymer.

2.8 Sol-Gel synthesis

A sol-gel synthesis is the process of forming a stable monodisperse colloidal solution and adding a catalyst to achieve gelation. When synthesizing nanoparticles with a bottom-up method, the sol-gel process is frequently used because of its versatility. The sol-gel method employs hydrolysis and condensation to achieve a high-purity composition with homogeneity at the molecular level [59]. The nature of these reactions vary significantly depending on the type of precursor utilized [60]. Alkoxide-based precursors are preferred because of their favourable hydrolysis equilibria [61].

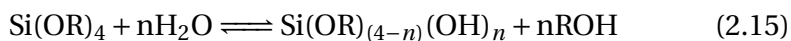
The sol-gel method includes the following steps [59, 60]:

1. Formation of a stable dispersion (sol).
2. Gelation resulting from the formation of an oxide- or alcohol-bridged network (the gel) by a polycondensation or polyesterification.
3. Aging of the gel, where polycondensation reactions continue until the gel transforms into a solid mass.
4. Drying of the gel to remove water and other volatile liquids from the gel network.
5. Dehydration, where the gel is calcined to remove surface-bound -OH groups. The removal of these groups will protect the gel from rehydration and stabilize the gel.
6. Densification and decomposition of the gel at high temperatures (> 800 °C).

2.8.1 Sol-Gel parameters

Water content and pH strongly influence the process and outcome of the sol-gel method. The reaction rate of hydrolysis is largely governed by amount of water present in the system [60]. Equation 2.15 describes the relationship between the silicon-water molar ratio, given by $n = \frac{Si}{H_2O}$, and the hydrolysis reaction. By increasing the water content, the

rate of hydrolysis will increase by substituting several alkyl groups with silanol groups.



Controlling the rate of hydrolysis and condensation is important when a specific product is desired. pH has a large impact on the reaction kinetics [62]. Figure 2.7 display the relative reaction rate based on pH for silicon alkoxides.

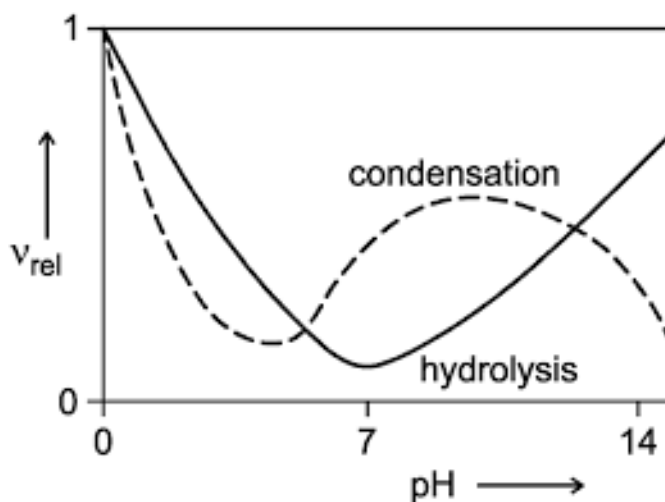


Figure 2.7: pH dependence of the hydrolysis and condensation reaction for silicon alkoxides. Adopted from [62].

Morphology and size is also heavily influenced by the pH. A system catalyzed with acid favours the condensation reaction, and will form polymer chains. These chains will branch out and interconnect to form a three-dimensional gel network [60], visualized in Figure 2.8 at the bottom left corner. A base catalyzed system will establish repulsive forces between the particles, negating the formation of networks and promoting the formation of nanoparticles [61], as observed in Figure 2.8. If the pH is kept stable, the nanoparticles formed will be monodisperse [60].

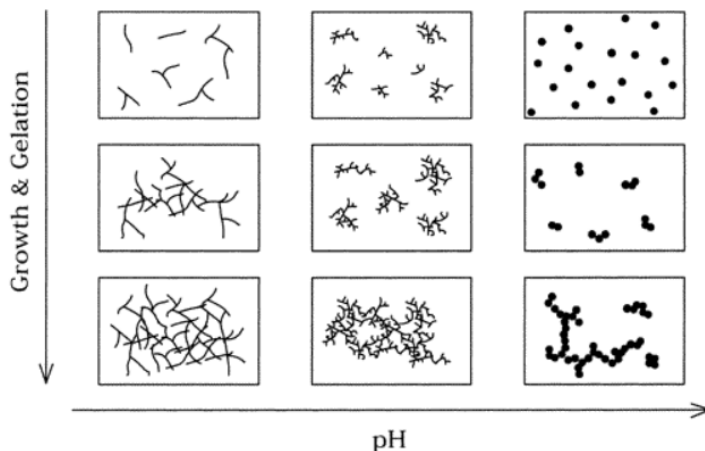
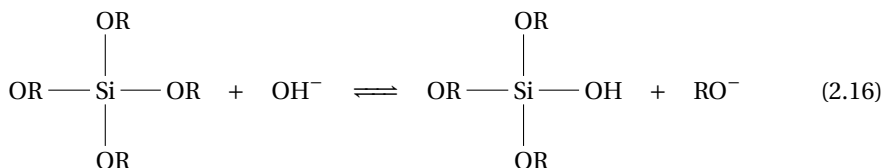


Figure 2.8: The relationship between pH and particle morphology. Adopted from [60].

2.8.2 Silica nanoparticle synthesis

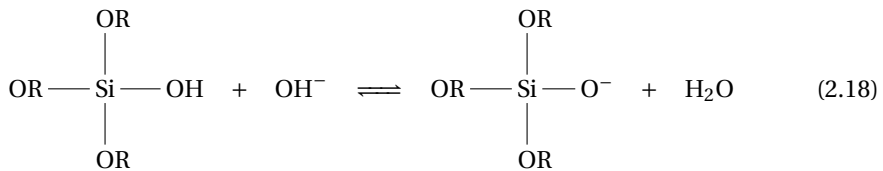
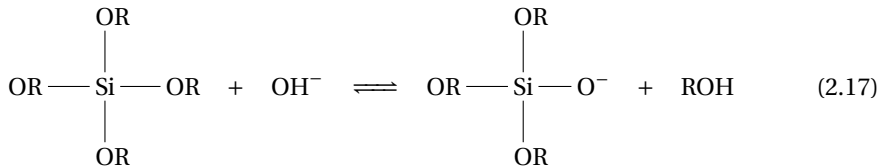
A well established method used to synthesize silica nanoparticles is the Stöber-Fink-Bohn method [63]. This process offers good growth control and can be tailored to yield spherical nanoparticles ranging from 5 – 2000nm [64]. The precursor used is tetraethyl orthosilicate, abbreviated as TEOS. This chemical compound consist of silicon as the metalloid central atom, surrounded by four alkoxy ligands. Multiple TEOS molecules forming siloxane bridges make up the silica nanoparticles. TEOS will be denoted mathematically as $\text{Si}(\text{OR})_4$.

When water is introduced into the system containing the TEOS precursor, a spontaneous hydrolysis reaction will occur as shown in Equation 2.16. The hydrolysis reaction rate is dependent on the silicon-water ratio and pH, as explained in Section 2.8.1.

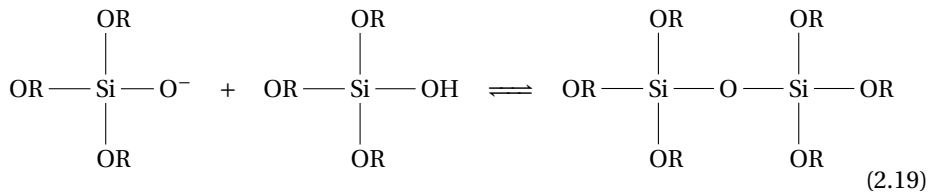


During the hydrolysis, silanol groups are formed, as shown in Equation 2.16. The stability of these silanol groups are relatively low because of the high electronegativity of silicon [60]. Therefore a weakening of the OH bonds will allow the condensation reactions to

occur. The condensation reaction needs to be catalyzed under basic conditions in order to obtain spherical nanoparticles, delineated in Figure 2.8 [62]. Two possible catalyzation routes exist; either by basic activation of the precursor molecule, or a base reacting with a hydrolyzed molecule, expressed in Equation 2.17 and 2.18 respectively [60, 64].



Reactions displayed in Equation 2.17 and 2.18 will then condensate via the reaction shown in Equation 2.19. Stable siloxane bridges are formed through the condensation step.



2.9 Spray coating

Spray coating is a deposition technique frequently used to deposit superhydrophobic coatings [65, 66]. Spray coating is both cheap and feasible for industrial applications. The technique consist of mixing a solution with a carrier gas, which is subsequently deposited via a nozzle [67]. Figure 2.9 demonstrates the deposition process. Heat can also be applied to substrates to improve coating adhesion and minimize coating defects [68].

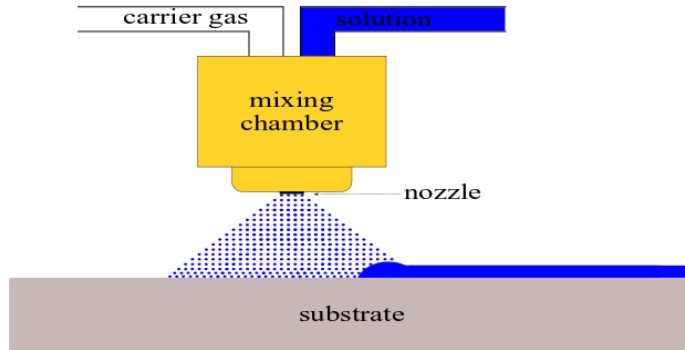


Figure 2.9: Schematic of the spray coating process.

Spray coating is fast and minimizes the amount of waste solution by providing excellent coverage control. Coating thickness and spray coverage are heavily influenced by flow rate and droplet size respectively [67, 69]. Coating thickness increase with increasing flow rate [67]. Flow rate is dependent on the liquids viscosity, higher viscosity result in a reduction of flow rate. Droplet size affect the spreading of liquid on the substrate. Where spreading is the degree of droplet wetting during deposition. Large droplets increase spreading [69]. The droplet size is limited by the nozzle. Spray coverage is also affected by the surface texture. Rough surfaces alter the impact dynamics and increase the chance of droplet splashing, consequently increasing the unevenness of the coating [69].

Chapter 3

Experimental

Cold rolled 316 stainless steel substrates was cleaned with acetone and isopropanol. Followed by surface characterization to determine microroughness. Silica nanoparticles of two different sizes were synthesized by a sol-gel process inspired by the Stöber-Fink-Bohn method. Nanoparticles were deposited onto substrates via spray coating. Hydrophobic coatings were subsequently synthesized with varying degrees of graphene oxide content. To create an intuitive overview, four graphene oxide categories were created. Where each category signify different amounts of graphene oxide, the categories are γ_0 , γ_1 , γ_2 and γ_3 . Graphene oxide content increase by a decade for each incremented number. γ_0 is the reference category without any graphene oxide content. These coatings were deposited onto steel substrates with and without silica nanoparticles, to evaluate the effect of nanoroughness created by the nanoparticles. After each deposition step, the substrate were heat treated before further characterization such as contact angle measurements, tribological testing and anti-icing experiments. Figure 3.1 presents a flowchart of the experimental work. Nanoparticles are abbreviated as NP.

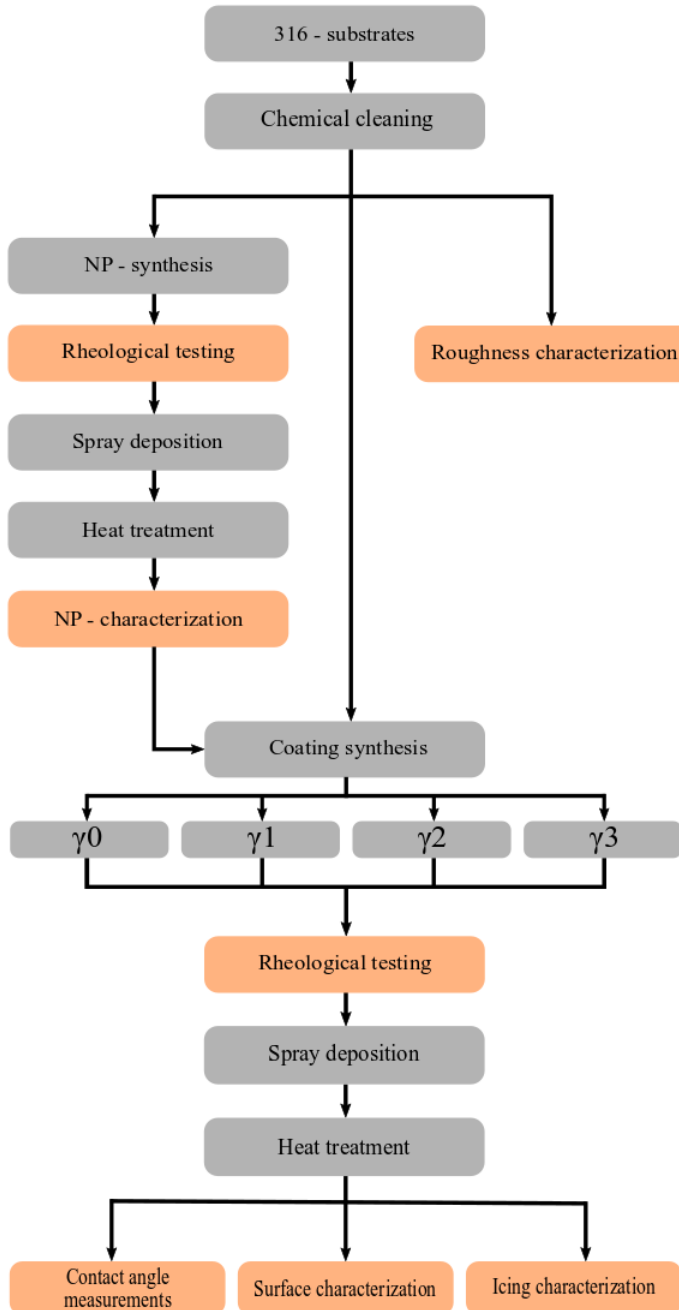


Figure 3.1: A flowchart of the experimental work. Light grey indicate an experimental process, while light orange indicate a characterization step.

3.1 Substrates

316-steel substrates were supplied and precut into by 15 x 10 x 2 mm³ by Finmekanisk Verksted at NTNU. All substrates are cold rolled during manufacturing. Consequently its microstructure will be influenced by the mechanical deformation received during fabrication. The cold-rolled 316 steel received no further surface modification during this thesis and its surface texture will be referred to as untreated. The composition of the 316 alloy is presented in Table 3.1.

Table 3.1: Composition of 316-steel, all percentages are given in weight percent.

Ni [%]	Cr[%]	C[%]	Mn[%]	Si[%]	S[%]	P[%]	N[%]	Mo[%]	Fe
10-14	16-18	0.08	2.0	0.75	0.03	0.045	0.10	2.0-3.0	Bal.

3.2 Cleaning

Substrates were chemically cleaned to minimize surface contaminants. Substrates were submerged in acetone and placed in a sonication bath for five minutes. Followed by a twenty-four hour immersion in isopropanol stored at ambient temperature. Substrates were dried in normal atmosphere at room temperature. Cleaned substrates were immediately utilized after drying. Chemicals used for cleaning is listed in Table 3.2.

Table 3.2: Chemicals used for cleaning substrates.

Name	Chemical formula	Provider	CAS
Isopropanol	C_3H_8O	Sigma-Aldrich	67 – 63 – 0
Acetone	C_3H_6O	Sigma-Aldrich	67 – 64 – 1

3.3 Nanoparticle synthesis

The nanoparticles were produced by the Stöber-Fink-Bohn process. Tetraethyl orthosilicate, TEOS, was chosen as a precursor with ethanol used as the solvent. In order to

acquire nanoparticles, the pH was augmented by applying ammonium hydroxide as the catalyst. A detailed layout of chemicals used and their purpose is provided in Table 3.3.

Table 3.3: Chemicals applied during silica nanoparticle synthesis.

Name	Formula	Purpose	Provider	CAS
Tetraethyl orthosilicate ¹	$Si(OC_2H_5)_4$	Precursor	Sigma-Aldrich	78 – 10 – 4
Ammonium hydroxide ²	NH_4OH	Catalyst	Sigma-Aldrich	1336 – 21 – 6
Ethanol ³	C_2H_5OH	Solvent	VWR	64 – 17 – 5

The synthesis procedure was adapted from earlier work performed by R.Luneng [1] and H.Vassmyr [2]. Ethanol, de-ionized water and ammonium hydroxide was added to a 100mL round bottom flask, the respective amounts are presented in Table 3.4. The round bottom flask was placed on top of a RCT Basic hotplate from IKA and mounted to a Liebig condenser to prevent evaporation loss. To mix the reactants, magnetic stirring was used while the hotplate temperature were preset to 35°C. The reactants were left to stir for 10 minutes to achieve a homogeneous solution. Followed up by dropwise addition of TEOS through a burette. When all of the TEOS was successfully added, the solution was left to react at constant temperature and stirring for the specified amount of time. Subsequently the round bottom flask was removed from the hotplate and cooled at room temperature. When the solution reached room temperature it was immediately transferred to a different beaker and stored at 4°C. Two types of nanoparticles were synthesized, where reaction time and stirring was varied to achieve different nanoparticle sizes. pH was measured using a pH-meter, edition PHM210, from MeterLab.

Table 3.4: A categorized presentation of the precise amounts of chemicals used during silica nanoparticle synthesis.

Sol-ID	pH	TEOS	NH ₄ OH	EtOH	DI water	Reaction time	RPM
NP1	12.02	1.5 mL	3.0 mL	45.0 mL	5.0 mL	50 min	350
NP2	11.88	1.5 mL	3.0 mL	45.0 mL	5.0 mL	60 min	400

¹98%, Reagent grade

²28-30%, ACS reagent

³96%

3.4 Coating synthesis

A sol-gel technique was used to synthesize the hydrophobic coating. 1H,1H,2H,2H-Perfluorooctyltriethoxysilane, denoted as β -silane, was used as the precursor in the sol-gel process. The precursor selection was based upon the hydrophobic nature of the β -silane and the results from earlier work performed by R.Luneng and H.Vassmyr [1, 2]. The chemical structure of precursor is depicted in Figure 3.2. Chemicals used are outlined in Table 3.5. The most challenging aspect during synthesis was to incorporate graphene oxide into the sol-gel process. After numerous trials and errors, a solution of mixing graphene oxide into the pH-augmented water was discovered. This solution yielded promising preliminary results and was therefore chosen as the main synthesis method.

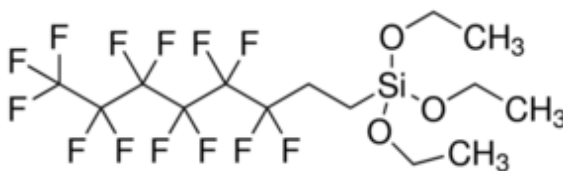


Figure 3.2: Chemical formula of 1H,1H,2H,2H-Perfluorooctyltriethoxysilane. Adapted from [70]

Table 3.5: Chemicals applied during coating synthesis.

Name	Formula	Purpose	Provider	CAS
1H,1H,2H,2H-Perfluorooctyltriethoxysilane	$C_{14}H_{19}F_{13}O_3Si$	Precursor	Sigma-Aldrich	51851-37-7
Ethanol absolute	C_2H_5OH	Solvent	VWR	64-17-5
Ammonium hydroxide ⁴	NH_4OH	Catalyst	Sigma-Aldrich	1336-21-6
Graphene oxide ⁵	$C_xH_yO_z$ ⁶	Nanofiller	CealTech	-

First, de-ionized water was pH adjusted by adding ammonium hydroxide until a pH of approximately 10 was achieved. After this step, one of two viable synthesis routes were used. Route one henceforth referred to as β 1, graphene oxide and DI-water were

⁴28-30%, ACS reagent

⁵10 wt%

⁶Exact composition and sheet size is unknown

mixed directly in the round bottom flask under mechanical stirring. Route two referred to as $\beta 2$, where graphene oxide and water were mixed in a stock solution and sonified before addition to the round bottom flask. The second route assumes monodispersed graphene oxide in the pH augmented water. Table 3.6 categorizes the different amounts of graphene oxide and differentiates $\beta 1$ and $\beta 2$. The graphene oxide weight percent is based upon the amount of β -silane. Regardless of which route used to add graphene oxide, all other reactants remained constant.

Table 3.6: Categorized synthesis and graphene oxide quantities.

Sol-ID	Description	Sol-ID	Graphene oxide [wt.%]
$\beta 1$	Precise mixing, mechanical stirring	$\gamma 0$	0.000
		$\gamma 1$	0.001
$\beta 2$	Stock solution, sonic stirring	$\gamma 2$	0.010
		$\gamma 3$	0.100

The mixed solution of graphene oxide and water was subsequently transferred to a 50 mL two-necked round bottom flask and placed in a bain-marie on top of a RCT hot plate. A magnetic stir bar was then added and magnetic stirring was set to 500 rpm. Consequently a Liebig condenser was mounted on top of the round bottom flask to avert any evaporation loss. A burette was attached onto the round bottom flask to provide a slow dropwise addition on absolute ethanol. The slow addition was applied to maintain a dispersed solution [57]. The solution was allowed to gradually heat with a slow and continuous addition of ethanol until all of the solvent was deposited. This process was conducted until the bain-marie reached 60°C and all of the ethanol was added. Immediately followed by dropwise addition of the precursor via the burette. The solution was left to react at constant temperature and magnetic stirring for 60 minutes. The precise quantity of reactants used are displayed in Table 3.7. After the reaction time was complete, the solution was transferred into a new beaker and immediately spray deposited.

⁷ 1H,1H,2H,2H-Perfluorooctyltriethoxysilane

Table 3.7: Exact quantities used during all coating syntheses. pH varied slightly between syntheses at 10 ± 0.2 .

β -silane ⁷	NH ₄ OH	EtOH	DI water	pH
1.0 mL	5.898×10^{-3} mL	6.086 mL	0.236 mL	≈ 10

3.5 Spray coating

The spray coating were performed by hand utilizing an airbrush manufactured by Cocraft. All coating procedures were performed with a pressure of two bar and a nozzle size of 0.3 mm. Because the procedure was executed by hand, the working distance and deposition angle fluctuates, but were attempted to be kept constant at 10 mm and 45° respectively. Spraying was performed in a constant sweeping motion. Nanoparticle deposition was optimized to create a thin uniform layer. One layer of nanoparticles was decided as the optimal number based on images included in Appendix A. All samples containing β_1 or β_2 coating received eight layers of spray deposition. Where a layer is defined as one sweep across the surface with the parameters supplied in Table 3.8. The β_1 and β_2 solutions were diluted 1:1 with absolute ethanol under heavy mechanical stirring before deposition. To expedite the evaporation and increase adhesion, substrates were heated on a RCT Basic hotplate.

Table 3.8: Spray coating parameters.

Sol-ID	Working distance [mm]	Angle ⁸	Substrate temperature [°C]	Layers
NP1 & NP2	≈ 10	$\approx 45^\circ$	60	1
β_1 & β_2	≈ 10	$\approx 45^\circ$	60	8

⁸Angle of the airbrush during deposition

3.6 Heat treatment

Immediately after spray deposition, substrates were placed onto alumina trays and heat treated in an Carbolite Gero PF60 oven. The temperature was measured and controlled by a R38, PID, controller. Depending on the type of solution deposited a specific heating program were followed to evaporate water and remaining solvent. These programs are outlined in Table 3.9. The alumina trays were placed in the middle of the oven to minimize heat gradients.

Table 3.9: Heat treatment parameters.

Sol-ID	Temperature [°C]	Time [min]
NP1	100	60
NP2	100	60
β 1	150	300
β 2	150	300

3.7 Characterization

Surface and roughness characteristics were identified by SEM, profilometer and white light interferometry. While synthesized solutions were characterized by viscosity measurements. Final coating attributes were identified through contact angle and icing measurements.

3.7.1 Roughness

A Veeco Dektak 150 profilometer was used to investigate the substrate roughness. Three substrates were measured with five scans across 2000 μm and 4000 μm each. Sampling rate was kept constant, providing 9000 and 18000 data points for the different scan lengths. Stylus radius and force, were set to 12.5 μm and 3mg respectively and kept constant. Measurement range was adjusted to 65.5 μm and the surface profile was set to "Hills&Valleys".

To achieve topographical image and a 3D visual presentation of the surface textures, a Contour GT-1 produced by Bruker was used. Countour GT-1 is an optical non-contact profilometer using white-light interferometry. Each surface type was scanned using vertical scanning settings. 3D images were plotted using the Contour GT-1 software. Average roughness, standard deviation, skewness and kurtosis were coded and calculated in Python 3.7. Codes used are included in the Appendix D.

3.7.2 Viscosity

To quantify the viscosity of synthesized solutions, a HAAKE MARS III rheometer was utilized. A 1.85 mL dose was administered to the rheometer and investigated under shear stress. The shear stress were both increased and decreased linearly and the viscosity was averaged across 100 measurements. Identical measurement programs were used for all tested solutions, a detailed program is supplied in Table 3.10. To approximate ambient temperature during spray deposition, the temperature was set to 25°C.

Table 3.10: Program parameters used during HAAKE MARS III measurements.

Step	Shear rate [1/s]	Time [s]	Temperature [°C]	Measurements
Rot Ramp	0.01 – 500.00	180	25	100
Rot Time	500.00	30	25	100
Rot Ramp	500.00 – 0.01	180	25	100

3.7.3 Surface characterization and nanoparticles

Images of the topography was captured with a Field Emission Scanning Electron Microscope, abbreviated as FESEM. The FESEM used was an Ultra 55 edition manufactured by Zeiss. Images were taken with accelerating voltage of 10keV. To acquire a good depth of field, the working distance was set between 5 – 10 mm. All images presented in this thesis were captured with an aperture size of at 30µm. To achieve high resolution topographical images secondary electrons were captured with a ET detector with a 300V bias.

Nanoparticles were characterized using high resolution images from the FESEM. Images

were processed using an open sourced software called Image J and calculated using codes written in Python 3.7. Several images were measured and averaged in order to acquire the average particle size. Both automatic and manual measurements were performed in the Image J software.

3.7.4 Coating thickness

Coating thickness was estimated using a Veeco Dektak 150 profilometer. Two samples were measured several times to acquire the coating topography. Subsequently a small incision was made using a copper nail. The topographies from the pre-incision and post-incision were superimposed over each other to estimate the thickness. A copper nail was used since its tensile modulus is high enough to break the polymer coating but low enough to avoid deformation in the steel microstructure. γ 0- β 1-NP0 and γ 2- β 2-NP0 were examined and assumed to be representative for all β 1 and β 2 coatings since they all followed an identical spray coating regime.

The substrate were measured a scan length of 500 μ m, with a high sampling rate of 18000 data points to achieve a high accuracy. The measurements range was reduced to 6.5 μ m while stylus radius and force, were set to 12.5 μ m and 3mg respectively.

3.7.5 Coating tribology

To assess the coatings resistance to wear, a pin on plate experiment was performed. The test were performed by SINTEF on a TE105 Long Stroke Low Load Reciprocating Machine. A steel ball, pin, is lowered with a constant applied force of 1 N against the coating mounted on a reciprocating plate with a frequency of 1 Hz. The coefficient of friction is automatically calculated by Pheonix Tribology software. Table 3.11 presents an overview of tribology parameters.

Table 3.11: Parameters used during tribology measurements.

Applied load [N]	Pin radius [mm]	Frequency [Hz]	Run time [s]
1	3	1	60

3.8 Contact angle measurements

Contact angle, roll-off angle and contact angle hysteresis were measured using a Drop Shape Analyzer - DSA 100 manufactured by Krüss. All measurements were conducted with DI-water under ambient conditions. Sessile drop mode was utilized to deposit the droplet and the Young-Laplace fitting mode was used to calculate the static contact angle. Young-Laplace fitting mode was selected to minimize pixel errors consequently giving a more precise measurement [71].

The samples were mounted using carbon adhesive tape to prevent sliding during tilting. To avoid any skewness the substrate was carefully centered on top of the adhesive tape. Subsequently the stage was adjusted until the substrate and high speed camera were aligned. Focus, brightness and zoom were manually optimized to yield a sharp and clear image. Successively, a 8 μL droplet was deposited onto the substrate while a high speed camera recorded the process. The baseline could be set automatically, but due to instrument inconsistencies, the baseline was set manually to achieve more accurate measurements. Directly after deposition the ADVANCE software would use the fitting method and baseline to calculate the static contact angle.

To minimize possible errors, an automated deposition and measurement program was constructed. The program collected 20 measurements within the first 10 seconds of deposition. Three different areas on each substrate was investigated to estimate coating consistency. Providing a total of 60 CA measurements for each substrate. Figure 3.3a displays a droplet evaluated by the Young-Laplace fitting mode.

To investigate the dynamic contact angles, CAH and ROA, the instrument was tilted 90° . Similar to the static contact angle measurements, a 8 μL droplet was deposited ensued by tilting at a constant rate of $60^\circ/\text{min}$. During tilting the dynamic contact angle was calculated twice per second. Due to the tilting of the instrument and the asymmetry of the droplet, a tangential fitting mode was used. This fitting mode was selected to obtain high contact angle precision [71].

The automated tilting and measurement process was created in the ADVANCE software. After the automated program was finished, each recording was reviewed and the ROA

was registered. CAH was calculated by Eq. 2.5, based on the advancing and receding contact angle of the last measurement before the ROA. Three droplets was deposited on each substrate and evaluated separately. Figure 3.3b displays a droplet evaluated by the Tangent fitting mode.

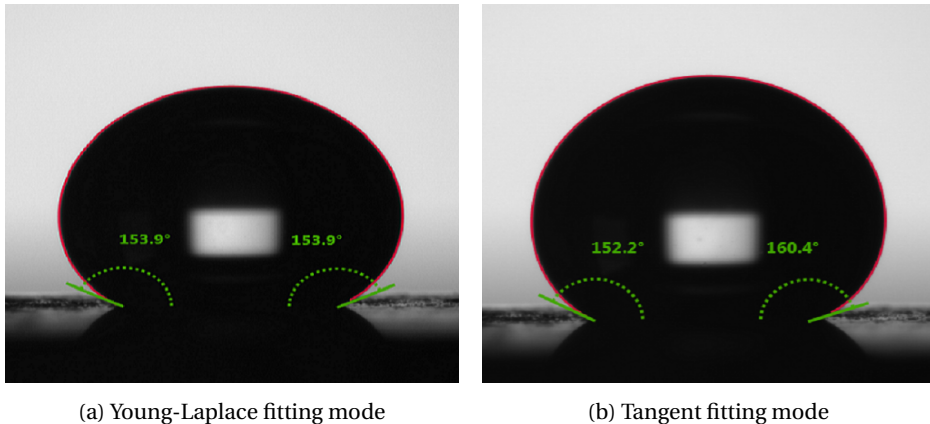


Figure 3.3: A comparison of the fitting modes used during contact angle measurements. The red boundaries delineate the detected droplet boundary. Young Laplace was used during static CA measurements while Tangent was used during dynamic CA measurements.

3.9 Environmental experiments

To explore the anti-icing capabilities of the coatings they were investigated in three different manners. Nucleation temperature, nucleation delay and cyclic behaviour. All icing experiments were conducted using a TC40 environmental chamber mounted on the DSA 100 stage. A Julabo F12-MA cooling circulator was used to cool the environmental chamber. Samples were inserted into the chamber and covered with a thermal conductive hood to minimize temperature gradients. A temperature sensor was inserted into the chamber and was used as the temperature reference. Due to the static nature of the icing-experiments, the Young-Laplace fitting mode was utilized.

3.9.1 Energy barrier for ice nucleation

The energy barrier for ice nucleation was examined by depositing a 8 μ L droplet and gradually decreasing the temperature. The droplet was deposited at a controlled temperature of 5 $^{\circ}$ C and successively lowered 1 $^{\circ}$ C/min until nucleation. Contact angles were measured each minute until ice formation occurred. When ice nucleation was initiated, the temperature was recorded. Ice nucleation could be detected by examining volume or color changes during the experiment.

3.9.2 Nucleation delay

The nucleation delay was measured at -10 $^{\circ}$ C. This temperature was selected based on the ice nucleation results. Only the best performing coatings for each γ -group were investigated. The samples were loaded individually into the environmental chamber and cooled down to -10 $^{\circ}$ C where it was held until the substrate had reached the desired temperature. The temperature sensor was placed on the substrate to confirm the temperature. Approximately 10 minutes was sufficient to cool the substrate. Subsequently a 8 μ L droplet was deposited and the time interval until the droplet froze was recorded.

3.9.3 Durability

To examine coating durability several icing/deicing cycles were executed. The best performing samples for each γ -group was tested. A 8 μ L droplet was deposited at 15 $^{\circ}$ C and gradually lowered at a rate of 1 $^{\circ}$ C/min. The contact angle was recorded as the temperature decreased until ice nucleation transpired. After ice formation, the temperature was noted and the chamber was reheated to 5 $^{\circ}$ C to deice the droplet. The environmental chamber was kept at 5 $^{\circ}$ C until the droplet was completely deiced. This process was repeated three times to examine changes in the contact angles.

3.10 Sample summary

All samples can be identified by their parameter tags. Each sample is represented by three tags, γ , β and NP followed by an identifying number. γ is used to convey the amount of graphene oxide. The subsequent number indicate the exact graphene oxide content. The corresponding numbers and content can be seen in Table 3.6 and Figure 3.4. The wt% is based on the amount of 1H,1H,2H,2H-Perfluorooctyltriethoxysilane precursor.

The β symbol is used to identify the coating synthesis method. Coatings with the β 1-tag, all reactants were mixed directly into the round bottom flask under mechanical stirring during synthesis. For coatings with the β 2-tag, graphene oxide and water was mixed in a stock solution based on the stoichiometric relation in Table 3.5. Sonication was used to obtain a dispersed stock solution. The correct amount of GO and water successively extracted from the stock solution and used in the synthesis.

The NP identifier is used to determine the nanoparticle size deposited on the substrate. Increasing numbers indicates a larger size. When no nanoparticles are present, the NP0 tag is used. A rule of thumb is to connect higher numbers with higher content or larger size. A descriptive figure is provided in Figure 3.4.

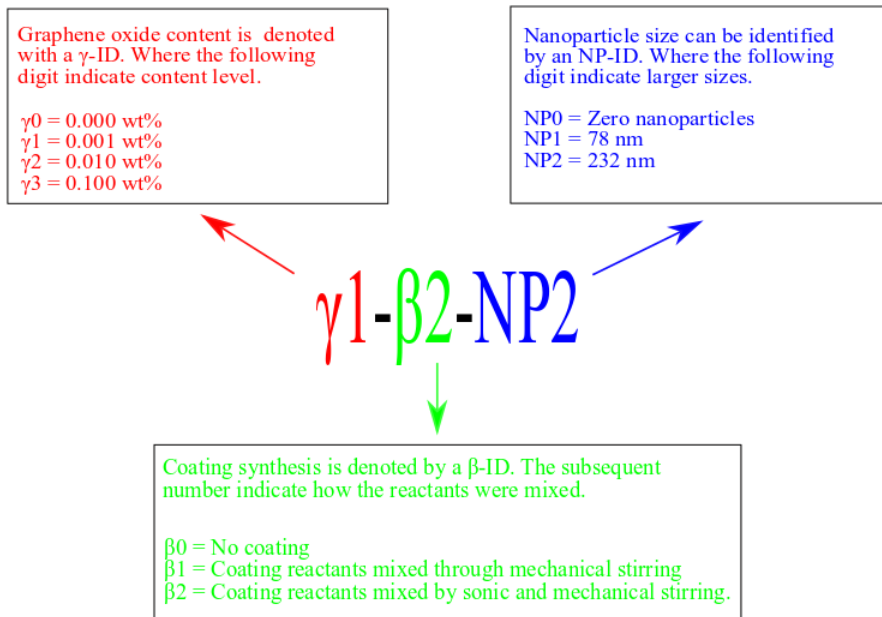


Figure 3.4: An explanation of how the samples are named and identified. In the given example above, the $\gamma 1-\beta 2-NP 2$ signifies a sample with nanoparticles sized 232 nm. With a fluorosilane-based coating containing 0.001 wt% graphene oxide mixed with mechanical and sonic stirring.

Chapter 4

Results

4.1 Microroughness

Table 4.1 presents average roughness, skewness and kurtosis calculated by Equation 2.10, 2.11 and 2.13 respectively. Standard deviation of average roughness is expressed as σ_{Ra} . All values presented are arithmetic averages of the total compiled data. Figure 4.1 illustrate a qualitative presentation of the untreated surface topography.

Table 4.1: A quantitative comparison of two measurement lengths. Average profile roughness, skewness and kurtosis are calculated from values obtained during profilometry on the untreated substrates.

Measurement length	R_a	σ_{Ra}	R_{sk}	R_{ku}
2000 μm	0.171 μm	0.037 μm	-0.432	7.703
4000 μm	0.239 μm	0.086 μm	-0.249	12.555

A relatively low average roughness profile was measured. By inspecting Figure 4.2b, a smooth surface with deep crevices between flat plateaus are observed. In addition, surface deformation can be observed by irregularities and straight lines across the surface. The deformation is evident when inspecting Figure 4.2a. The prevalence of crevices is confirmed by the negative skewness presented in Table 4.1. The high kurtosis calculated for both measurement lengths suggest a narrow height distribution i.e a high

accuracy of the average roughness. This data complements the plane surfaces observed in Figure 4.2.

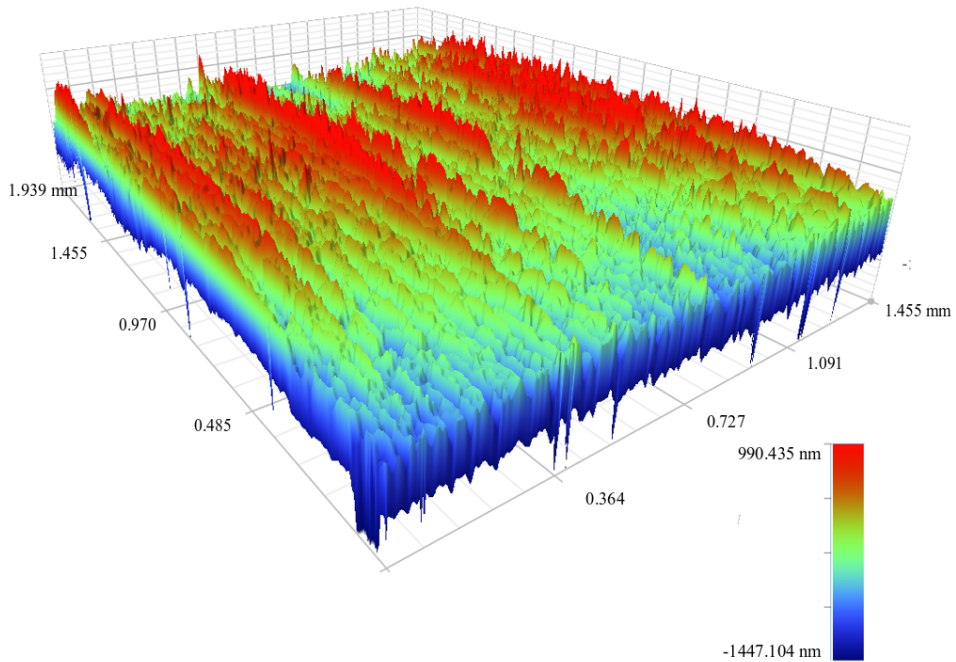
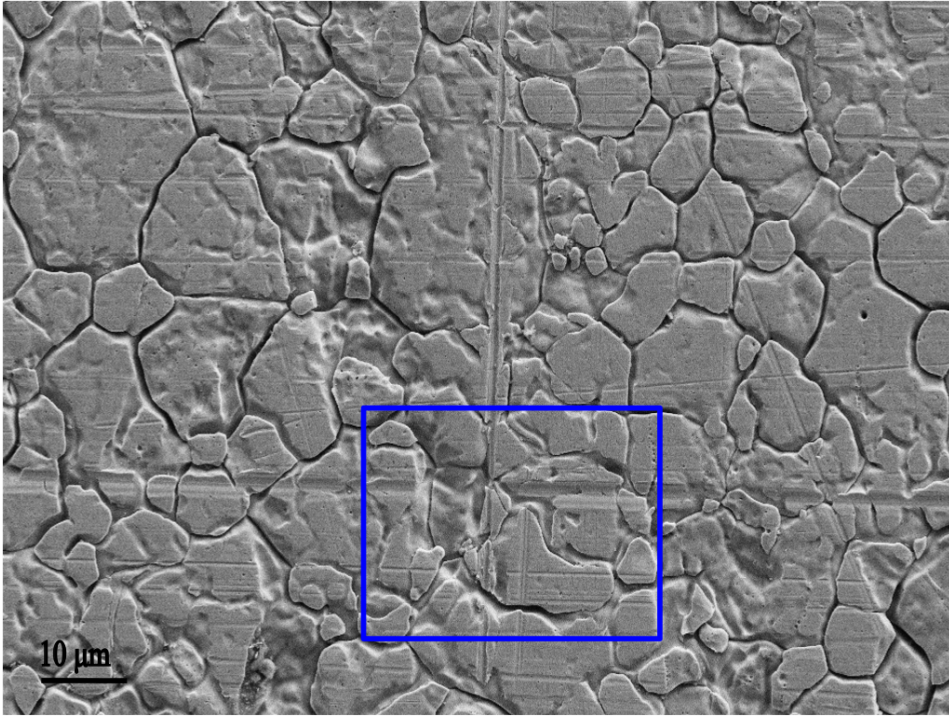
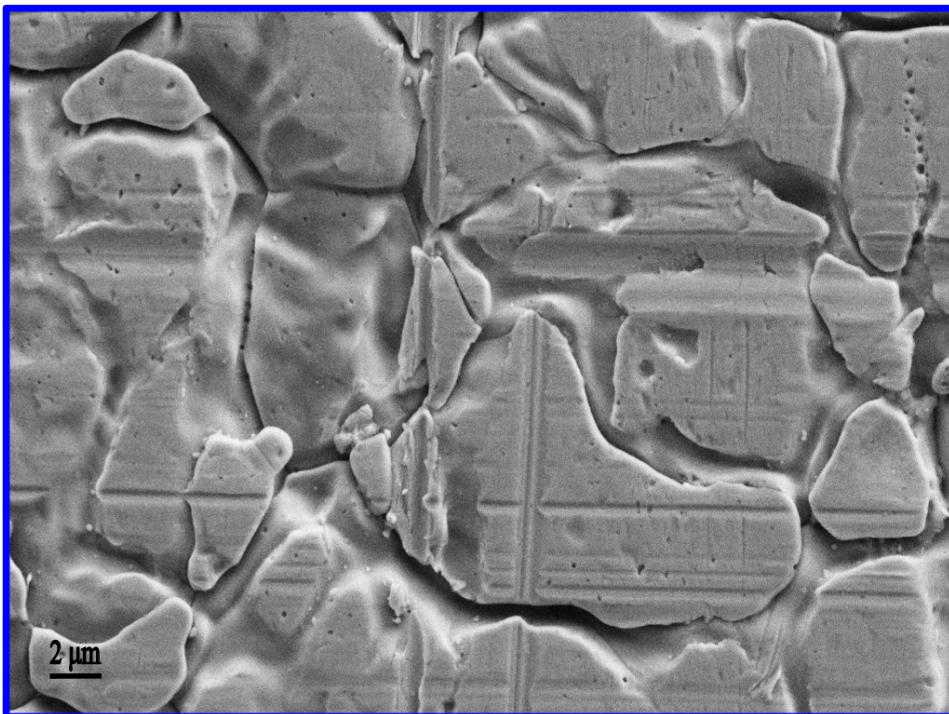


Figure 4.1: A qualitative 3D presentation of the surface texture measured with a Contour GT-1.



(a) SEM overview of a γ_0 - β_0 -NP0 sample.



(b) Magnified SEM image of a γ_0 - β_0 -NP0 sample.

Figure 4.2: SEM images of a γ_0 - β_0 -NP0 sample. The blue square in Figure 4.2a indicate the image boundary of Figure 4.2b.

4.2 Rheology

Viscosity for each solution was averaged over 100 measurements at a constant shear rate. The results are tabulated in Table 4.2. All $\beta 1$ and $\beta 2$ solutions were diluted 1:1 with absolute ethanol. Consequently the solutions have high percentages of absolute ethanol and will result in similar viscosities.

Table 4.2: A summary of the measured viscosities. All viscosities are measured at 25°C.

Sol-ID	η [mPa · s]
NP1	1.66
NP2	1.69
$\gamma 0$ - $\beta 1$	1.12
$\gamma 1$ - $\beta 2$	1.07
$\gamma 2$ - $\beta 2$	0.99
$\gamma 3$ - $\beta 1$	0.91
$\gamma 3$ - $\beta 2$	0.98

4.3 Nanoparticles

The average particle size for the NP1-batch was found to be 78 nm with a standard deviation of 8 nm. The NP1-batch demonstrates a homogeneous and uniform particle size, this is confirmed by Figure 4.5a. The NP2-batch contains slightly larger particles with an average particle size of 232 nm and a standard deviation of 32 nm. The high standard deviation reflects a varied particle size, which can be seen by inspecting Figure 4.5b. Particle sizes are summarized in Table 4.3. Figure 4.5 displays a comparison of a NP1 sample and a NP2 sample imaged at identical magnification.

Clusters of nanoparticles were observed on all NP1 and NP2 samples. These clusters were rare and varied in size on all samples. These clusters are aggregated nanoparticles forming large spheres. Figure 4.3 and Figure 4.4 presents nanoparticle clusters on a NP1 and NP2 sample respectively. Additional nanoparticle images are included in the Appendix B.

Table 4.3: A summary of the respective nanoparticle sizes

Sol-ID	Average particle size	Standard deviation
NP1	78 nm	8 nm
NP2	232 nm	32 nm

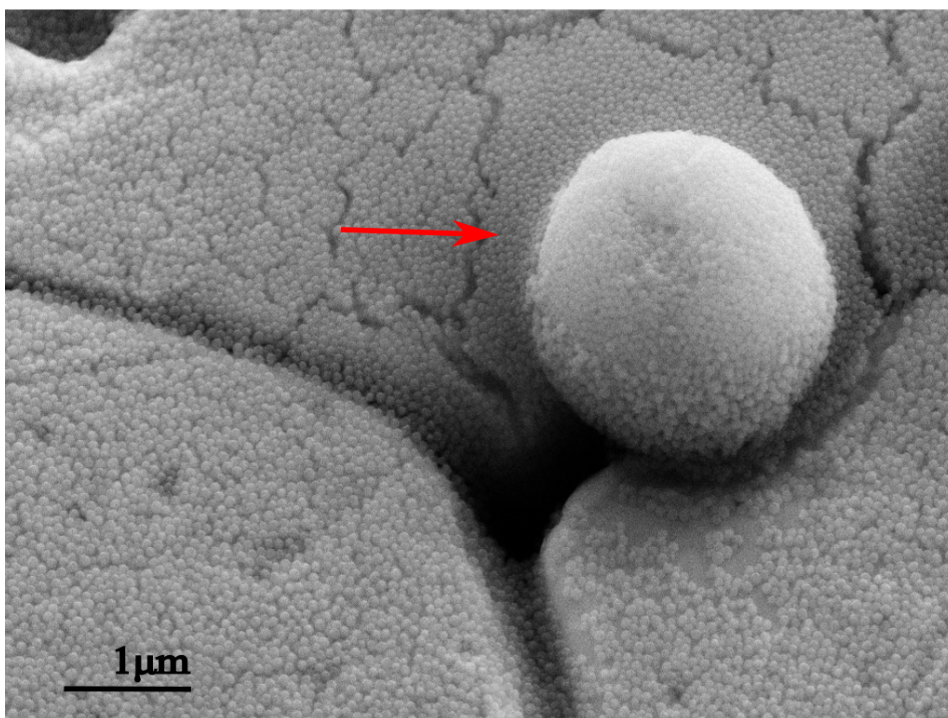


Figure 4.3: A nanoparticle cluster found on a $\gamma_0\text{-}\beta_0\text{-NP1}$ sample. The cluster is indicated by a red arrow.

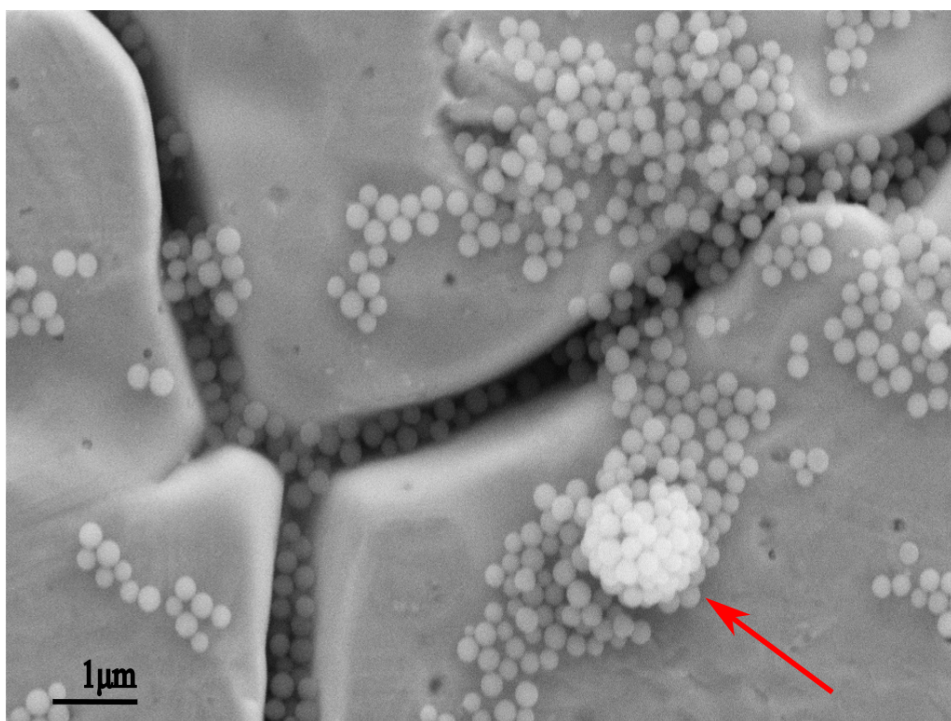
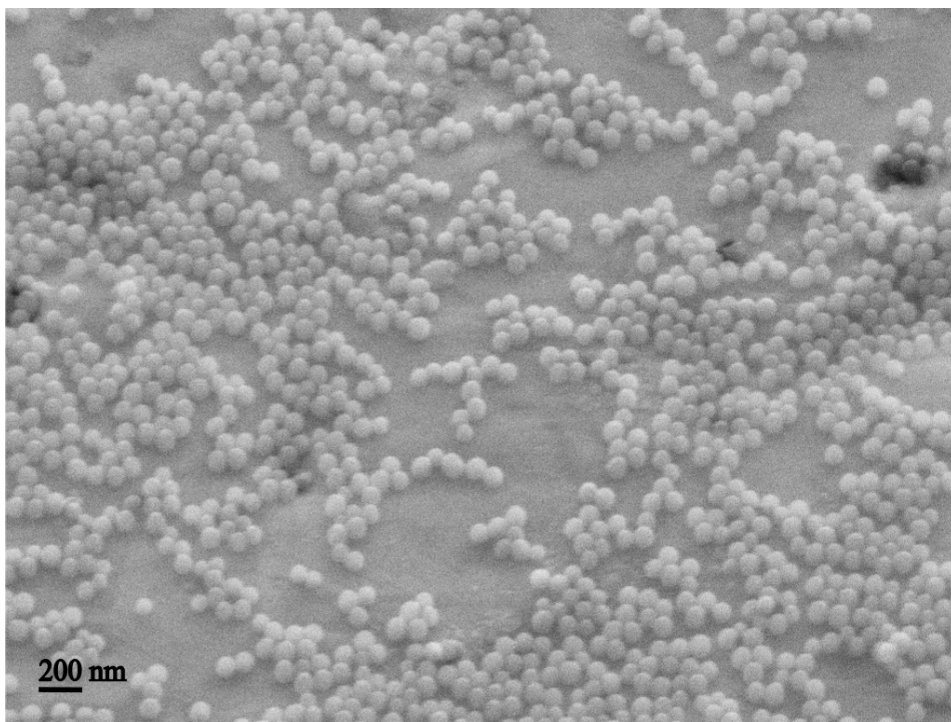
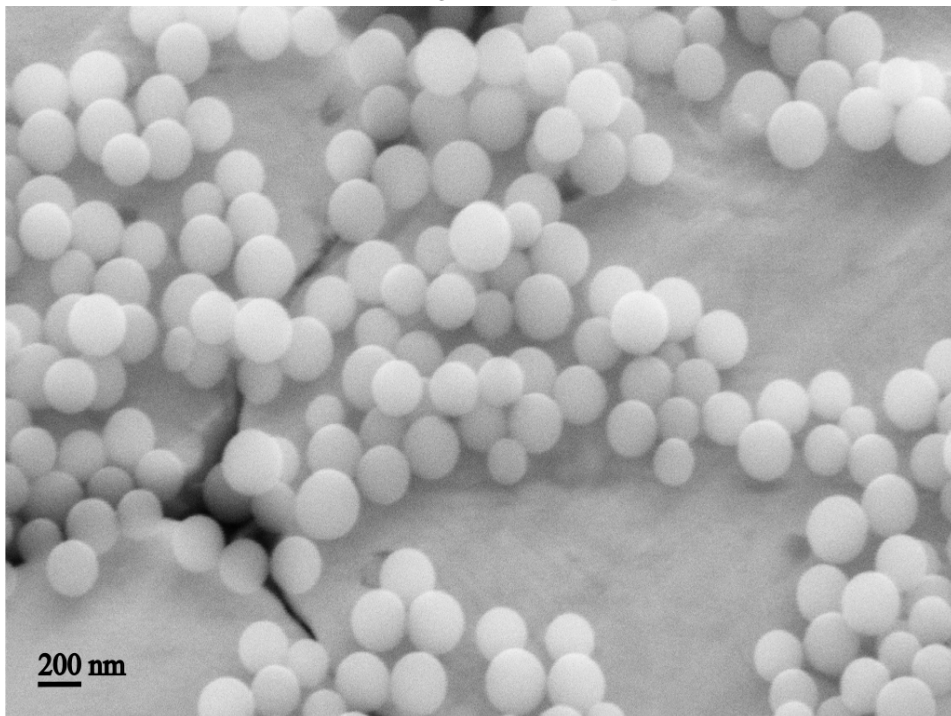


Figure 4.4: A small cluster discovered on a γ_0 - β_0 -NP2 sample. The cluster is highlighted by a red arrow.



(a) SEM image of an NP1-sample.



(b) SEM image of an NP2-sample.

Figure 4.5: A comparison of the different nanoparticles imaged at identical magnifications. To improve the resolution both images is taken at a 40° angle.

4.4 Nanoparticle deposition

By inspecting Figure 4.7a, a thin particle layer can be observed on the γ 0- β 0-NP1 sample. In Figure 4.7b, an especially high coverage is observed in the crevices, these particles are also highly ordered. On the plane plateaus, the particles are less ordered and randomly distributed. This phenomena can be observed in both Figure 4.7 and 4.8. In Figure 4.8, a high degree of particle coverage on a γ 0- β 0-NP2 sample can be observed. Particle layer thickness ranges between one and three particles across the majority of the samples, which can be seen in Figure 4.5b and 4.8b and images included in Appendix B. A good particle coverage was observed for all samples. Both NP1 and NP2 samples demonstrate a higher particle density in crevices compared to peaks.

On several NP2-samples, very large nanoparticle buildups were observed as presented in 4.6. In these buildups, the particles aggregated to form thick nanoparticle layers across the surface.

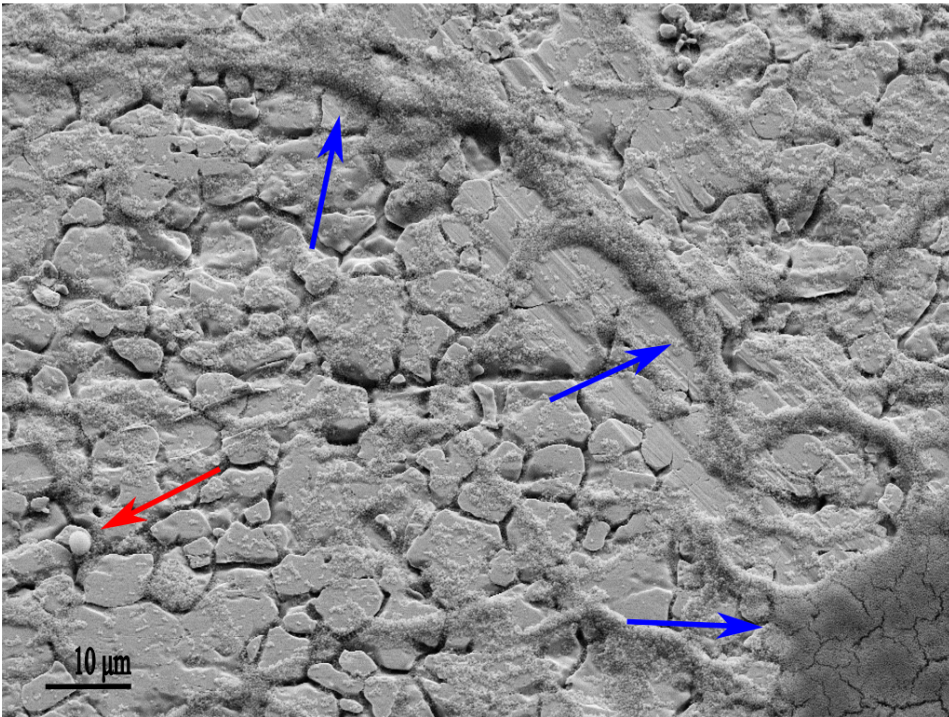
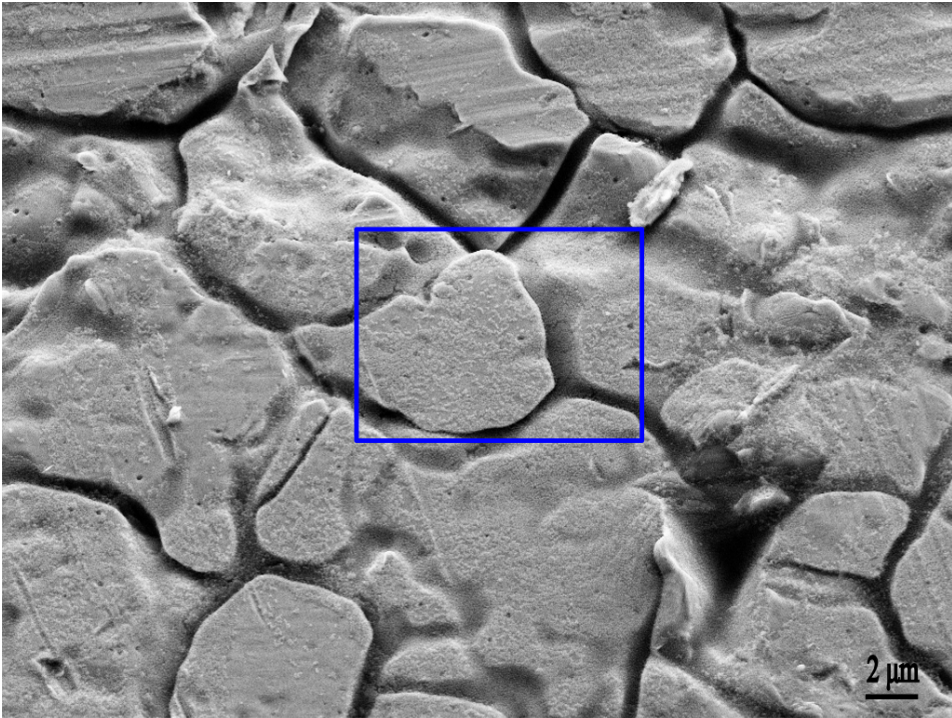
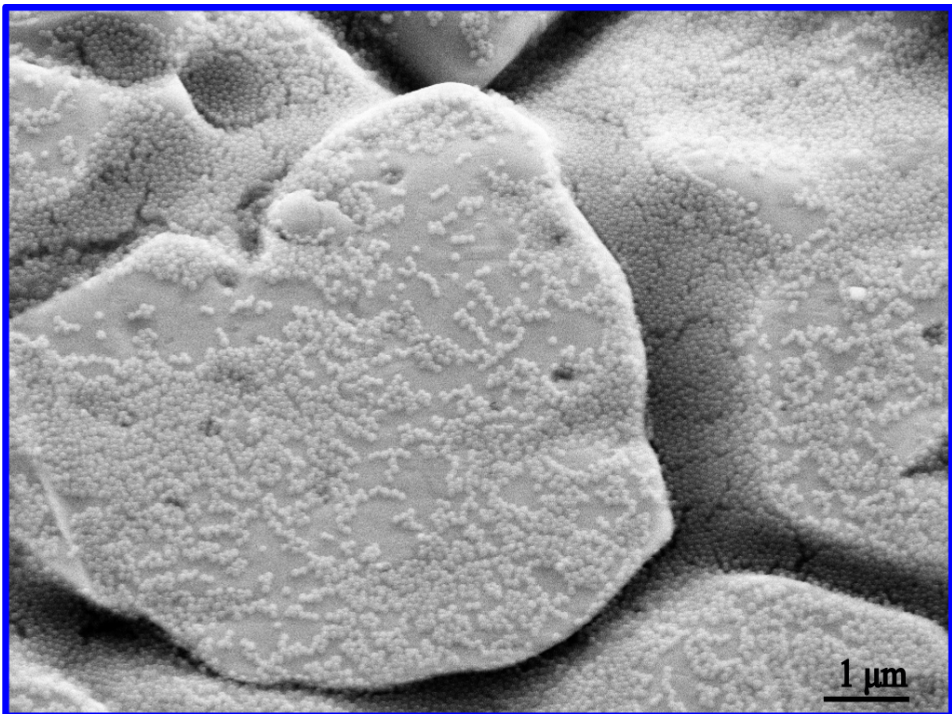


Figure 4.6: An overview image of a $\gamma_0\text{-}\beta_0\text{-NP2}$ where large nanoparticle buildups can be observed. Particle buildups are indicated by the blue arrows while a large particle cluster is indicated by the red arrow.

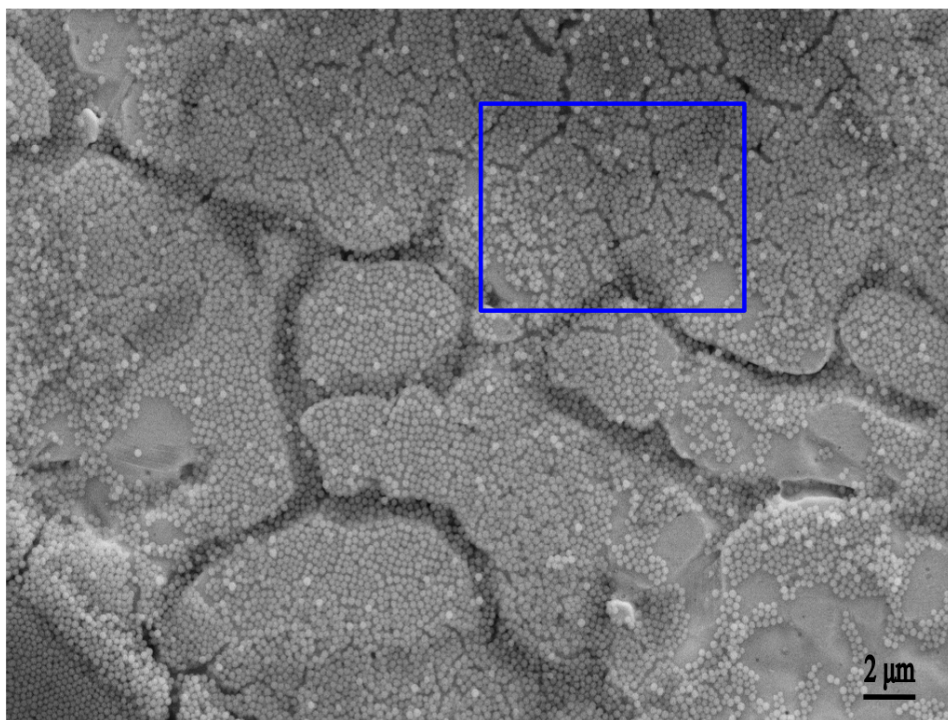


(a) SEM overview of an γ_0 - β_0 -NP1 sample.

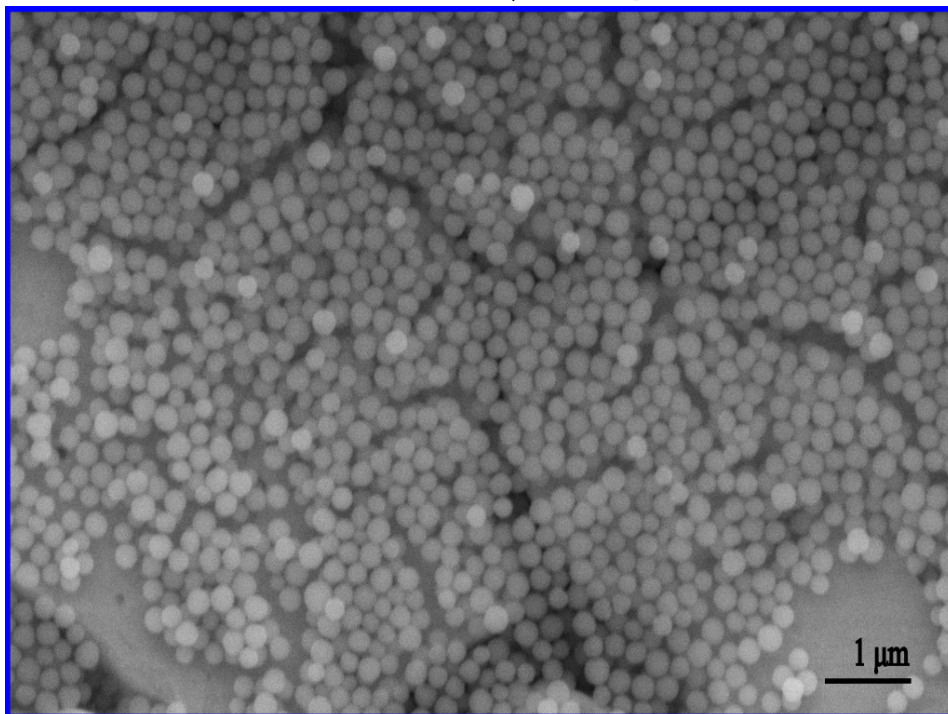


(b) A magnified image of the particle coverage on a γ_0 - β_0 -NP1 sample.

Figure 4.7: SEM images of a γ_0 - β_0 -NP1 sample. The blue square in Figure 4.7a indicate the image boundary of Figure 4.7b. Both images are captured at 40° angle.



(a) Overview of an γ_0 - β_0 -NP2 sample.



(b) A magnified image of the particle coverage on a γ_0 - β_0 -NP2 sample.

Figure 4.8: SEM images of a γ_0 - β_0 -NP2 sample. The blue square in Figure 4.8a indicate the image boundary of Figure 4.8b.

4.5 Coating characterization

4.5.1 Thickness

Coating thickness was estimated to be $2.05 \pm 0.37 \mu\text{m}$. Figure 4.9 demonstrates a topography measurement before and after incision superimposed over each other. The difference between the lowest point of the cut compared to pre-cut was estimated to be the coating thickness. This value was averaged for all measurements made. The smaller crevices are assumed to be natural variations in the coating while the large hills on either side of the cut-crevice are estimated to be excess coating.

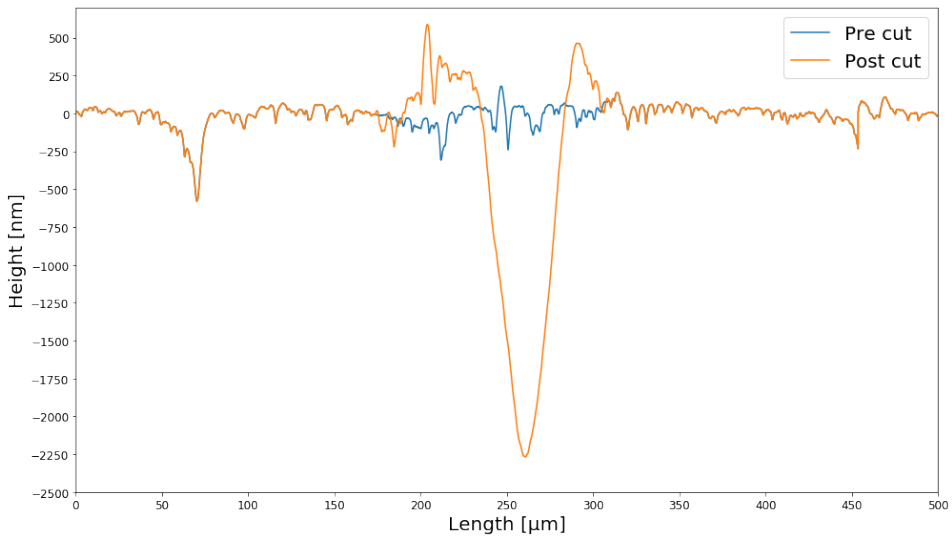


Figure 4.9: A topography measurement of a $\gamma 0$ - $\beta 1$ -NP0 sample before and after a tiny incision was made. The depth of the cut indicates the coating thickness.

4.5.2 Graphene oxide

A critical task was to incorporate the graphene oxide into the polymer coating and exploring the behaviour of GO. From Figure 4.10 GO can be observed as sheets draped across the surface, covering the nanoparticles. To verify the sheets stretched across the surface as GO, a γ 2- β 0-NP0 sample was examined as a reference. The γ 2- β 0-NP0 sample in Figure 4.11 can visually confirm how graphene oxide looks and behaves when deposited. GO sheets have a tendency to form wrinkles, which are indicated by the red arrows in Figure 4.11. These wrinkles can also be found in Figure 4.10. As a result we can conclude with a successful GO deposition on the steel surface. Additional images of coatings containing graphene oxide are included in Appendix C.

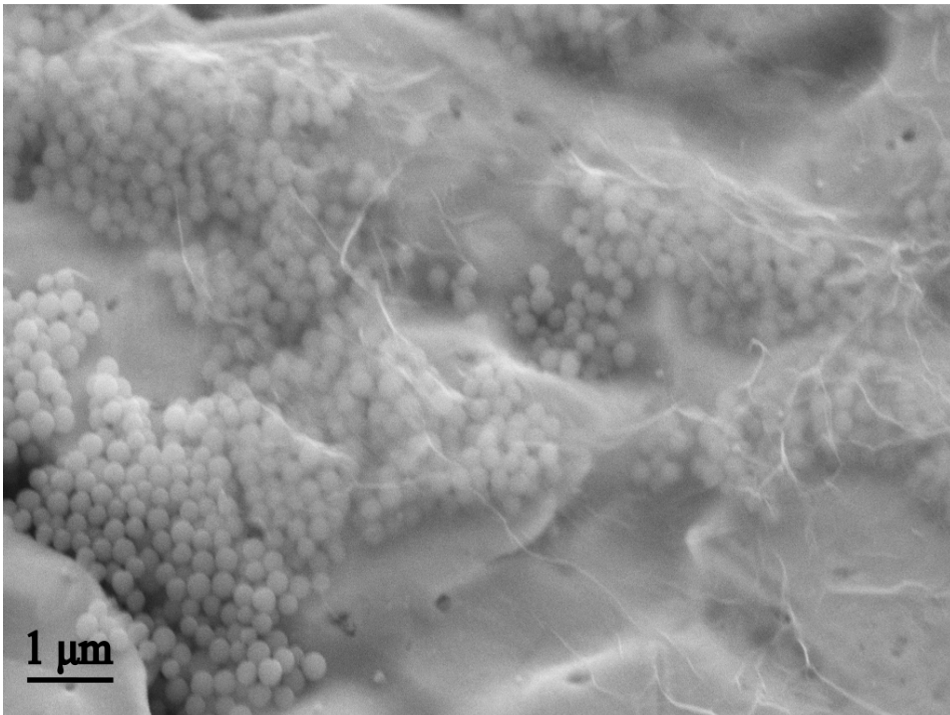


Figure 4.10: An overview image of GO sheets covering the nanoparticles in a γ 2- β 2-NP2 sample.

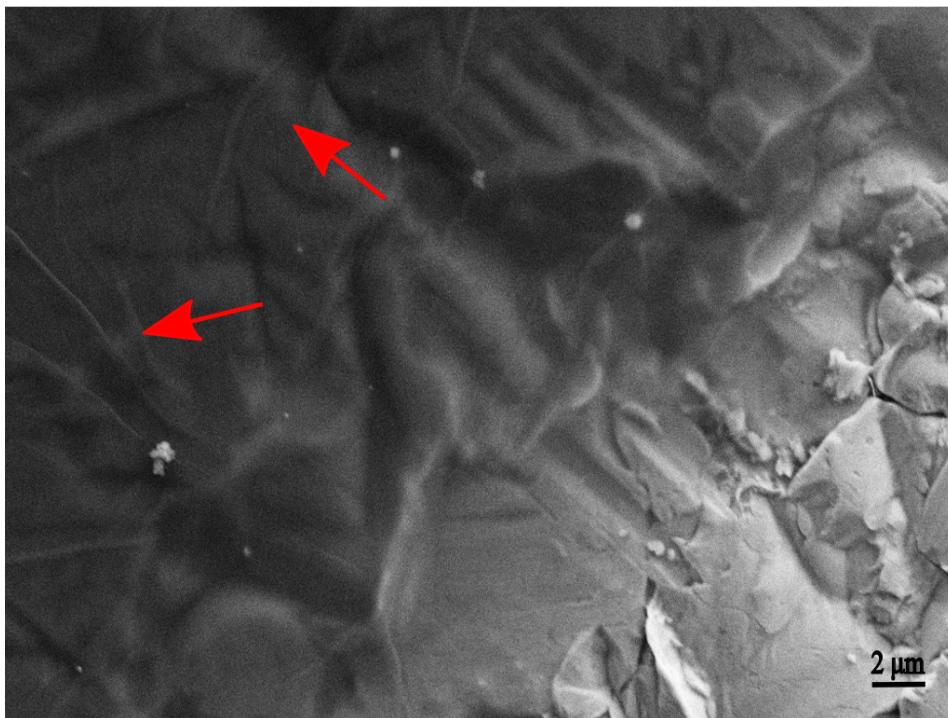
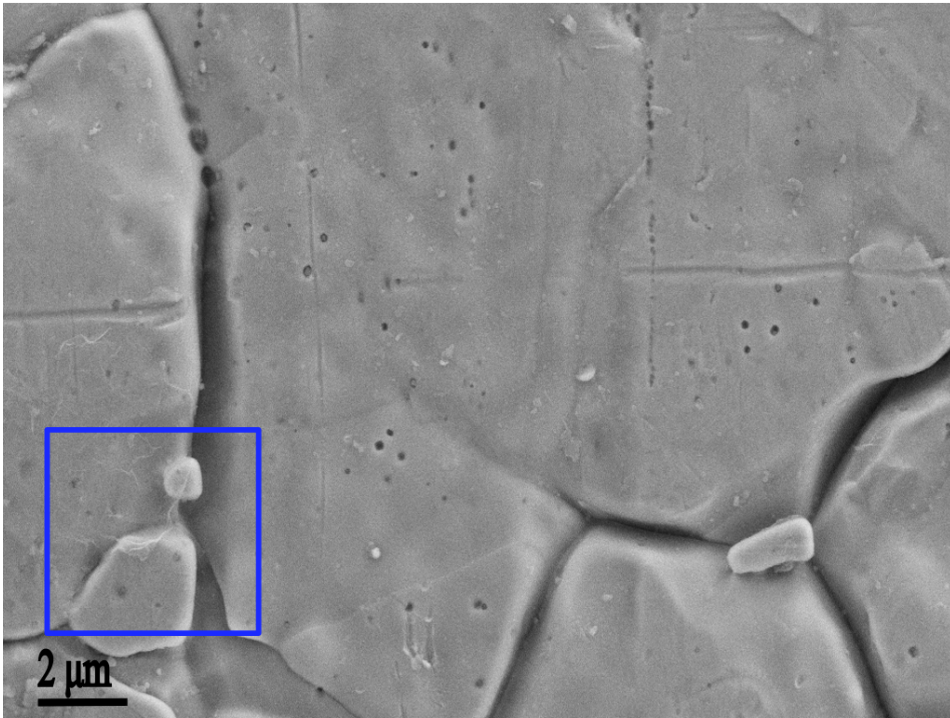


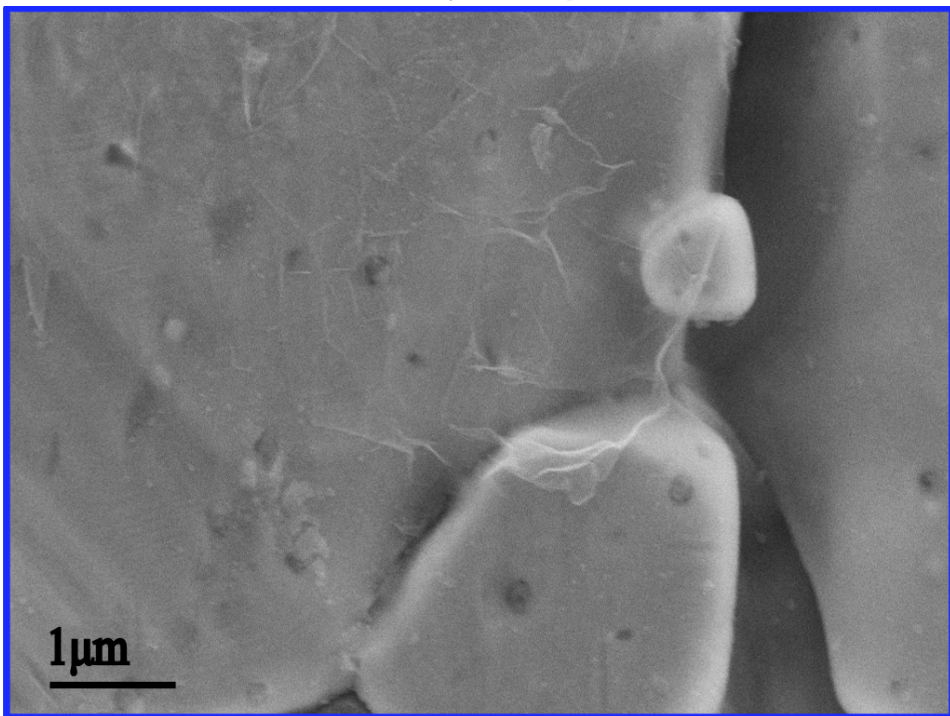
Figure 4.11: The $\gamma 2$ - $\beta 0$ -NP0 sample is partially coated with GO. This partial coating was done to easily distinguish between the GO and steel. The dark area contains a high concentration of GO, while the light grey area is uncoated. The red arrows indicate folded/crumpled graphene oxide sheets.

On all coatings containing GO, the GO sheets were observed randomly scattered across the surface independent of GO content. Figure 4.12a presents an area with a low amount of GO sheets on a $\gamma 3$ - $\beta 1$ -NP0 sample. By inspecting Figure 4.12b we can observe what appears to be a singular sheet. But without knowing the sheet size of the GO provided, we are unable to discern whether the GO sheet in Figure 4.12b is one singular sheet or several inter-layered sheets.

An attraction between nanoparticles and the GO sheets was observed. On all samples containing nanoparticles, the majority of GO were found draped over or wrapped around the nanoparticles. This phenomena can be observed in Figure 4.13. The blurred stripes in Figure 4.13 can be identified as graphene oxide sheets.



(a) An overview image of a $\gamma_3\text{-}\beta_1\text{-NP0}$ sample, where a singular GO sheet can be spotted, indicated by the blue square.



(b) A zoomed in image of the GO sheet on a $\gamma_3\text{-}\beta_1\text{-NP0}$ sample.

Figure 4.12: A $\gamma_3\text{-}\beta_1\text{-NP0}$ sample demonstrating a low presence of GO sheets. The blue square in Figure 4.12a indicate the image boundary of Figure 4.12b

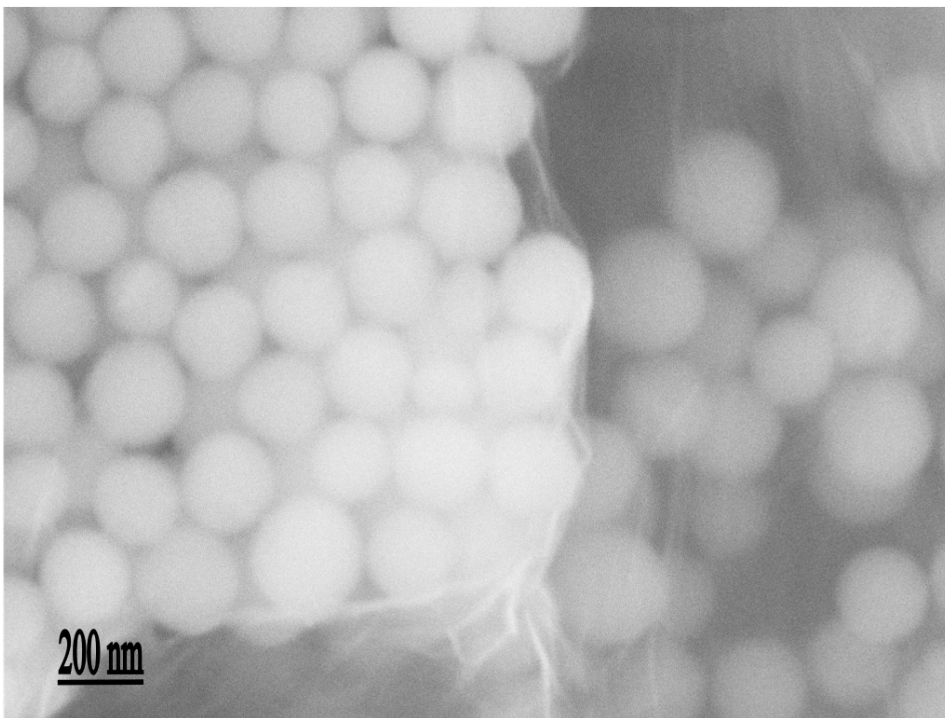


Figure 4.13: An image of a γ_1 - β_2 -NP2 sample where graphene oxide sheets can be seen wrapped around the nanoparticles.

4.6 Wetting

All contact angle measurements are tabulated and categorized in Table 4.4. The untreated steel sample, γ_0 - β_0 -NP0 was measured as a reference. From Table 4.4 we can observe an increase in hydrophobicity due to β_1 and β_2 additions. The coatings demonstrating the highest hydrophobic character was sample γ_1 - β_2 -NP2 and γ_2 - β_2 -NP2. Figure 4.14 demonstrate a decreasing contact angle with increasing amounts of GO, for coatings containing nanoparticles. No distinguishable trend can be seen from the coatings without nanoparticles. These coatings seems to be unaffected by increasing GO content based on Figure 4.14. A surprising result is the graphene oxide content seems have little effect on contact angles considering all samples containing graphene oxide performed better than samples without.

Table 4.4: CA, CAH and ROA measurements for all samples. If a 90° tilt was reached without the droplet rolling off, ROA and CAH are registered as $> 90^\circ$ and N/A respectively.

Sample ID	CA [$^\circ$]	ROA [$^\circ$]	CA _{adv} [$^\circ$]	CA _{rec} [$^\circ$]	CAH [$^\circ$]
$\gamma 0\text{-}\beta 0\text{-NP0}$	82 ± 6	> 90	N/A	N/A	N/A
$\gamma 0\text{-}\beta 0\text{-NP1}$	119 ± 1	> 90	N/A	N/A	N/A
$\gamma 0\text{-}\beta 0\text{-NP2}$	86 ± 8	> 90	N/A	N/A	N/A
$\gamma 0\text{-}\beta 1\text{-NP0}$	114 ± 3	> 90	N/A	N/A	N/A
$\gamma 0\text{-}\beta 1\text{-NP1}$	140 ± 2	> 90	N/A	N/A	N/A
$\gamma 0\text{-}\beta 1\text{-NP2}$	143 ± 2	> 90	N/A	N/A	N/A
$\gamma 1\text{-}\beta 2\text{-NP0}$	114 ± 3	> 90	N/A	N/A	N/A
$\gamma 1\text{-}\beta 2\text{-NP2}$	152 ± 3	46 ± 9	163 ± 4	112 ± 14	50 ± 17
$\gamma 2\text{-}\beta 0\text{-NP0}$	10 ± 2	> 90	N/A	N/A	N/A
$\gamma 2\text{-}\beta 2\text{-NP0}$	127 ± 5	> 90	N/A	N/A	N/A
$\gamma 2\text{-}\beta 2\text{-NP2}$	150 ± 4	79 ± 7	159 ± 10	137 ± 3	23 ± 9
$\gamma 3\text{-}\beta 1\text{-NP0}$	127 ± 4	> 90	N/A	N/A	N/A
$\gamma 3\text{-}\beta 1\text{-NP1}$	143 ± 3	> 90	N/A	N/A	N/A
$\gamma 3\text{-}\beta 2\text{-NP0}$	113 ± 6	> 90	N/A	N/A	N/A
$\gamma 3\text{-}\beta 2\text{-NP2}$	136 ± 7	> 90	N/A	N/A	N/A

Coatings containing nanoparticles systematically exhibited improved hydrophobicity. On average the NP1 particles increased the contact angle by $21^\circ \pm 5^\circ$ compared to identical NP0 samples. While the larger NP2 particles, showed an average contact angle improvement by $28^\circ \pm 7^\circ$ compared to NP0 samples. Providing a basis for the claim that larger particles have higher effect on the CA.

Figure 4.15a provides a visual demonstration of the hydrophilic nature of graphene oxide. This high degree of wetting confirms expectations from literature [57]. After encapsulating the graphene oxide into the polymer coating, this hydrophilic nature can be negated and in cohesion with nanoparticles a hydrophobic coating can be created. Figure 4.15b presents $\gamma 2\text{-}\beta 2\text{-NP2}$ sample demonstrating a superhydrophobic contact angle.

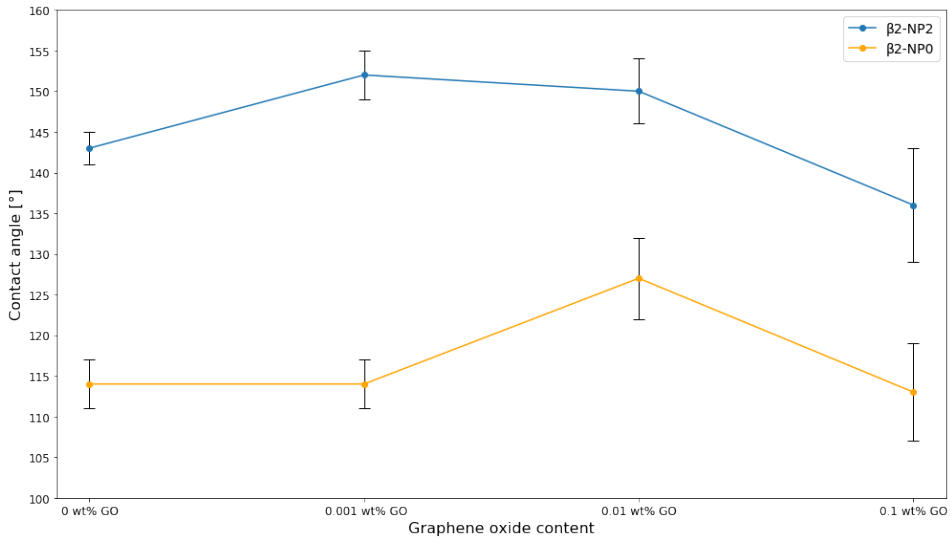


Figure 4.14: A comparison of contact angles with increasing graphene oxide content with and without NP2 particles.

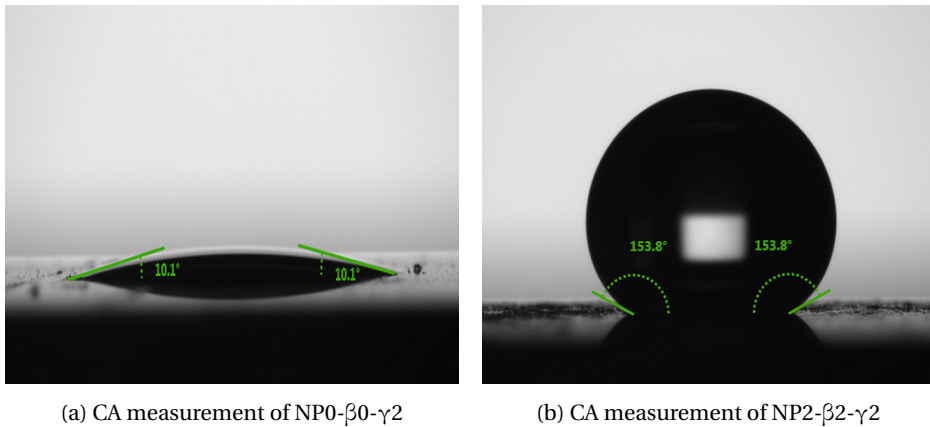


Figure 4.15: Contact angle comparison of NP0- $\beta 0$ - $\gamma 2$ and NP2- $\beta 2$ - $\gamma 2$ presented in Figure 4.15a and 4.15b respectively. A large difference in contact angles can be observed. In addition the remarkable contribution of nanoparticles and β -silane on the hydrophobicity can be seen.

Another important result is the ROA and CAH. For almost all measurements, the droplet remained pinned to the surface during tilting. As a result, a high liquid-surface adhesion is confirmed. Sample $\gamma 1\text{-}\beta 2\text{-NP2}$ and $\gamma 2\text{-}\beta 2\text{-NP2}$ was the only coatings who achieved a roll-of angle, wherein the roll-of angle varied significantly across the samples providing a high standard deviation. For the $\gamma 2\text{-}\beta 2\text{-NP2}$ samples, a very high ROA of $79^\circ \pm 7$ was recorded with relatively low CAH of $23^\circ \pm 9$. While $\gamma 1\text{-}\beta 2\text{-NP2}$ measurements showed a lower ROA of $46^\circ \pm 9$ coupled with a high CAH of $50^\circ \pm 17$. None of the coatings exhibited a CAH of less than 10° to qualify as superhydrophobic.

Contact angle measurements were performed at ambient temperatures. To ascertain the influence of evaporation on the contact angle and volume, a droplet was continuously measured as a function of time. This experiment yielded a constant evaporation rate affecting the CA over time, the result is plotted in Figure 4.16.

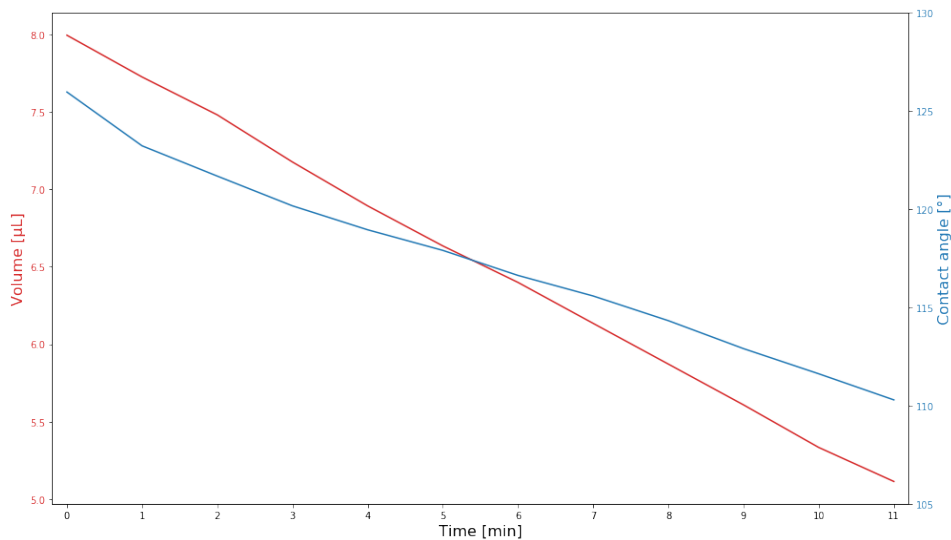


Figure 4.16: Contact angle and volume plotted against time. The measurements were taken of $8 \mu\text{L}$ droplet deposited on a $\gamma 1\text{-}\beta 2\text{-NP0}$ sample.

4.7 Anti-icing properties

4.7.1 Energy barrier

The temperature necessary to achieve ice nucleation was recorded and summarized in Table 4.5. Contact angles at 5°C, 0°C and individual nucleation temperatures are included to provide insight to the CA behaviour during declining temperatures. For all samples measured at 5°C, contact angles were below the superhydrophobic threshold of 150°. A decline in the hydrophobic behaviour at lower temperatures can be seen for all coating types. This decline is visualized in Figure 4.17 which compares the best performing coatings from each γ -category.

An increase in the energy barrier necessary for ice nucleation is observed for all coating compared to the γ_0 - β_0 -NP0 reference. From Figure 4.17 a trend of higher energy barriers with increasing graphene oxide content can be observed. Where the endpoint of the graphs indicate nucleation temperature. High contact angles were generally found to reflect high energy barriers. This effect can be seen by comparing γ_2 - β_2 -NP2 and γ_2 - β_2 -NP0.

Another phenomenon observed during ice nucleation experiments was the ice formation process. All droplets followed the same formation regime, although the speed varied. Figure 4.18 display a typical icing process. Formation began with a sudden change in color, this can be seen by comparing Figure 4.18a and 4.18b. Nucleation began at the liquid-surface interface followed by a unidirectional solidification. The red arrows in Figure 4.18 follow the ice solidification.

Table 4.5: Ice nucleation temperature measured for all samples. CA was also registered as the temperature decreased $1^\circ/\text{min}$.

Sample ID	Nucleation temperature	CA at 5°C	CA at 0°C	CA at nucleation temperature
$\gamma 0\text{-}\beta 0\text{-NP0}$	-5.6°C	62°	54°	53°
$\gamma 0\text{-}\beta 0\text{-NP1}$	-9.7°C	99°	97°	94°
$\gamma 0\text{-}\beta 0\text{-NP2}$	-10.4°C	73°	72°	71°
$\gamma 0\text{-}\beta 1\text{-NP0}$	-12.4°C	89°	88°	86°
$\gamma 0\text{-}\beta 1\text{-NP1}$	-15.3°C	100°	98°	93°
$\gamma 0\text{-}\beta 1\text{-NP2}$	-10.3°C	132°	130°	130°
$\gamma 1\text{-}\beta 2\text{-NP0}$	-13.1°C	107°	106°	105°
$\gamma 1\text{-}\beta 2\text{-NP2}$	-10.7°C	146°	143°	138°
$\gamma 2\text{-}\beta 2\text{-NP0}$	-7.3°C	91°	90°	87°
$\gamma 2\text{-}\beta 2\text{-NP2}$	-11.5°C	127°	123°	120°
$\gamma 3\text{-}\beta 1\text{-NP0}$	-11.1°C	110°	109°	105°
$\gamma 3\text{-}\beta 1\text{-NP1}$	-15.5°C	119°	117°	112°

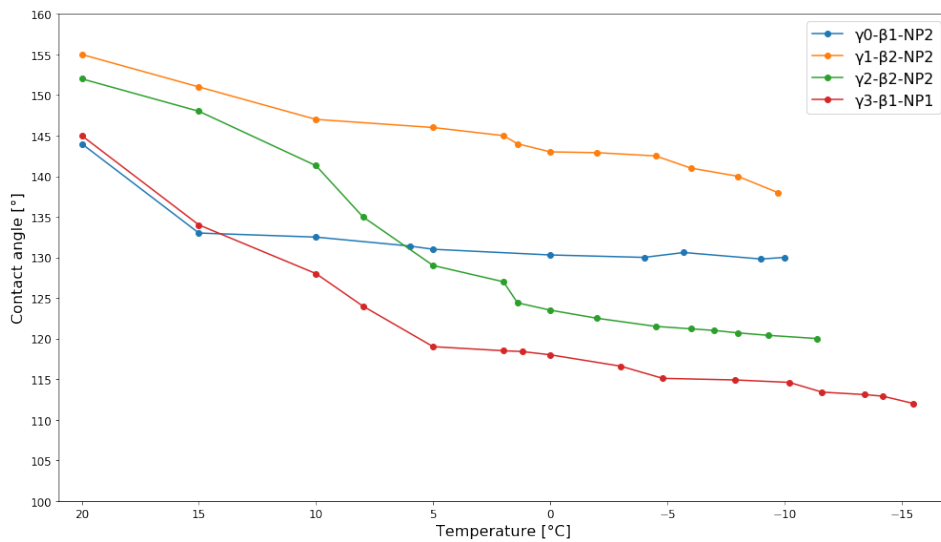


Figure 4.17: Contact angles recorded plotted against increasing graphene oxide content for both with and without nanoparticles.

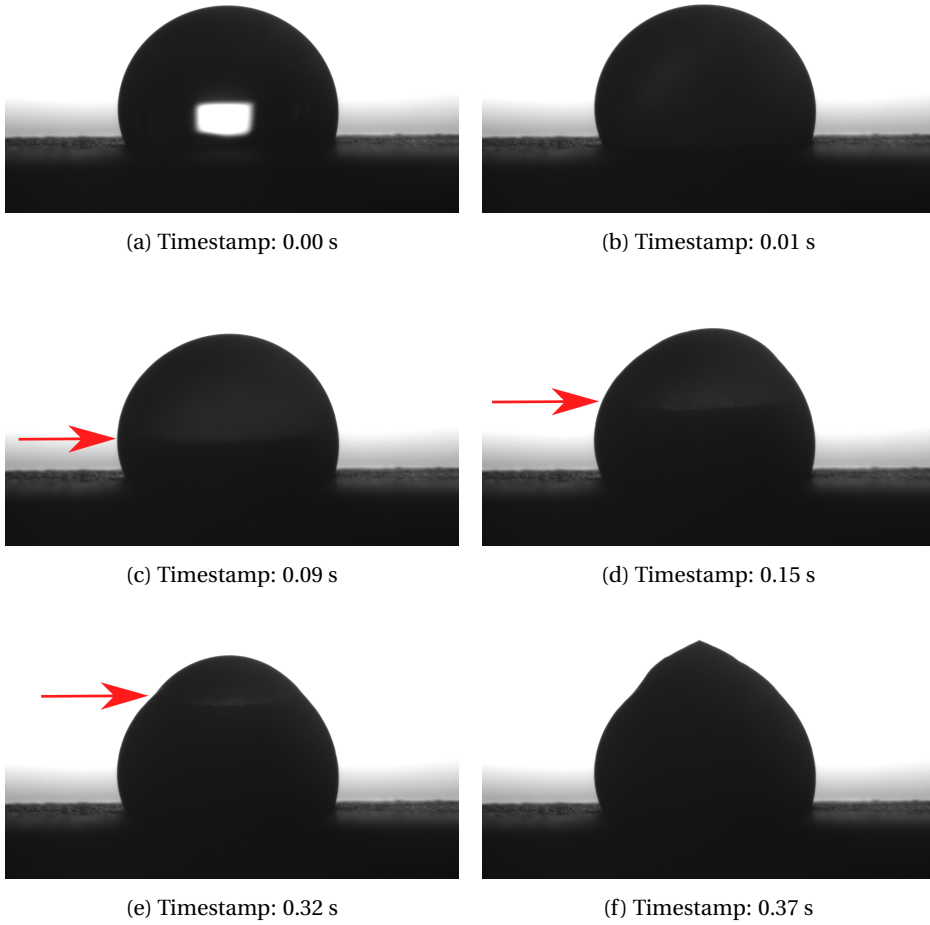


Figure 4.18: Ice formation on a γ_2 - β_2 -NP2 sample. Each image includes a timestamp indicating the speed and chronological order of the process. A volume increase can be observed from Image 4.18c through 4.18f.

4.7.2 Ice delay

Table 4.6 summarizes the delay of ice formation. As anticipated, γ 2- β 2-NP0 began freezing upon impact. The immediate nucleation was expected because of the energy barrier results, ceding ice nucleation at -7.3°C . The γ 0- β 2-NP2 coating yielded the highest nucleation delay of 23 minutes. While the addition of GO seemed to significantly reduce the ice delay.

Table 4.6: Results for the delay of ice nucleation. All samples were measured at $-10^{\circ}\text{C} \pm 0.2$. If the droplet froze upon impact, no contact angle was registered.

Sample ID	Ice formation delay	CA [$^{\circ}$]	Temperature ¹ [$^{\circ}\text{C}$]
γ 0- β 1-NP2	23 min	120	-10.0
γ 1- β 2-NP2	<1 min	122	-10.0
γ 2- β 2-NP0	0 min	N/A	-10.0
γ 2- β 2-NP2	8 min	117	-9.9
γ 3- β 1-NP1	<1 min	120	-10.1

4.7.3 Durability

Cyclic behaviour was investigated on the coatings of each γ -group showing the highest contact angle. Table 4.7 presents contact angle measured at 5°C and nucleation temperatures during cycling. All tested coatings demonstrated a good durability. Contact angles were reduced marginally during ice cycling.

Coating γ 0- β 2-NP2 and γ 3- β 2-NP2 showed minor contact angle deterioration and stable nucleation temperatures. γ 1- β 2-NP2 and γ 2- β 2-NP2 showed a large variation in nucleation temperatures. The recorded CA of γ 2- β 2-NP2 remained almost constant showing no signs of CA deterioration. γ 1- β 2-NP2 demonstrated the highest contact angles, but experienced a small CA reduction during cycling.

¹Exact temperature registered by the peltier element at ice nucleation.

Table 4.7: Contact angles were measured at 5°C before the temperature was gradually decreased 1°C/min. When the droplet froze, the temperature were recorded and the chamber was reheated to 5°C. Cycle 0 indicate the initial contact angle before any nucleation occurred.

Sample ID	Cycle	CA [°] at 5°C	Nucleation temperature [°C]
γ 0- β 1-NP2	0	133	-
	1	136	-10.0
	2	132	-10.3
	3	132	-10.8
γ 1- β 2-NP2	0	142	-
	1	141	-14.9
	2	138	-17.6
	3	136	-19.3
γ 2- β 2-NP2	0	127	-
	1	129	-9.4
	2	126	-15.2
	3	127	-14.4
γ 3- β 1-NP1	0	122	-
	1	116	-11.0
	2	116	-11.6
	3	116	-11.8

4.8 Tribological properties

$\gamma_2\text{-}\beta_2\text{-NP}_2$ and $\gamma_0\text{-}\beta_1\text{-NP}_2$ were characterized by SINTEF. By utilizing the 316-steel coefficient of friction, coating failure can be measured to compare abrasion resistance. 316-steel demonstrates a coefficient of friction of 1.04, which is therefore set as the threshold for coating failure. Coating failure is defined as complete removal of coating. Coefficient of friction as an evolution of time is presented in Figure 4.19. $\gamma_0\text{-}\beta_1\text{-NP}_2$ experienced coating failure after 4.1 seconds, while $\gamma_2\text{-}\beta_2\text{-NP}_2$ displayed coating failure after 22.7 seconds. By inspecting Figure 4.19, a significantly enhanced abrasion resistance can be observed for $\gamma_2\text{-}\beta_2\text{-NP}_2$.

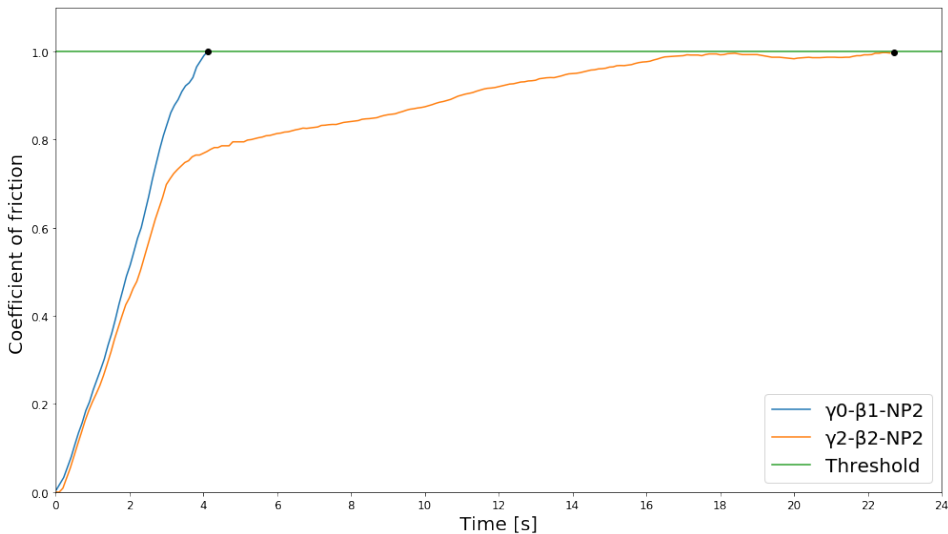


Figure 4.19: Coefficient of friction plotted against time. The black dots indicate coating failure.

Chapter 5

Discussion

5.1 Hierarchical structure

Hierarchical structures with a low microroughness and two different degrees of nanoroughness were constructed. Variations on the microroughness stem from the fabrication process while nanoroughness variation will be influenced by both the synthesis and deposition process.

5.1.1 Microroughness

The stainless steel surface is flattened during the cold-rolling process and will therefore yield a relatively smooth surface. As anticipated, a low average roughness was measured across the untreated surfaces. By inspecting Figure 4.1, narrow ridges and trenches along the substrate are observed. These ridges and trenches probably stem from deformation during manufacturing. Abrasive wear can influence the surface microstructure creating large random topography variations across the surface. Judging by the high kurtosis calculated for both measurement lengths, the bulk of the height measurements are well within the boundaries of the average roughness. Implying a very high accuracy of average roughness data. A negative skewness indicate a higher amount of crevices, these crevices are counterproductive when constructing a hierarchical structure. A crevice can

pin the water droplet if the crevice is wetted, establishing a high liquid-surface adhesion. Asperities are more beneficial when creating hierarchical structure. The average roughness increase from $R_a = 0.171 \mu\text{m}$ to $R_a = 0.239 \mu\text{m}$ between the different measurement lengths. An increase can be explained by small steel plate curvatures which arise during cold-rolling procedure. The effect of these curvatures can be further amplified when the steel plates are cut into substrate sizes. But due to the small scale difference the outcome of these curvatures can be neglected. Large amounts of mechanical deformations can be observed in Figure 4.2, these deformations have an insignificant impact on the surface roughness based on the average roughness coupled with a high kurtosis. Although these deformations might have a large impact on the local hierarchical structure inducing local variations.

5.1.2 Nanoparticles

Two different batches of nanoparticles were synthesized, only differing in reaction times to achieve different size distributions. The NP1 particles demonstrated a small mean particle size of 78 nm with a standard deviation of 8 nm offering a uniform particle distribution as seen in Figure 4.7. The NP2 batch was synthesized using parameters identical to the earlier work done by R.Luneng [1] who reported a mean size of 221 nm with a standard deviation of 8 nm. The NP2 mean size of 232 nm with a standard deviation of 32 nm verifies the reproducibility of the Stöber-Fink-Bohn process. The higher standard deviation for NP2 particles probably arise from a slightly lower pH. If the pH is not sufficiently high, the repulsive forces between particles will be weakened, resulting in particle growth.

Considering the nature of characterization, several uncertainties may have been introduced. Image J analyze each particle based on contrast and can be performed automatically or manually. At low magnification, the software may interpret overlapping particles as one large particle. And at very high magnifications, particle outlines may become blurred due to poor resolution. These phenomena introduce uncertainty of the mean particle size and standard deviation values. Both automatic and manual measurements were included in the mean size calculation in order to minimize this effect. Additional

images used for mean size calculation is included in Appendix B.

The proximity of nanoparticles across the surface have major influence on the hierarchical structure. From Figure 5.2 we can observe a thick and highly ordered layer of nanoparticles enclosed by a red trapeze. In this area the nanoparticles completely cover the microstructure, undermining the hierarchical structure. These highly ordered particle layers will behave as a nanostructured surface, reducing the roughness significantly. Figure 5.1 illustrate how the wetting properties can be altered by these ordered nanoparticle layers. As seen in Figure 5.1A, the nanostructure increase the surface area in contact with the water droplet. While Figure 5.1B illustrate how a scattered nanoparticle coverage can yield a lower liquid-surface interface resulting in a higher contact angle. Due to these nanoparticle buildups the hierarchical structure across the surface is compromised resulting in large variations. An optimized hierarchical structure demand a higher spreading of nanoparticles.

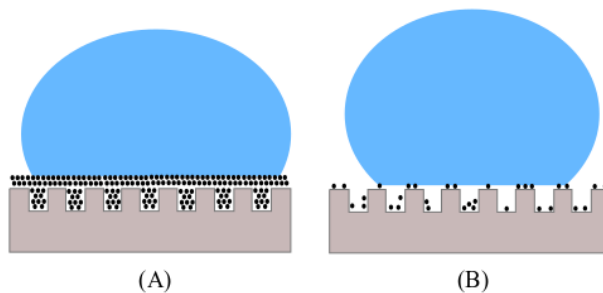


Figure 5.1: Illustration (A) demonstrate wetting behaviour on ordered nanoparticle layers. Illustration (B) demonstrates a scattered and random nanoparticle layer yielding a high contact angle.

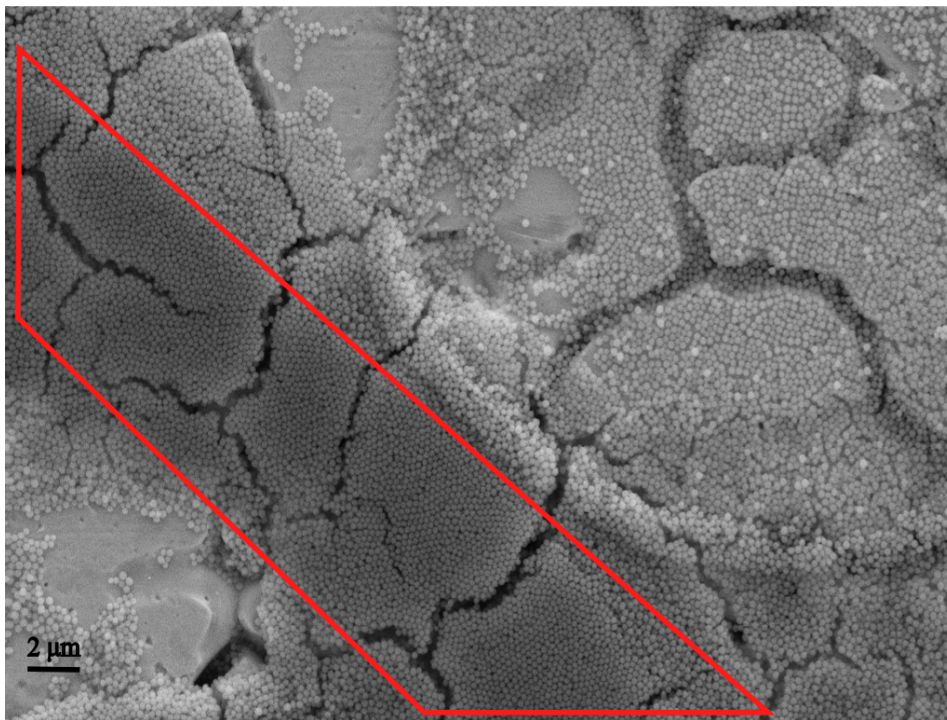


Figure 5.2: A nanoparticle buildup on a γ 0- β 0-NP2 sample showing a thick and highly ordered particle layer. The buildup is enclosed by a red trapeze.

For both nanoparticle sizes, clusters and nanoparticle buildups were observed. The nanoparticle buildups might be the result of poor spray deposition, but the nanoparticle clusters is likely to arise from poor silica adhesion to the surface. As seen in Figure 4.3 and 4.4, the large cluster consist of several small aggregated particles. An important inquiry followed by this observation is whether the clusters were formed before or after spray deposition. If the clusters are formed after deposition, a poor silica-surface adhesion can be assumed. But in this case, a higher amount of silica clusters would be expected across the surface. Only a couple of clusters were found during FESEM imaging. Therefore the cluster must be formed prior to deposition. The clusters are probably a result of an unstable particle solution causing aggregation over time, as visualized in Figure 2.8. There are several methods for resolving this issue. By enhancing the electrostatic and/or steric repulsion the solution will stabilize. By stabilizing the solution the attractive forces between silica nanoparticles will be decrease, minimizing cluster formation. A stabilizing effect on the particle solution might also reduce the nanoparticle buildups as shown in

Figure 4.6 and 5.2. Silica nanoparticle synthesis warrants further investigation on finding a suitable stabilizing agent. Another possible solution would be to sonicate the particle solution, a high sonication could be enough to break down the silica aggregates.

Based on Equation 2.9, the surface area of the nanoparticle shape will also have an influence on hydrophobicity. All synthesized nanoparticles are homogeneous and spherical, where spheres show a relative large surface area. Based on the assumption of minimal liquid-surface contact area result in maximum contact angles. Spherical nanoparticles are sub-optimal compared to nanowires or nanoprisms. The importance of nanostructure shape should be researched and taken into account when evaluating hydrophobicity.

5.2 Synthesis evaluation

A toilsome challenge was keeping the temperature constant during particle and coating synthesis. As a result several batches of nanoparticles failed to be used in further experiments. The dry block heater was unable to keep a constant temperature and the temperature fluctuated heavily. To minimize this problem, a water bath was introduced. The water bath prevented the sudden temperature changes and kept the temperature more stable.

pH was not continuously measured during the synthesis. Based on the pH dependence of the morphology, a source of uncertainty is introduced. If the pH was altered by inaccurate ammonium hydroxide administration, the hydrolysis and condensation rates could have been affected, resulting in undesirable morphologies. Figure 2.7 demonstrates how change in pH can affect the structure of silica nanoparticles. NP2 particles show a larger size distribution which could have been the outcome of unstable pH during synthesis.

5.3 Wetting states

Microroughness primarily govern the CAH whereas the nanoroughness heavily influence the CA [40]. Considering the high CAH achieved for γ_1 - β_2 -NP2 and γ_2 - γ_2 -NP2, a Cassie impregnating state is most likely to have existed during measurements. A high CA coupled with a high CAH is called a rose petal effect, and is unfavourable for anti-icing coatings. This is due to the high water-surface adhesion preventing water droplets from shedding. Such behaviour might arise from nanoparticle buildups covering and subverting the hierarchical structure, or the hierarchical microroughness being too low. By increasing the average roughness through sandblasting, a higher microroughness can be achieved. By increasing the microroughness a more ideal hierarchical structure can be created, favouring a Cassie-Baxter state. Consequently increasing the water repellent behaviour. This possibility is demonstrated by earlier work by R.Luneng and H.Vassmyr [1, 2]. γ_0 - β_1 -NP2 and γ_3 - β_1 -NP1 demonstrated contact angles below 150° and ROA $> 90^\circ$, these results indicate a Wenzel wetting state. Or a combination of Cassie impregnating and Wenzel state.

The reason for assuming a Cassie impregnating state instead of a Wenzel state for coating γ_1 - β_2 -NP2 and γ_2 - γ_2 -NP2 is because of the high CA recorded. A Wenzel state will effectively lower the contact angle due to increased wetting, as indicated in Figure 2.3. The high adhesion arise from the water droplet being pinned by the partially wetted hierarchical structure. Figure 5.3 serves as an example of how the surface structure can pin the droplet, causing high adhesion.

Both particle sizes demonstrates a uniform shape and size which can be observed in Figure 4.5. NP2 particles were found to have, on average, a higher impact on the contact angle compared to the NP1 particles. Although the differences are minor, these findings are contradictory to the work performed by Hill et al. [72]. These contradicting results might stem from inaccuracies during characterization or a non-uniform coating.

By inspecting Figure 4.17 a decrease in contact angle can be observed as temperature was lowered. This decrease probably arise due to a irreversible transition from a Cassie-Baxter/Cassie impregnating state to a wetted Wenzel state. Once the air pockets in a

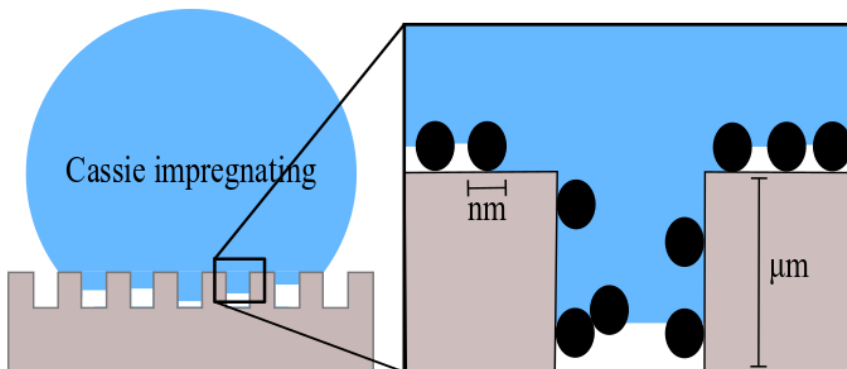


Figure 5.3: Magnified illustration of the Cassie impregnating state. Partial penetration of the hierarchical structure resulting in a pinned water droplet. The black circles indicate silica nanoparticles.

Cassie-Baxter state is removed/wetted, cohesive forces will prevent air pockets from occurring during reheating of the samples. A more favourable equilibria is established, this behaviour can be seen in coating γ_3 - γ_2 -NP1 and γ_0 - γ_1 -NP2 in Table 4.7.

5.4 Spray coating and rheology

Alternative deposition techniques were considered, such as dip coating and spin coating. Spin coating is a promising deposition technique based on the uniform layer produced and reproducibility. Because spin coating is not feasible for industrial scaling, spin coating was considered sub-optimal. Dip coating was dismissed as an alternative because of earlier work performed by the author [3]. Previous findings determined dip coating insufficient for achieving a uniform layer. Dip coating was also found to be heavily influenced by the microstructure, showing a very high coating densities in crevices while protruding peaks were uncoated.

The reported viscosities for the β_1 and β_2 solutions were similar and had consequently little effect on the deposition variation. Similar viscosities is due to the high percentage of absolute ethanol in the sol, which has a reported viscosity of 0.949 mPas [73]. Although

the nanoparticle solutions had a higher measured viscosity, the difference is considered minor thus the influence is deemed to be insignificant.

A large uncertainty can be attributed to the nature of spray coating. Considering all spray depositions were performed by hand, significant coating and nanoparticle variations can be expected. This expectation is validated when inspecting Figure 4.6, areas with significantly higher amounts of nanoparticles can be spotted forming what appears to be outer rim of a circle. Where the epicenter is less populated with nanoparticles. This formation most likely stem from the spray gun being held too close to the substrate or the pressure being too high during deposition. This warrants further optimization of the spray coating procedure. Albeit spray coating proved a suitable technique for obtaining a high coverage which was reported for all coatings investigated.

5.5 Coating thickness and coverage

The coating thickness was measured by scratching the coating manually with a copper nail and subsequently measuring the depth of the cut. Since the force applied when scratching the coating is not quantified, this result only serves as a rudimentary approximation. This is reflected from the high standard deviation of $0.37\ \mu\text{m}$. In addition, the test does not account for whether or not all of the coating was removed during scratching. Several thickness measurements were performed to minimize uncertainty. All thickness measurements were averaged to approximate the coating thickness. A more reliable measurement technique would be to image the cross-section of the sample allowing precise thickness measurements. But due to the thin nature of the coating this technique might prove problematic. Machining the substrate might completely remove the thin coating rendering the test unsuccessful.

Coating thickness is an important parameter regarding the hierarchical structure. To preserve the hierarchical structure, the coating cannot be too thick. A thick coating will undermine the hierarchical structure. Based on the coatings containing nanoparticles systematically demonstrated higher hydrophobicity than their counterpart, the average coating thickness of $2.05 \pm 0.37\ \mu\text{m}$ is considered adequate. A compromise is made when

creating thin coatings/composites. Coleman et.al suggest a proportional relationship between composite strength and composite thickness [74]. Indicating an optimization of coating strength by maximizing the coating thickness. Finding the threshold for maximum coating thickness is therefore warranted.

The pre-cut measurement of $\gamma_0\text{-}\beta_1\text{-NP0}$ on Figure 4.9 is considered representative for the coating thickness uniformity. All profilometer measurements showed similar topography behaviour as Figure 4.9, the small crevices is assumed to be a result of the underlying microstructure. Coating thickness is estimated to be within boundaries of 2.05 ± 0.37 μm and evenly distributed across the sample indicating a high coating coverage. This estimation is supported by the high CA measurements coupled with a low standard deviation. If parts of the coating were uncoated, the measured CA would be drastically lower causing large standard deviations. Because all coatings follow an identical spray coating regime, the assumption of similar coating thickness for all coatings deposited is valid.

Energy-dispersive X-ray spectroscopy, EDS, measurements were attempted on the coatings to verify a successful coating deposition. Results proved inadequate and were therefore not included in the result section. The thin nature of the coating made EDS measurements challenging. Fluorine was targeted as the coating identifier because silicon, oxygen and carbon are present in the 316-steel substrate as seen in Table 3.1. But the interaction volume of the incident beam proved too large even at minimum voltages. All measurements were dominated by the 316-steel. In addition, the characteristic x-rays of fluorine and iron overlaps. The K_α energy for fluorine and L_α energy of iron are almost identical, tabulated at 0.677 keV and 0.705 keV respectively [75]. These similar x-ray energies are difficult to distinguish from each other, making EDS measurements futile.

5.6 Contact angle evaluation

Extensive contact angle measurements were performed during the experimental work and contact angle variations were found on all tested samples. These variations either arise from characterization errors or coating deficiencies such as nanoparticle buildups. The standard deviations measured are quite low for all tested samples, suggesting a high CA accuracy.

A type of characterization error is the fitting mode. The selection of fitting mode will inherently introduce a source of error. Because the accuracy of the fitting mode is limited by the resolution of the high speed camera. Poor resolution will result in inaccurate measurements due to blurred droplet boundaries. To minimize this source of error, the optimal fitting mode was selected based on the predicted droplet behaviour. For static contact angles, the droplet usually forms a symmetrical shape which is best reflected by the Young-Laplace fitting mode [71]. While the Tangent mode was used for curve-fitting the dynamic contact angles. The dynamic contact angles are highly irregular and may induce large errors due to disturbance in the drop shape caused by contaminants or surface irregularities [71]. Proposing a higher possible error in the dynamic contact angle measurements such as ROA and CAH.

According to Young's equation 2.4, the static contact angle is not dependant on the droplet size. However, it is intuitive that gravity will affect the droplet shape with increasing volume. Extrand and Moon [76] found that droplets below 10 μL displayed a spherical shape and was unaffected by the gravitational pull. Considering the consistent use of 8 μL droplets during all contact angle measurements and icing experiments, the gravitational effect on the contact angle can be neglected.

Atmosphere is also an important factor, all contact angles presented in Table 4.4 were conducted at ambient temperatures. Consequently evaporation and its effect on the droplet shape must be evaluated. To examine the evaporation, the droplet volume was measured as a function of time. As shown in Figure 4.16, the evaporation is too slow to affect static the droplet shape considering the automated program was finished within 10 seconds. Although the dynamic contact angles were measured over a 100 second

period, indicating atmospheric influence on the dynamic contact angles. Suggesting a higher uncertainty for ROA and CAH measurements. To control the evaporation rate or in case of long term contact angle evaluation. A humidity chamber should be employed in combination with the DSA 100.

Another characterization challenge faced was the baseline error. The ADVANCE software from Kruss automatically pinpoint the baseline of the substrate. But due to inconsistent baselines, the baseline had to be set manually for every measurement. Figure 5.4 demonstrates how the baseline had to be set between every measurement. This method will naturally introduce some uncertainties. If the baseline was offset by even the smallest margin, a source of error is introduced to the measurement.

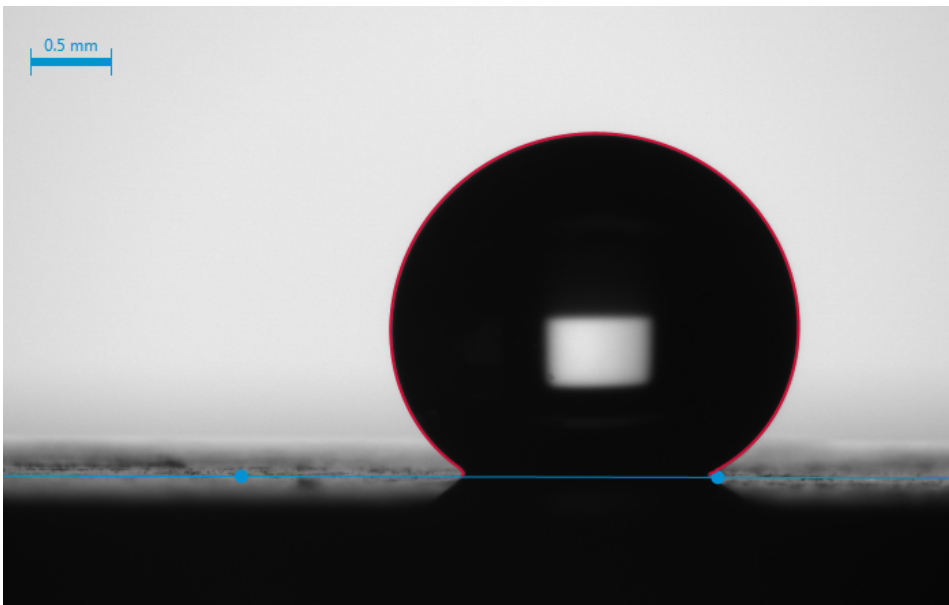


Figure 5.4: An example on how the baseline was manually set between each contact angle measurement. The baseline is represented by a blue line. The image is taken of a γ 3- β 1-NP1 sample.

5.7 Anti-icing characterization

During icing experiments only one sample from each coating type was tested. This was done because of time constraints and will naturally introduce a large uncertainty

to the reproducibility of icing experiments. A large discrepancy can be observed in some coatings when comparing the ice nucleation temperature between energy barrier tests and cycling tests. The largest difference being 8.6°C recorded for the $\gamma 1$ - $\beta 2$ -NP2 sample. A statistical approach is necessary to reduce the uncertainty and achieve a true representation of the icing behaviour.

During ice formation delay, the beneficial effect of nanoparticles can be observed in Table 4.6. The coating without nanoparticles froze upon impact, giving credit to the theory of insulating air pockets created by hierarchical structures delays ice formation [13].

The instrument used to perform anti-icing experiments, DSA 100, was not placed on vibration dampening pads. This error could have influenced the nucleation experiments. Causing ice formation to occur prematurely due to external vibrations. This error might be the reason for $\gamma 1$ - $\beta 2$ -NP2 decrease in nucleation temperature. Suggesting a very low true nucleation temperature.

Ice formation will eventually occur on all anti-icing coatings regardless of icephobicity. Because of this, the ice adhesion strength of the coating should be considered. Ice adhesion test were not performed during this work, but because of Equation 2.14 some predictions can be made [50]. Coating $\gamma 1$ - $\beta 2$ -NP2 and $\gamma 2$ - $\beta 2$ -NP2 demonstrated the lowest liquid-surface adhesion with a receding contact angle of $112^\circ \pm 14^\circ$ and $137^\circ \pm 3^\circ$ respectively. From these results a new approximation can be calculated in Equation 5.1 and 5.2. From Equation 5.1 and 5.2 a large difference can be seen, suggesting a significantly lower work of ice adhesion for $\gamma 2$ - $\beta 2$ -NP2.

$$W_{\gamma 1-\beta 2-NP2} \approx \gamma_w (1 + \cos 112) = 0.63\gamma_w \quad (5.1)$$

$$W_{\gamma 2-\beta 2-NP2} \approx \gamma_w (1 + \cos 137) = 0.29\gamma_w \quad (5.2)$$

5.8 Tribological assessment

Assuming equal coating thickness a significantly higher abrasion resistance can be seen for $\gamma 2\text{-}\beta 2\text{-NP2}$ compared to the reference $\gamma 0\text{-}\beta 2\text{-NP2}$. Although the assumption of similar coating thickness can be made as explained in Section 5.5, a source of error is introduced. Reproducible results are required to verify the contributing effect of graphene oxide. In addition, the tribological experiment does not give any information about the impact of graphene oxide content. To assess the optimal graphene oxide content, several coatings with different graphene oxide quantities should be measured.

The applied load of 1 N is low compared to industrial standards. Industrial grade polymer coatings with similar thickness usually range between 2-40 N [77]. Considering the short coating lifetime under 1 N applied force, a poor abrasion resistance can be established for both coatings compared to industrial standards.

5.9 Graphene oxides effect on anti-icing coatings

Despite graphene oxides hydrophilic nature, a superhydrophobic contact angle is obtainable through rigorous experiments. Graphene oxide is insoluble in most solutions except water [57], however by introducing the graphene oxide via the water acting as a hydrolyzing agent, graphene oxide can be successfully incorporated into the coating. Graphene oxide does not seem to reduce the hydrophobic character of the coating, based on Table 4.4, but rather enhance the hydrophobic character at ambient temperatures. Although a drastic hydrophobic deterioration can be seen in Figure 4.14 for coatings containing graphene oxide. These results show great potential for graphene oxide additions in hydrophobic coatings.

The additions of graphene oxide into the coating seemed to have a minor effect on the cycling durability and nucleation temperature. Compared to the reference coating, $\gamma 0\text{-}\beta 1\text{-NP2}$, improved nucleation temperatures can be seen in Table 4.7. The change in contact angle at 5°C also seem unaffected by the graphene oxide additions. All tested coatings almost retain its original contact angle, $\pm 6^\circ$, after three cycles regardless of

graphene oxide amount. Ice formation delay was notably reduced for all coatings containing graphene oxide. The amount of graphene oxide seems insignificant considering both $\gamma 1\text{-}\beta 2\text{-NP2}$ and $\gamma 3\text{-}\beta 1\text{-NP1}$ froze within one minute of deposition. The best performing coating containing graphene oxide was the $\gamma 2\text{-}\beta 2\text{-NP2}$ with a 8 minute delay. This result show a clear decay in ice formation delay, compared to the $\gamma 0\text{-}\beta 1\text{-NP2}$ coating with a delay time of 23 minutes. Based on these findings we can postulate that the degree graphene oxide content have minor effect on the durability, an improved effect on energy barrier for ice formation and a deteriorating effect on ice formation delay. Considering the icing characterization were only performed once, these findings only show a preliminary result. Statistical anti-icing test must be performed before making a definite conclusion.

Sheets of graphene oxide can clearly be observed in Figure 4.10. But without knowing the size of the graphene oxide sheets used in the synthesis, it is difficult to discern whether the sheets observed is one singular sheet or several inter-layered sheets. Further analysis on the GO used should be performed, regarding the mechanical properties and composition. The placement of the sheets is also a challenging aspect. GO will contribute most significantly if the sheets are embedded into the polymer matrix. Where it can act as a 2-dimensional nanofiller [15, 17]. Due to the extremely thin polymer coating, it is difficult to determine whether the graphene oxide sheets are on the surface or inside the polymer coating. If the sheets are situated on the surface of the polymer, they will most likely increase wetting, undermining the hydrophobic behaviour.

Chapter 6

Conclusion

A hierarchical structure was created by combining the inherent microroughness from cold-rolled 316-steel with the nanoroughness supplied by SiO₂ nanoparticles. The superhydrophobic behaviour of the coating were found to be dependant on both surface structure and surface chemistry. Nanoparticles played a key factor in increasing the hydrophobicity, all coatings containing nanoparticles exhibited high contact angles. The inherent microroughness of cold-rolled 316-substrates were found to be too low to yield an ideal hierarchical structure. An increased microroughness is suspected to generate an improved contact angle hysteresis. Nanoparticles were also shown to increase the ice formation delay. All nanoparticles exhibited a uniform shape and size verifying the reproducibility of the Stöber-Fink-Bohn method. 232nm particles were shown to have a higher influence on the hydrophobicity than the 78 nm particles, although the difference were minor. Spray coating proved feasible for nanoparticle and coating deposition, although large variations were found and further optimization is warranted. Nanoparticles synthesized showed a high particle-particle attraction contributing to an uneven nanoparticle distribution. A high liquid-surface adhesion was measured for all coatings. Indicating a Cassie impregnating state, or a so-called rose petal effect. None of the synthesized coatings demonstrated a superhydrophobic behaviour, due to high contact angle hysteresis. A decreasing contact angle trend was observed for increasing graphene oxide content. The best performing coating was γ 2- β 2-NP2 displaying a

contact angle of $150^{\circ} \pm 4^{\circ}$ and a contact angle hysteresis of 23 ± 9 . Suggesting 0.01wt% graphene oxide is the most viable option for superhydrophobic anti-icing coatings. Anti-icing experiments showed a significant decrease in ice formation delay due to graphene oxide additions. The quantity of graphene oxide added seemed inconsequential to the ice delay. Contact angles were also found to decrease as temperature was lowered. This decrease is believed to arise due to an irreversible transition from a Cassie-Baxter/Cassie impregnating state to a wetted Wenzel state. During cycling tests graphene oxide showed a contributing effect on the durability of the examined coatings. γ 2- β 2-NP2 showed no change in contact angles during subsequent cycling. Graphene oxide showed a minor beneficial effect on anti-icing properties, this effect is believed to be amplified by improving the superhydrophobic character of the coating. Tribological measurements showed a significantly enhanced abrasion resistance on the anti-icing coatings due to graphene oxide additions.

Deviations were found during icing experiments and due to lack of statistical icing measurements, these deviations introduce a large uncertainty. The deviations found can be explained by a non-uniformity in the coating which most likely derives from uneven nanoparticle distribution and mechanical deformation. Many sources of error exist because of a complex and multilayered system. An evenly distributed particle distribution combined with a higher microroughness could achieve a more favourable Cassie-Baxter state. Further experiments are necessary to conclude graphene oxide viability in anti-icing coatings. 0.01wt% graphene oxide additions show the highest potential for anti-icing application.

Chapter 7

Further work

The anti-icing coatings in this work are multilayered and complex nanocomposites. Several critical factors are involved when designing the nanocomposite. Each of these factors must be optimized to yield a high performance anti-icing coating. Surface structure were found to be sub-optimal, warranting further surface modification such as sandblasting or polishing to alter microroughness. Increasing microroughness via sandblasting shows a promising potential for improving the hydrophobicity [1, 2]. Thick nanoparticle buildups were responsible a non-uniform particle distribution, this is partially due to attractive intermolecular forces between particles. Further synthesis optimization should be made to decrease the intermolecular forces to achieve a stable nanoparticle solution. Sonication of the particle solution prior to deposition is also believed to reduce the amount of nanoparticle clusters. The uneven particle deposition can also be attributed to the spray coating method. To improve the deposition and reduce variations a standardized and automated deposition method is recommended.

The surface chemistry of the fluorine based polymer proved satisfactory and graphene oxide was successfully incorporated into the polymer matrix, although further functionalization can be done to improve adhesion and reproducibility. Graphene oxide has a high capacity for chemical functionalization opening a plethora of alternative methods for incorporating graphene oxide into the polymer matrix [55]. 1H,1H,2H,2H-Perfluorooctyltriethoxysilane is an expensive precursor material, thus an alternative and

cheaper polymer should be investigated for potential industrial application.

Graphene oxides potential as a nanofiller were not investigated during this work. Further work should research and emphasize the mechanical strength graphene oxide can offer as a reinforcing agent [15, 16]. This research in combination with a statistical approach to icing properties should be sufficient to establish graphene oxides potential in anti-icing coatings. Maximum coating thickness should also be investigated to optimize composite strength while retaining the hierarchical structure. Ice adhesion is an important anti-icing property and should also be included in further anti-icing investigation.

Bibliography

- [1] Raymond Luneng. Development of hydrophobic surfaces for anti-icing applications. Master's thesis, 2015.
- [2] Hanna Sandvoll Vassmyr. Development of hydrophobic surfaces for anti-icing applications. Master's thesis, 2016.
- [3] Erik Wangensten Berg. Anti-icing coatings; preparation and characterization. Specialization Project, 2018.
- [4] J.L. Laforte, M.A. Allaire, and J. Laflamme. State-of-the-art on power line de-icing. *Atmospheric Research*, 46(1):143 – 158, 1998.
- [5] Ali Raza Solangi. Icing effects on power lines and anti-icing and de-icing methods. Master's thesis, UiT The Arctic University of Norway, 2018.
- [6] S Barber, Y Wang, S Jafari, N Chokani, and Reza S Abhari. The impact of ice formation on wind turbine performance and aerodynamics. *Journal of Solar Energy Engineering*, 133(1):011007, 2011.
- [7] Ozcan Yirtici, Ismail H Tuncer, and Serkan Ozgen. Ice accretion prediction on wind turbines and consequent power losses. In *Journal of Physics: Conference Series*, volume 753, page 022022. IOP Publishing, 2016.
- [8] G Brasseur, RA Cox, D Hauglustaine, et al. Aircraft icing. *National Center for Atmospheric Research*, 2003.
- [9] D. Wright J. Steuernagle, K. Roy. Aircraft icing. *Aircraft Owners and Pilots Association*, page 16, 2008.

- [10] Tuo Wang, Yonghao Zheng, Abdul-Rahman O. Raji, Yilun Li, William K. A. Sikkema, and James M. Tour. Passive anti-icing and active deicing films. *ACS Applied Materials & Interfaces*, 8(22):14169–14173, 2016.
- [11] Roman Zorn and Hagen Steger. De-icing and snow melting system with innovative heat pipe technology. 2015.
- [12] H.L. Dai, K.L. Zhang, X.L. Xu, and H.Y. Yu. Evaluation on the effects of deicing chemicals on soil and water environment. *Procedia Environmental Sciences*, 13, 2012. 18th Biennial ISEM Conference on Ecological Modelling for Global Change and Coupled Human and Natural System.
- [13] Michael J Kreder, Jack Alvarenga, Philseok Kim, and Joanna Aizenberg. Design of anti-icing surfaces: smooth, textured or slippery? *Nature Reviews Materials*, 1(1), 2016.
- [14] Ji Won Suk, Richard D. Piner, Jinho An, and Rodney S. Ruoff. Mechanical properties of monolayer graphene oxide. *ACS Nano*, 4(11):6557–6564, 2010.
- [15] E.I. Akpan, X. Shen, B. Wetzel, and K. Friedrich. 2 - design and synthesis of polymer nanocomposites. In Krzysztof Pielichowski and Tomasz M. Majka, editors, *Polymer Composites with Functionalized Nanoparticles*, Micro and Nano Technologies, pages 47 – 83. Elsevier, 2019.
- [16] J. Njuguna, K. Pielichowski, and S. Desai. Nanofiller-reinforced polymer nanocomposites. *Polymers for Advanced Technologies*, 19(8):947–959, 2008.
- [17] Kirk M. Cantor and Patrick Watts. 12 - plastics processing. In Myer Kutz, editor, *Applied Plastics Engineering Handbook*, Plastics Design Library, pages 195 – 203. William Andrew Publishing, Oxford, 2011.
- [18] Paul C Hiemenz. Principles of colloid and surface chemistry, 1997.
- [19] Rice University. Water, 2012.
- [20] N. Gao, Y.Y. Yan, X.Y. Chen, and D.J. Mee. Superhydrophobic surfaces with hierarchical structure. *Materials Letters*, 65(19):2902 – 2905, 2011.

- [21] Finn Knut Hansen. The measurement of surface energy of polymers by means of contact angles of liquids on solid surfaces. *A short overview of frequently used methods*. University of Oslo, Oslo, 2004.
- [22] Robert J Good. Surface free energy of solids and liquids: thermodynamics, molecular forces, and structure. *Journal of colloid and interface science*, 59(3):398–419, 1977.
- [23] F Leroy and F Muller-Plathe. Calculation of the work of adhesion of solid-liquid interfaces by molecular dynamics simulations. In *Schriften des Forschungszentrums Julich, NIC Series*, volume 48, 2016.
- [24] Saleem Hashmi. *Comprehensive materials finishing*. Elsevier, 2016.
- [25] Bharat Bhushan, Yong Chae Jung, and Kerstin Koch. Micro-, nano- and hierarchical structures for superhydrophobicity, self-cleaning and low adhesion. *Philosophical Transactions of the Royal Society of London A: Mathematical, Physical and Engineering Sciences*, 367(1894):1631–1672, 2009.
- [26] Ludmila B. Boinovich and Alexandre M. Emelyanenko. Anti-icing potential of superhydrophobic coatings. *Mendeleev Communications*, 23(1):3 – 10, 2013.
- [27] Yuehua Yuan and T Randall Lee. Contact angle and wetting properties. In *Surface science techniques*, pages 3–34. Springer, 2013.
- [28] Adam J. Meuler, J. David Smith, Kripa K. Varanasi, Joseph M. Mabry, Gareth H. McKinley, and Robert E. Cohen. Relationships between water wettability and ice adhesion. *ACS Applied Materials & Interfaces*, 2(11):3100–3110, 2010.
- [29] Richard Menini and Masoud Farzaneh. Advanced icephobic coatings. *Journal of Adhesion Science and Technology*, 25(9):971–992, 2011.
- [30] Lichao Gao and Thomas J McCarthy. Contact angle hysteresis explained. *Langmuir*, 22(14):6234–6237, 2006.
- [31] Masashi Miwa, Akira Nakajima, Akira Fujishima, Kazuhito Hashimoto, and Toshiya Watanabe. Effects of the surface roughness on sliding angles of water droplets on superhydrophobic surfaces. *Langmuir*, 16(13):5754–5760, 2000.

- [32] Biolin Scientific. *Contact angle measurements*, 2018.
- [33] HB Eral, JM Oh, et al. Contact angle hysteresis: a review of fundamentals and applications. *Colloid and polymer science*, 291(2):247–260, 2013.
- [34] Abraham Marmur. The lotus effect: Superhydrophobicity and metastability. *Langmuir*, 20(9):3517–3519, 2004.
- [35] Robert N. Wenzel. Resistance of solid surfaces to wetting by water. *Industrial & Engineering Chemistry*, 28(8):988–994, 1936.
- [36] Alberto Giacomello, Simone Meloni, Mauro Chinappi, and Carlo Massimo Casciola. Cassie–baxter and wenzel states on a nanostructured surface: Phase diagram, metastabilities, and transition mechanism by atomistic free energy calculations. *Langmuir*, 28(29):10764–10772, 2012.
- [37] ABD Cassie and S Baxter. Wettability of porous surfaces. *Transactions of the Faraday society*, 40:546–551, 1944.
- [38] Sanjay Subhash Latthe, Annaso Basavraj Gurav, Chavan Shridhar Maruti, and Rajiv Shrikant Vhatkar. Recent progress in preparation of superhydrophobic surfaces: a review. *Journal of Surface Engineered Materials and Advanced Technology*, 2(02):76, 2012.
- [39] Gene Whyman, Edward Bormashenko, and Tamir Stein. The rigorous derivation of young, cassie–baxter and wenzel equations and the analysis of the contact angle hysteresis phenomenon. *Chemical Physics Letters*, 450(4):355 – 359, 2008.
- [40] Bharat Bhushan and Michael Nosonovsky. The rose petal effect and the modes of superhydrophobicity. *Philosophical Transactions of the Royal Society A: Mathematical, Physical and Engineering Sciences*, 368(1929):4713–4728, 2010.
- [41] ES Gadelmawla, M.M. Koura, Talal Maksoud, Ibrahim Elewa, and Hassan Soliman. Roughness parameters. *Journal of Materials Processing Technology*, 123:133–145, 04 2002.

- [42] Kristian Sætre. Ice abrasion on fiber reinforced concrete: A study on the effects of various types of fiber and the reliability of the laboratory measurements. Master's thesis, Institutt for konstruksjonsteknikk, 2014.
- [43] Bharat Bhushan. Surface roughness analysis and measurement techniques. In *Modern Tribology Handbook, Two Volume Set*, pages 74–144. CRC press, 2000.
- [44] C Neinhuis and W Barthlott. Characterization and distribution of water-repellent, self-cleaning plant surfaces. *Annals of botany*, 79(6):667–677, 1997.
- [45] Abraham Marmur. The lotus effect: Superhydrophobicity and metastability. *Langmuir*, 20(9):3517–3519, 2004.
- [46] S Farhadi, M Farzaneh, and SA Kulinich. Anti-icing performance of superhydrophobic surfaces. *Applied Surface Science*, 257(14):6264–6269, 2011.
- [47] Philseok Kim, Tak-Sing Wong, Jack Alvarenga, Michael J. Kreder, Wilmer E. Adorno-Martinez, and Joanna Aizenberg. Liquid-infused nanostructured surfaces with extreme anti-ice and anti-frost performance. *ACS Nano*, 6(8):6569–6577, 2012.
- [48] Vahid Hejazi, Konstantin Sobolev, and Michael Nosonovsky. From superhydrophobicity to icephobicity: forces and interaction analysis. *Scientific reports*, 3:2194, 2013.
- [49] Atanu K. Metya, Jayant K. Singh, and Florian Müller-Plathe. Ice nucleation on nanotextured surfaces: the influence of surface fraction, pillar height and wetting states. *Phys. Chem. Chem. Phys.*, 18:26796–26806, 2016.
- [50] Lasse Makkonen. Ice adhesion —theory, measurements and countermeasures. *Journal of Adhesion Science and Technology*, 26(4-5):413–445, 2012.
- [51] Richard Menini, Zahira Ghalmi, and Masoud Farzaneh. Highly resistant icephobic coatings on aluminum alloys. *Cold Regions Science and Technology*, 65(1):65–69, 2011.
- [52] Liangliang Cao, Andrew K. Jones, Vinod K. Sikka, Jianzhong Wu, and Di Gao. Anti-icing superhydrophobic coatings. *Langmuir*, 25(21), 2009.

- [53] SA Kulinich and M Farzaneh. Ice adhesion on super-hydrophobic surfaces. *Applied Surface Science*, 255(18):8153–8157, 2009.
- [54] K. S. Novoselov, A. K. Geim, S. V. Morozov, D. Jiang, Y. Zhang, S. V. Dubonos, I. V. Grigorieva, and A. A. Firsov. Electric field effect in atomically thin carbon films. *Science*, 306(5696):666–669, 2004.
- [55] Da Chen, Hongbin Feng, and Jinghong Li. Graphene oxide: Preparation, functionalization, and electrochemical applications. *Chemical Reviews*, 112(11):6027–6053, 2012.
- [56] Konstantin S Novoselov, VI Fal, L Colombo, PR Gellert, MG Schwab, K Kim, et al. A roadmap for graphene. *nature*, 490(7419):192, 2012.
- [57] Vadim V Neklyudov, Nail R Khafizov, Igor A Sedov, and Ayrat M Dimiev. New insights into the solubility of graphene oxide in water and alcohols. *Physical Chemistry Chemical Physics*, 19(26):17000–17008, 2017.
- [58] F.V. Ferreira, E.S. Brito, W. Franceschi, E.A.N. Simonetti, L.S. Cividanes, M. Chipara, and K. Lozano. Functionalized graphene oxide as reinforcement in epoxy based nanocomposites. *Surfaces and Interfaces*, 10:100 – 109, 2018.
- [59] David W. Richerson. *Modern Ceramic Engineering*. Taylor & Francis, 1988.
- [60] Brian L Cushing, Vladimir L Kolesnichenko, and Charles J O'Connor. Recent advances in the liquid-phase syntheses of inorganic nanoparticles. *Chemical reviews*, 104(9):3893–3946, 2004.
- [61] C Sanchez, J Livage, M Henry, and F Babonneau. Chemical modification of alkoxide precursors. *Journal of Non-Crystalline Solids*, 100(1-3):65–76, 1988.
- [62] John D Wright and Nico AJM Sommerdijk. *Sol-gel materials: chemistry and applications*. CRC press, 2014.
- [63] Werner Stöber, Arthur Fink, and Ernst Bohn. Controlled growth of monodisperse silica spheres in the micron size range. *Journal of colloid and interface science*, 26(1):62–69, 1968.

- [64] Sarah L Greasley, Samuel J Page, Slobodan Sirovica, Shu Chen, Richard A Martin, Antonio Riveiro, John V Hanna, Alexandra E Porter, and Julian R Jones. Controlling particle size in the stöber process and incorporation of calcium. *Journal of colloid and interface science*, 469:213–223, 2016.
- [65] Hui Ye, Liqun Zhu, Weiping Li, Huicong Liu, and Haining Chen. Simple spray deposition of a water-based superhydrophobic coating with high stability for flexible applications. *Journal of Materials Chemistry A*, 5(20):9882–9890, 2017.
- [66] G Polizos, Gyoung Gug Jang, D Barton Smith, FA List, Matthew G Lassiter, Jaehyeung Park, and Panos G Datskos. Transparent superhydrophobic surfaces using a spray coating process. *Solar Energy Materials and Solar Cells*, 176:405–410, 2018.
- [67] Fatemeh Zabihi and Morteza Eslamian. Characteristics of thin films fabricated by spray coating on rough and permeable paper substrates. *Journal of Coatings Technology and Research*, 12(3):489–503, May 2015.
- [68] Jianchi Huang, Zhihao Yuan, Siyi Gao, Jianshan Liao, and Morteza Eslamian. Understanding spray coating process: Visual observation of impingement of multiple droplets on a substrate. *Journal of Shanghai Jiaotong University (Science)*, 23(1):97–105, Feb 2018.
- [69] Alexander L Yarin. Drop impact dynamics: splashing, spreading, receding, bouncing... *Annu. Rev. Fluid Mech.*, 38:159–192, 2006.
- [70] Sigma-Aldrich. 1h,1h,2h,2h-perfluorooctyltriethoxysilane. Accessed: 2019-04-09.
- [71] Kock-Yee Law and Hong Zhao. *Surface wetting: characterization, contact angle, and fundamentals*. Springer, 2016.
- [72] Barron AR Alexander S. Hill D, Attia H. Size and morphology dependent surface wetting based on hydrocarbon functionalized nanoparticles. *Journal of Colloid and Interface Science*, 543:328 – 334, 2019.
- [73] Ezekiel D Dikio, Simphiwe M Nelana, David A Isabirye, and Eno E Ebenso. Density, dynamic viscosity and derived properties of binary mixtures of methanol, ethanol,

- n-propanol, and n-butanol with pyridine at $t=(293.15, 303.15, 313.15 \text{ and } 323.15) \text{ K}$. *Int. J. Electrochem. Sci*, 7(11), 2012.
- [74] Jonathan N Coleman, Martin Cadek, Rowan Blake, Valeria Nicolosi, Kevin P Ryan, Colin Belton, Antonio Fonseca, Janos B Nagy, Yurii K Gun'ko, and Werner J Blau. High performance nanotube-reinforced plastics: Understanding the mechanism of strength increase. *Advanced Functional Materials*, 14(8):791–798, 2004.
- [75] Bruker. Periodic table of elements and x-ray energies. 2019.
- [76] C. W. Extrand and Sung In Moon. When sessile drops are no longer small: Transitions from spherical to fully flattened. *Langmuir*, 26(14):11815–11822, 2010.
- [77] D Paulkowski, K Vissing, and M Santos. Cost-efficient production of plasma polymeric coatings on rotary shaft sea lings. *Fluid Sealings, Manchester, UK*, 2016.

Appendices

A - Spray coat optimization

Spray optimization images from one, three and four layers presented respectively.

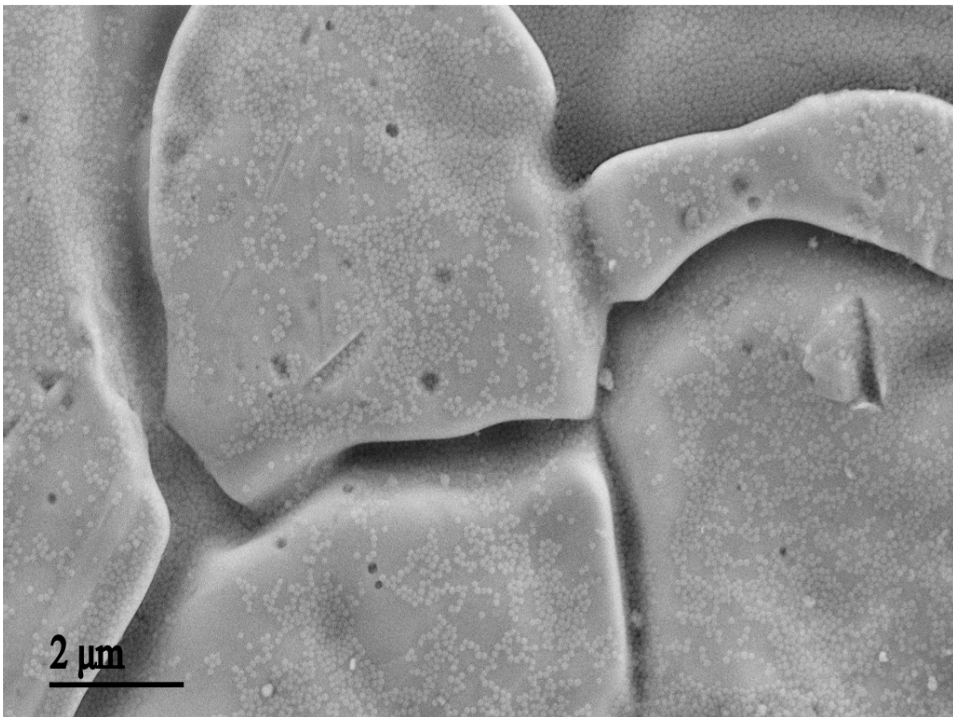


Figure 1: Nanoparticle coverage after one layer.

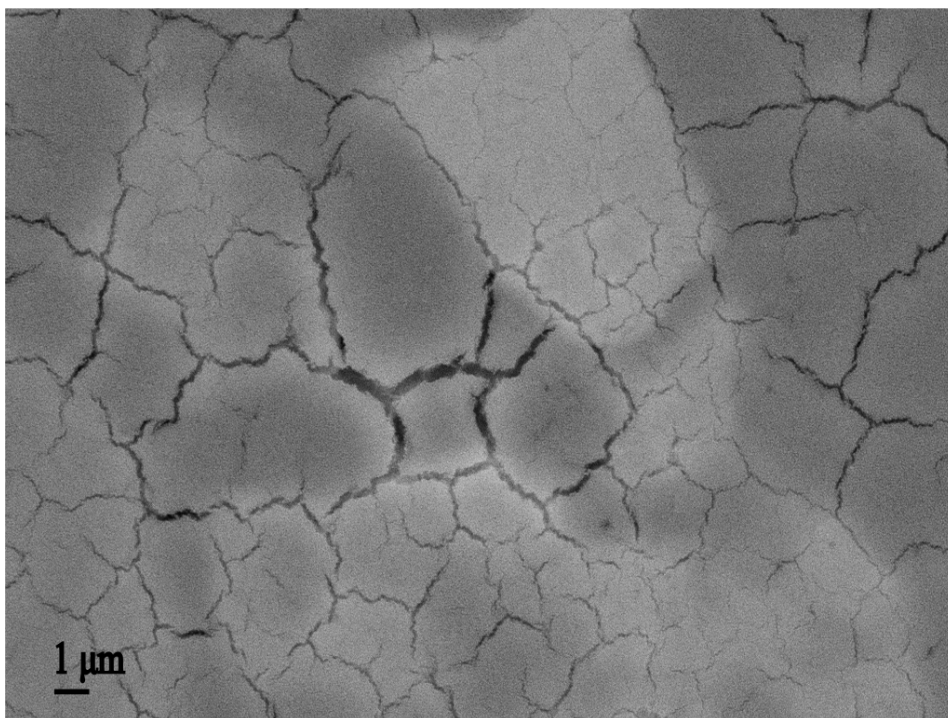


Figure 2: Nanoparticle coverage after three layers.

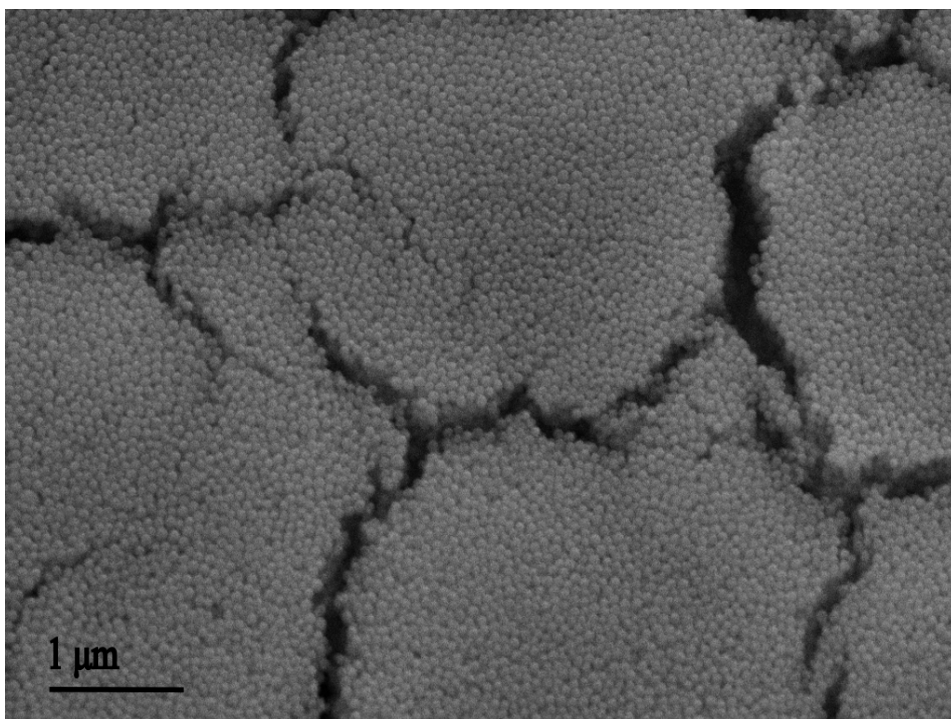


Figure 3: Nanoparticle coverage after four layers.

B - Nanoparticles

Additional FESEM images of NP1 and NP2 particles.

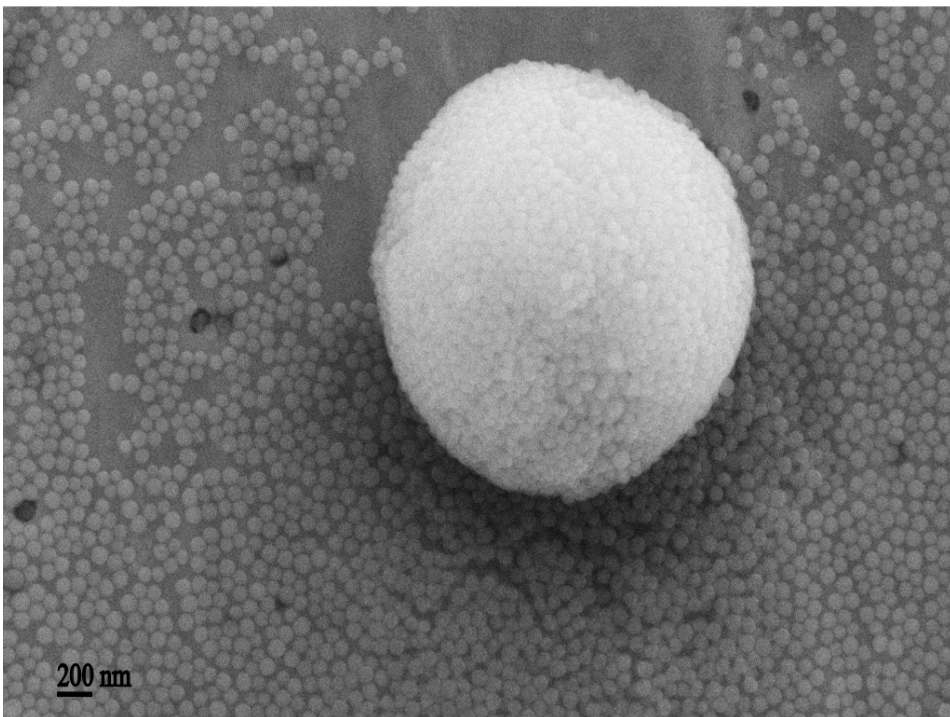


Figure 4: Image of a nanoparticle cluster on a γ 0- β 0-NP1 sample. A thin and even spreading of nanoparticles can also be observed.

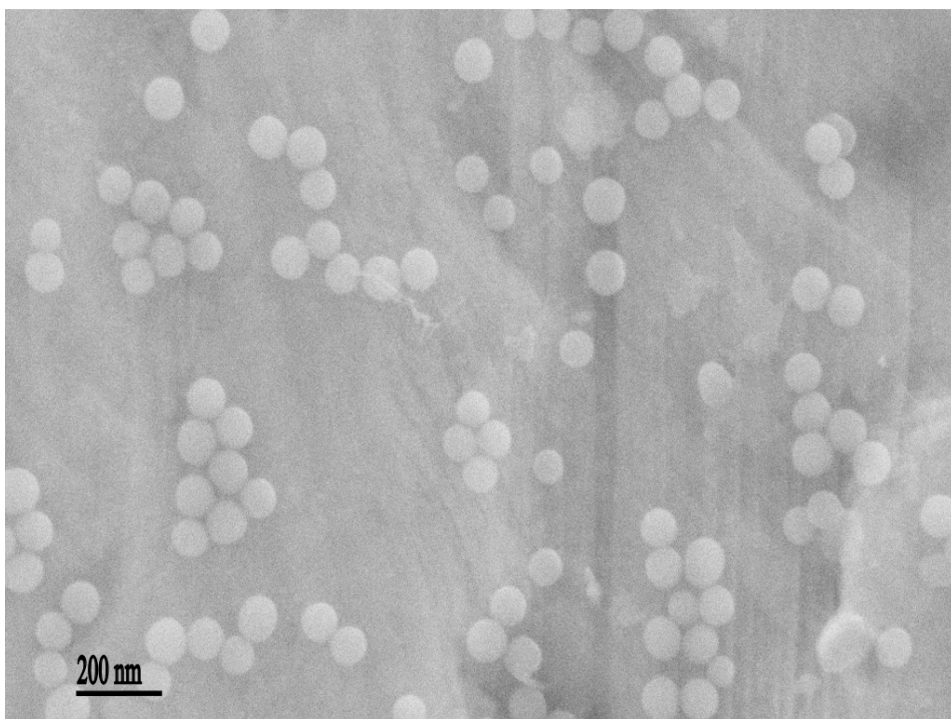


Figure 5: Magnified image of a NP1 particles on a γ_0 - β_0 -NP1 sample.

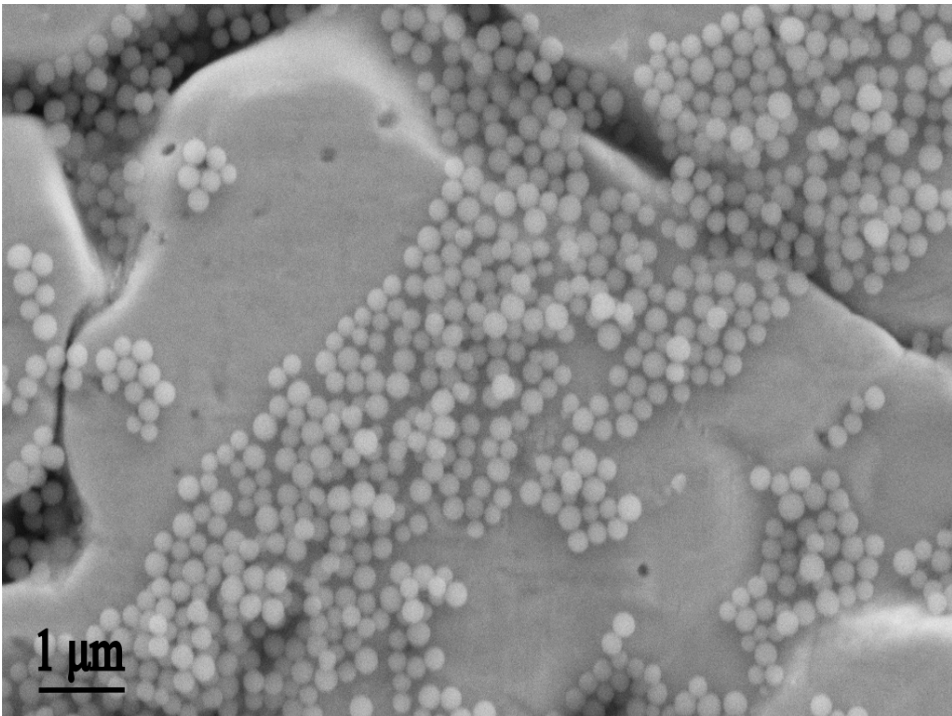


Figure 6: Image of nanoparticle coverage on a γ 0- β 0-NP2 sample.

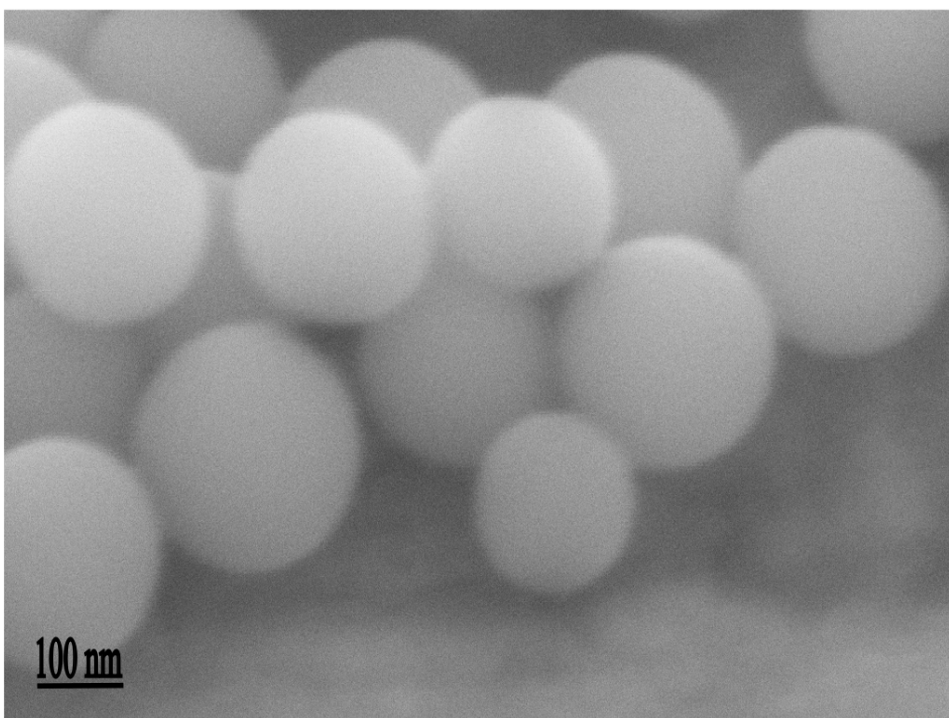


Figure 7: Image of a $\gamma_0\text{-}\beta_0\text{-NP}_2$ sample displaying the size variance of NP2 particles.

C - Coating

Additional FESEM images of coatings synthesized with and without nanoparticles.

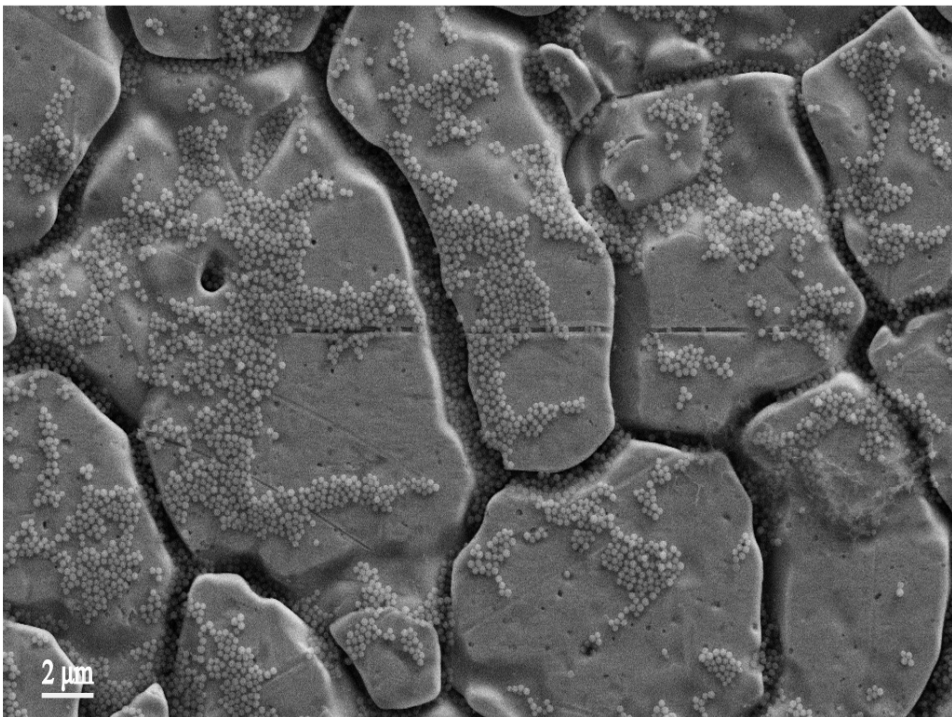


Figure 8: Overview image of a γ 1- β 2-NP2. A decent particle coverage can be observed. A graphene oxide sheet can be observed on the bottom right side of the image.

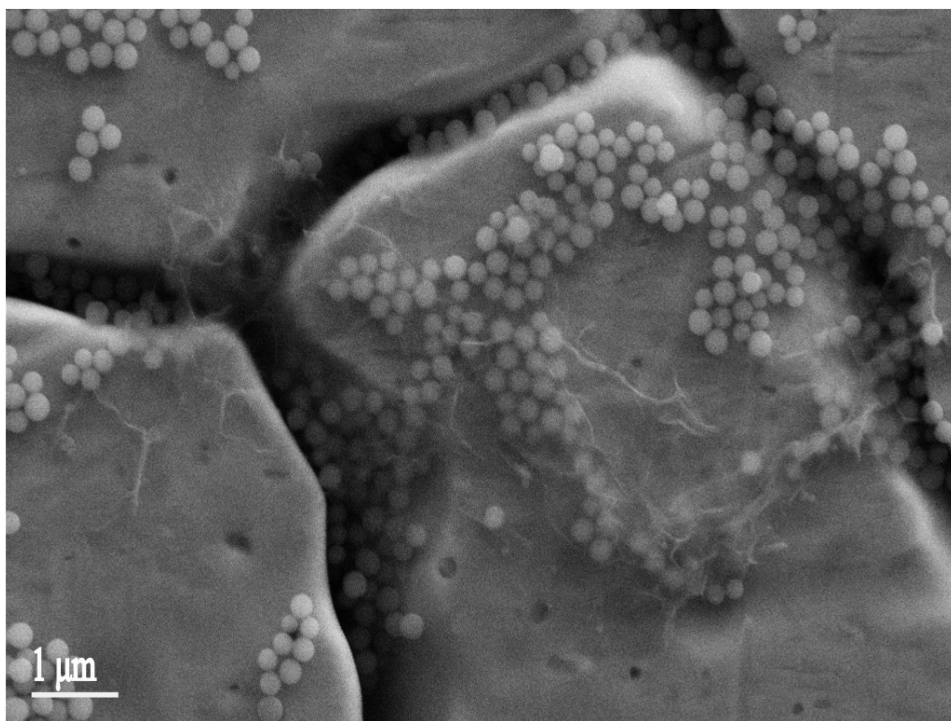


Figure 9: Magnified image of a $\gamma 1$ - $\beta 2$ -NP2. A graphene oxide sheet can be seen covering the nanoparticles.

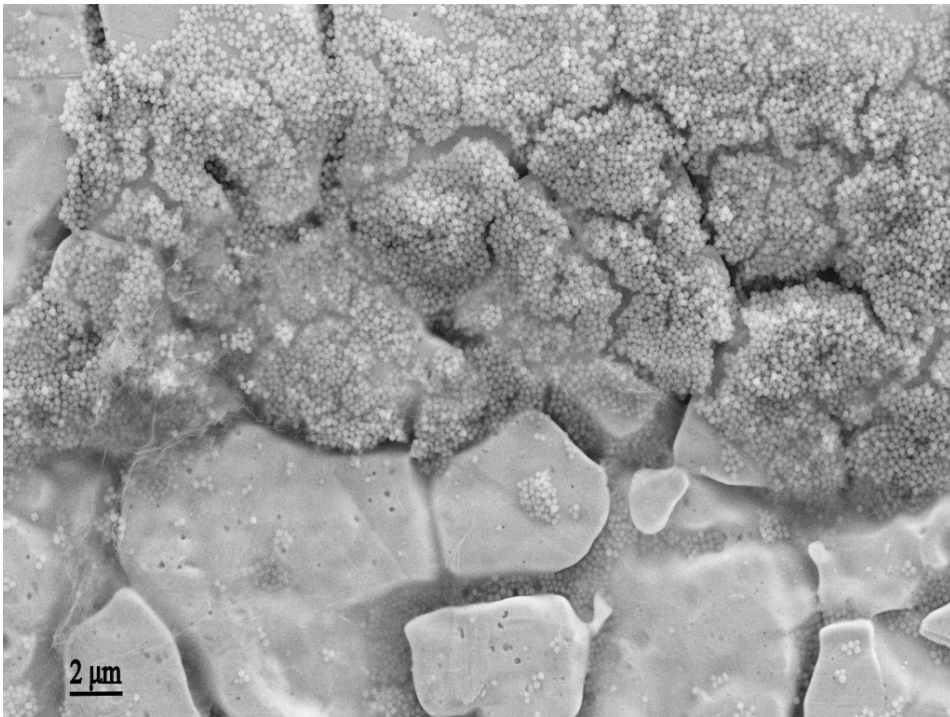


Figure 10: Overview image of a $\gamma_2\text{-}\beta_2\text{-NP2}$. A large particle buildup can be observed with high amounts of graphene oxide covering the buildups.

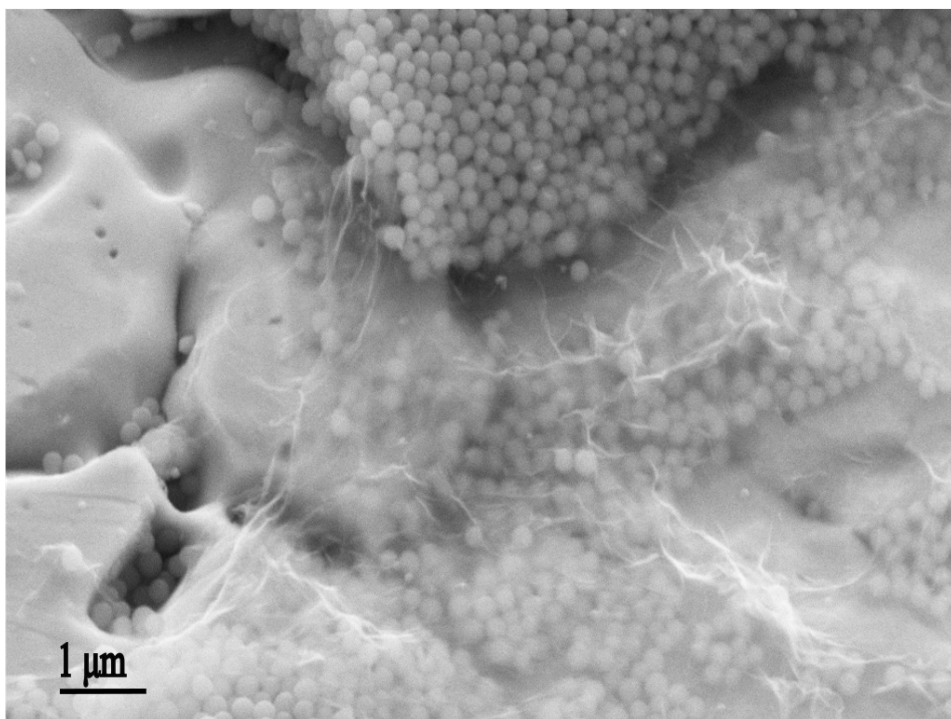


Figure 11: Image of a $\gamma 2$ - $\beta 2$ -NP2. A graphene oxide sheet can be seen covering the nanoparticles.

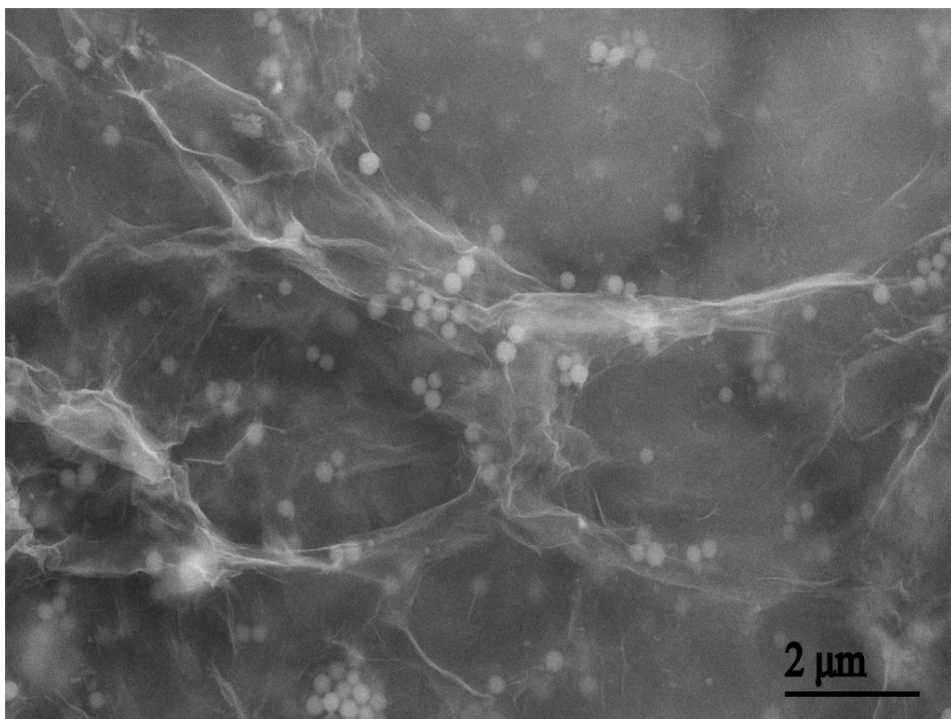


Figure 12: Image of a $\gamma 3\text{-}\beta 2\text{-NP2}$ sample. A large concentration of graphene oxide sheets can be seen covering the nanoparticles.

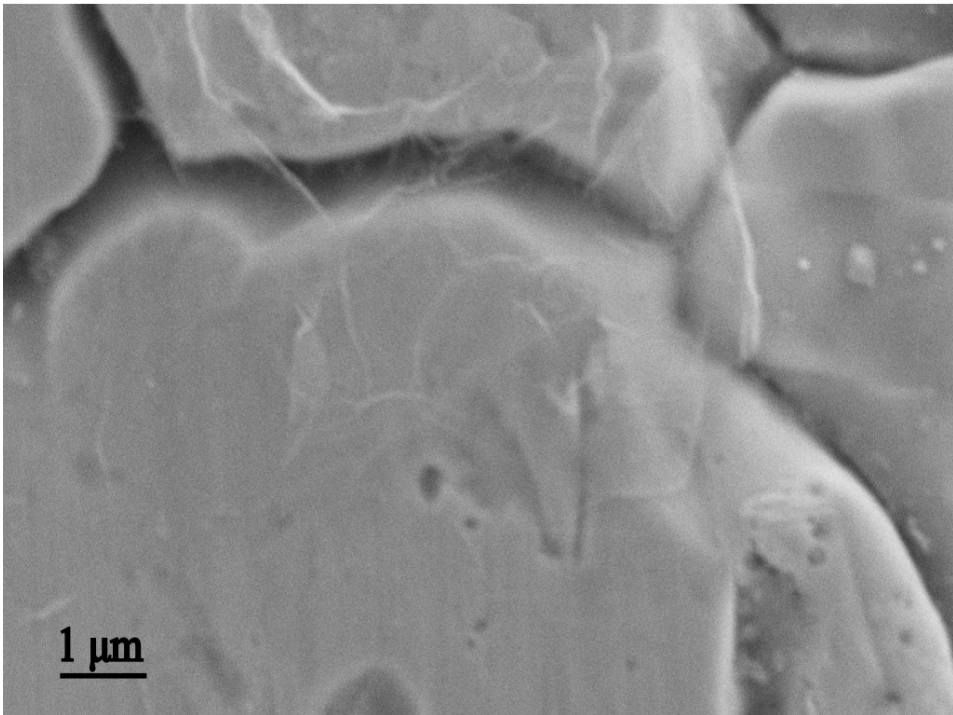


Figure 13: Image of a γ_1 - β_2 -NP0 sample. A graphene oxide sheet covering the cold-rolled microstructure can be observed.

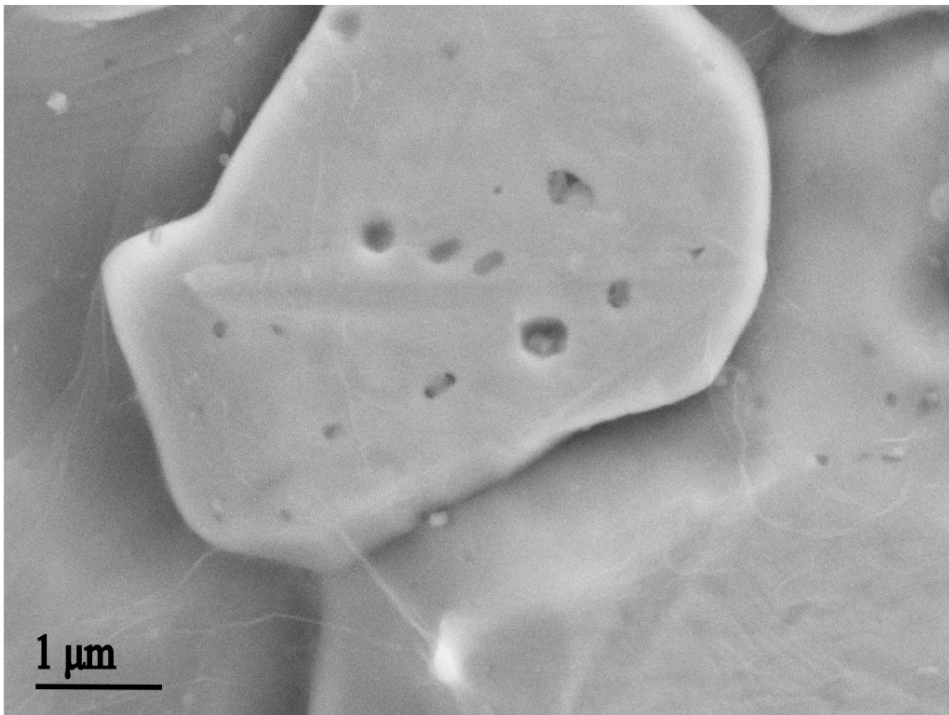


Figure 14: Image of a $\gamma_2\text{-}\beta_2\text{-NP0}$ sample. A graphene oxide sheet covering the cold-rolled microstructure can be observed.

D - Python codes

Codes created in python 3.7.

```
In [ ]: import numpy as np
import matplotlib.pyplot as plt

# Code used for importing data and dividing data into vectors.
def readRoughnessData(g):
    fileName=g
    a=np.genfromtxt(fileName)
    a=np.transpose(a)
    lateral=a[0]
    raw=a[1]
    return lateral, raw

# Code used to calculate the average roughness
def calcRa(vec):
    avg = sum(vec)/len(vec)
    Ra = 0
    for i in range(len(vec)):
        Ra = Ra + abs(vec[i]-avg)
    RaFinal = Ra/len(vec)
    return RaFinal

# Code used to calculate sample standard deviation
def standardDev(vec):
    xsquare = 0
    avg = sum(vec)/len(vec)
    for i in range(len(vec)):
        xsquare = xsquare + ((vec[i]-avg)**2)
    final = np.sqrt(xsquare/(len(vec)-1))
    return avg, final

# Code used to calculate population standard deviation
def standardDev2(vec):
    xsquare = 0
    avg = sum(vec)/len(vec)
    for i in range(len(vec)):
        xsquare = xsquare + ((vec[i]-avg)**2)
    final = np.sqrt(xsquare/len(vec))
```



```
        return avg, final

# Code used to calculate the root mean square
def calcRq(vec):
    out = 0
    avg = sum(vec)/len(vec)
    for i in range(len(vec)):
        out = out + ((vec[i]-avg)**2)
    final = np.sqrt(out/(len(vec)))
    return final

# Code used to calculate skewness
def calcRsk(vec):
    avg = sum(vec)/len(vec)
    out = 0
    Rq = calcRq(vec)
    for i in range(len(vec)):
        out = out + ((vec[i]-avg)**3)
    final = out/(len(vec)*((Rq)**3))
    return final

# Code used to calculate kurtosis
def calcRku(vec):
    avg = sum(vec)/len(vec)
    out = 0
    Rq = calcRq(vec)
    for i in range(len(vec)):
        out = out + ((vec[i]-avg)**4)
    final = out/(len(vec)*((Rq)**4))
    return final
```